

NASA Contractor Report 202008

1N-99

CoP.

287199

**National Aeronautics and Space Administration
(NASA)/American Society for Engineering Education
(ASEE) Summer Faculty Fellowship Program - 1996**

Volume 1

Richard B. Bannerot and Donn G. Sickorez, Editors

Grant NAG 9-867



June 1997

NASA Contractor Report 202008

National Aeronautics and Space Administration (NASA) American Society of Engineering Education (ASEE) Summer Faculty Program - 1996

Volume 1

Richard B. Bannerot, Editor
University of Houston
Houston, Texas

Donn G. Sickorez, Editor
University Programs Office
Lyndon B. Johnson Space Center
Houston, Texas

Grant NAG 9-867



National Aeronautics and
Space Administration

June 1997



PREFACE

The 1996 Johnson Space Center (JSC) National Aeronautics and Space Administration (NASA)/American Society for Engineering Education (ASEE) Summer Faculty Fellowship Program was conducted by the University of Houston and JSC. The 10-week program was operated under the auspices of the ASEE. The program at JSC, as well as the programs at other NASA Centers, was funded by the Office of University Affairs, NASA Headquarters, Washington, D.C. The objectives of the program, which began in 1965 at JSC and in 1964 nationally, are:

1. To further the professional knowledge of qualified engineering and science faculty members.
2. To stimulate an exchange of ideas between participants and NASA.
3. To enrich and refresh the research and teaching activities of participant's institutions.
4. To contribute to the research objectives of the NASA Centers.

Each faculty fellow spent at least 10 weeks at JSC engaged in a research project commensurate with his/her interests and background and worked in collaboration with a NASA/JSC colleague. This document is a compilation of the final reports on the research projects done by the faculty fellows during the summer of 1996. Volume 1 contains the first 12 reports, and volume 2 contains the remaining 13 reports.

CONTENTS

Volume 1

1.	ANDERSON, Gary: <i>Intelligent System Development Using a Rough Sets Methodology</i>	1-1 -1
2.	BACHNAK, Rafic: <i>Electronic Design Automation: Integrating the Design and Manufacturing Functions</i>	2-1 -2
3.	BASCIANO, Thomas: <i>Development of Methods to Evaluate Safer Flight Characteristics</i>	3-1 -3
5.	BISHOP, Phillip: <i>Measurement of Carbon Dioxide Accumulation and Physiological Function in the Launch and Entry and Advanced Crew Escape Suit</i>	5-1 -4
6.	BLACKWELL, Harvel: <i>Analysis of Flow from ARC-Jet Spectra</i>	6-1 -5
7.	CACCESE, Vincent: <i>Design Criteria for X-CRV Honeycomb Panels - A Preliminary Study</i>	7-1 -6
8.	CHOLEWIAK, Roger: <i>Studies of the Interactions Between Vestibular Function and Tactual Orientation Display Systems</i>	8-1 -7
9.	COOMBS, Cassandra: <i>There's Iron in Them Thar Hills: A Geologic Look at the Aristarchus Plateau as a Potential Landing Site for Human Lunar Return</i>	9-1 -8
11.	GIARRATANO, Joseph: <i>Inherit Space</i>	11-1
12.	HARVEY, Ralph: <i>Studies of Magmatic Inclusions in the Basaltic Martian Meteorites Shergotty, Zagami, EETA 79001 and QUE 94201</i>	12-1
13.	HAYES, Linda: <i>Developing Tools and Techniques to Increase Communication Effectiveness</i>	13-1
14.	HOGAN, Harry: <i>Estimating Trabecular Bone Mechanical Properties from Non-Invasive Imaging</i>	14-1

Volume 2

15.	JANIKOW, Cezary: <i>Improving Search Properties in Genetic Programming</i>	15-1
17.	KIME, Yolanda: <i>Prediction of Degraded Strength in Composite Laminates with Matrix Cracks</i>	17-1
18.	KLEIS, Stanley: <i>Bioreactor Mass Transport Studies</i>	18-1
19.	KOEHLERT, Erik: <i>Developing a Graphical User Interface for the ALSS Crop Planning Tool</i>	19-1
20.	LEMOINE, Sandra: <i>A Comparison of Total and Intrinsic Muscle Stiffness among Flexors and Extensors of the Ankle, Knee and Elbow</i>	20-1

21.	LEON, V.: <i>Integration of CELSS Simulation with Long-Term Crop Scheduling</i>	21-1
22.	MCGINNIS, Michael: <i>Influence of Zero-shear on Yeast Development</i>	22-1
23.	MULLEN, Terence: <i>Computer Based Training: Field Deployable Trainer & Shared Virtual Reality</i>	23-1
24.	PATE, Dennis: <i>A Human Factors Analysis of EVA Time Requirements</i>	24-1
25.	RICHARDSON, Albert: <i>Simulation of the Predictive Control Algorithm for Container Crane Operation Using MATLAB Fuzzy Logic Tool Box</i>	25-1
27.	WASSIL-GRIMM, Andrew: <i>Database Development for Electrical, Electronic and Electromechanical (EEE) Parts for the International Space Station ALPHA</i>	27-1
28.	WILLIAMS, Trevor: <i>Dynamics Questions Associated with the AERCam Sprint Free-Flyer</i>	28-1
29.	WNUK, Michael: <i>Analysis of Impact Induced Damage and its Effect on Structural Integrity of Space Flight Composite Overwrapped Pressure Vessels</i>	29-1

INTELLIGENT SYSTEM DEVELOPMENT USING A ROUGH SETS
METHODOLOGY

51-63
038272
14A

Final Report
NASA/ASEE Summer Faculty Fellowship Program-1993
Johnson Space Center

294247

Prepared by: Gary T. Anderson, Ph.D.
Academic Rank: Associate Professor
University & Department: University of Arkansas at Little Rock
Department of Applied Science
Little Rock, AR 72204
NASA/JSC
Directorate: Business Information Systems
Division: Information Systems
Office: Information Technology
JSC Colleague: Robert O. Shelton, Ph.D.
Date Submitted: August 9, 1996
Contract Number: NAG 9-867

ABSTRACT

The purpose of this research was to examine the potential of the rough sets technique for developing intelligent models of complex systems from limited information. Rough sets a simple but promising technology to extract easily understood rules from data. The rough set methodology has been shown to perform well when used with a large set of exemplars, but its performance with sparse data sets is less certain. The difficulty is that rules will be developed based on just a few examples, each of which might have a large amount of noise associated with them. The question then becomes, what is the probability of a useful rule being developed from such limited information? One nice feature of rough sets is that in unusual situations, the technique can give an answer of "I don't know". That is, if a case arises that is different from the cases the rough set rules were developed on, the methodology can recognize this and alert human operators of it. It can also be trained to do this when the desired action is unknown because conflicting examples apply to the same set of inputs.

This summer's project was to look at combining rough set theory with statistical theory to develop confidence limits in rules developed by rough sets. Often it is important not to make a certain type of mistake (e.g., false positives or false negatives), so the rules must be biased toward preventing a catastrophic error, rather than giving the most likely course of action. A method to determine the best course of action in the light of such constraints was examined. The resulting technique was tested with files containing electrical power line "signatures" from the space shuttle and with decompression sickness data.

INTELLIGENT SYSTEM DEVELOPMENT USING A ROUGH SETS
METHODOLOGY

Gary T. Anderson
University of Arkansas at Little Rock
BT2
9 August 1996

Robert O. Shelton
Information Technology Office
Information Systems Office
Business Information Systems Directorate



Gary T. Anderson



Robert O. Shelton

INTRODUCTION

As NASA moves forward towards deployment of the space station, a possible permanent manned station on the moon and a manned flight to Mars, the long term reliability and maintenance of life support systems in hostile environments becomes a crucial issue. Intelligent software that can monitor systems and make automated decisions can relieve the human crew of such responsibilities during long space and lunar missions, freeing them to perform other tasks. The complexities of life support and other systems make such software difficult to develop. For example, the software must be able to evaluate several interdependent inputs, with many variations on typical cases. The software should probably also be developed from mission data, which has noise both on system inputs and on system outcomes (i.e., the results of system actions). As a result of these requirements, often very few examples will exist for situations that occur only rarely. It is often in these rare cases where it is critical that the software perform correctly. Rough sets is one technique that makes intelligent monitoring of complex systems less cumbersome.

Since its introduction [Pawlak, 1982], rough sets has proven to be a simple but effective technology to extract rules from data [Slowinski, 1992]. Discussions of rough set methodology are given in [Pawlak, 1988], [Grzymala-Busse, 1988], [Chan, 1991] and [Szladow, 1993]. The rough set technique has been shown to perform well when used with a large set of examples, but its performance with small data sets is less certain. The problem is that rules will be developed based on just a few examples, each of which might have a large amount of noise associated with them. Furthermore, conflicting rules will often be triggered when the system is used on new cases. The question becomes, what is the probability of a useful rule being developed from such limited information? Probability theory is used to determine how much confidence one can have in a given rough set rule based on the number of examples that support that rule.

ROUGH SETS

A core idea in rough sets is that precision is frequently not necessary when looking for patterns in data. For example, a fever is usually enough to indicate the presence of disease, without knowledge of exact body temperature. Rough set rules are generated from a set of examples with known outcomes. Discrete inputs are used as is, while continuous inputs are divided into discrete categories. An input with a temperature range of 96 - 110 °F might be divided into broad ranges described by cold, cool, warm and hot. In this manner, strong patterns that exist in the data are reflected in the model.

The rough sets algorithm is typically used to extract rules from a table of examples. Each example (table row) is called an object, while each piece of information in the example (table column) is called an attribute. The outcome is then called the decision attribute. Ideally, the decision attribute is completely determined by the other attributes in the table, and the outcome is said to be discernible by the inputs. The rough set methodology then searches for a minimal set of input attributes, called reducts, that can

completely describe the decision attribute. Small reducts produce general rules, while large reducts produce specific rules. Various factors can cause the outcome to not be completely discernible by the inputs. These include cases where there is noise in the data, the input attributes do not completely describe the outcome, complex relationships exist between the input and decision attributes, or the input attributes are divided non-optimally into discrete categories.

Figure 1 shows an example of a two input case where the outcome is either a 'yes' or a 'no'. Each input is divided into six discrete categories, and it is assumed that no noise is present on either the inputs or the outcome. The region enclosed by the irregularly shaped loop marks the true boundary between 'yes' and 'no' outcomes for different combinations of the two inputs. The white boxes inside the loop are called the positive region, or lower approximation of the outcome. These are boxes that always have 'yes' outcomes in the table of examples. The negative region, where all examples have an outcome of 'no', is the combination of all white boxes outside of the boundary loop. In between these two areas is a boundary region, marked by gray boxes in Figure 1. In the boundary region, some examples will have a 'yes', while others will have a 'no' outcome. Because the examples that fall in the boundary region are inconsistent, two types of rules are often generated by rough set algorithms, called certain and possible rules. Certain rules are developed from a set of completely consistent examples (e.g., the positive and negative regions in Figure 1), while possible rules are generated from a set of inconsistent examples (e.g., the boundary region in Figure 1). As will be shown, however, because rules are generated from a limited sample of examples, there are no rules that are completely certain.

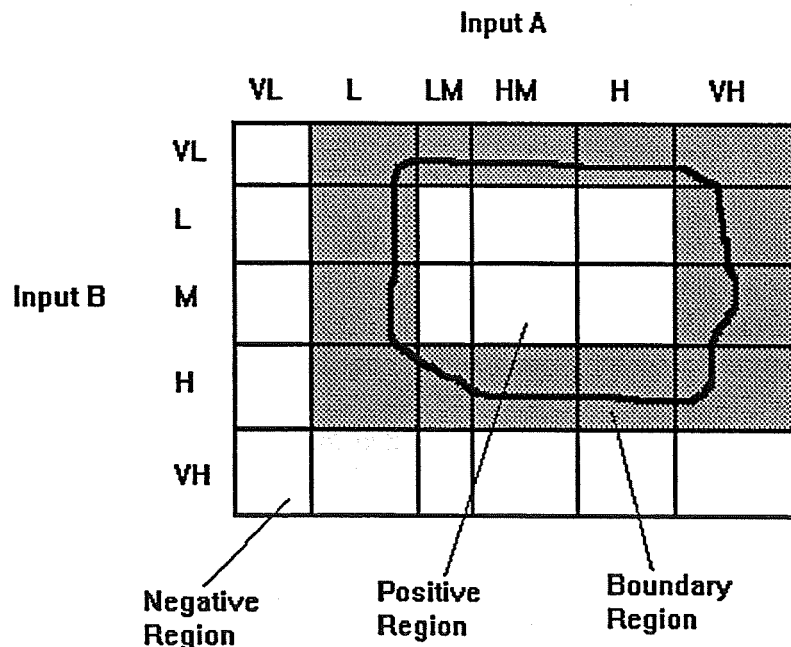


Figure 1.- Rough set example with consistent data.

The boundary region in Figure 1 can be made smaller by changing the definition of the attribute categories for the inputs. For example, if the definition of VL is increased for input A, the boundary region will decrease in size. The price to pay for such a move is that rules generated for input A being L will have fewer examples supporting them, and will thus have less certain validity.

Figure 2 shows the same case as in Figure 1, except that now noise has been added to the data. The noise adds inconsistencies to what should be the positive and negative regions of the model, and sometimes creates a false consistency in the boundary region. If the rough set model is generated from a large set of examples, this will not cause a major problem because the patterns will be clearly discernible through the noise. A difficulty arises, however, when the number of examples the model is based on is small in any region of the input space. Because the number of examples for a given combination of inputs is small, noise can significantly alter the apparent outcome for that combination.

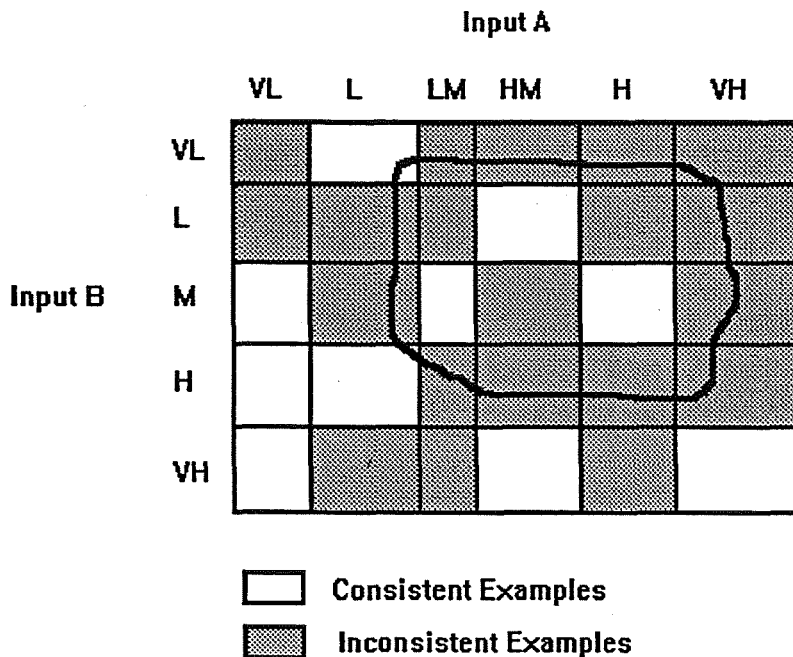


Figure 2.- Rough set example with noisy data.

There are many reasons a data set might have relatively few examples in certain regions. Certain values of an input may occur infrequently, or it may be physically difficult to collect data for these input ranges. Sometimes, it is desirable to predict an event that occurs only rarely, such as a moderate to severe earthquake in Arkansas. Often, a model will have a large number of inputs, making the number of examples required to fill all possible combinations of inputs quite large. A more common difficulty is when predictions

section presents a method of determining the confidence level one can have in a given rule, which can then be used to resolve conflicts between rules.

PROBABILITY CALCULATION

Given n samples from a binary distribution, r of which are true, what is the probability p of a true response? If p is known, then the probability $P(n, r, p)$ of getting r true responses is:

$$P(n, r, p) = \binom{n}{r} p^r (1-p)^{n-r} \quad (1)$$

To find the mode, the peak of the distribution, simply maximize (1) with respect to p as follows:

$$\frac{d}{dp} P(n, r, p) = r p^{r-1} (1-p)^{n-r} - p^r (n-r) p^{n-r-1} = p^{n-r-1} (r(1-p) - (n-r)p) = 0 \quad (2)$$

Solving (2) one gets

$$r-rp = np - rp \quad (3)$$

or $p = r/n$. To obtain a probability distribution from (1) one need only normalize as follows

$$D(p; n, r) = \frac{\binom{n}{r} p^r (1-p)^{n-r}}{\int_0^1 \binom{n}{r} p^r (1-p)^{n-r} dp} \quad (4)$$

The integral in the denominator of (4) can easily be evaluated using integration by parts.

Let $I(n, r) = \int_0^1 p^r (1-p)^{n-r} dp$. Then

$$I(n, n) = \int_0^1 p^n dp = \frac{1}{n+1} \quad (5)$$

and

$$\begin{aligned} I(n, r) &= \int_0^1 p^r (1-p)^{n-r} dp = \frac{1}{r+1} p^{r+1} (1-p)^{n-r} \Big|_0^1 + \frac{n-r}{r+1} \int_0^1 p^{r+1} (1-p)^{n-(r+1)} dp \\ &= \frac{n-r}{r+1} I(n, r+1) \end{aligned} \quad (6)$$

Solving the recurrence (6) with end condition (5), one gets

$$I(n,r) = \frac{1}{n+1} \prod_{j=r}^{n-1} \frac{n-j}{j+1} = \frac{1}{(n+1) \binom{n}{r}} \quad (7)$$

The mean of the distribution (4) is realized as

$$\bar{p} = \frac{I(n+1, r+1)}{I(n, r)} = \frac{(n+1)(r+1)!(n-r)!n!}{(n+2)r!(n-r)!(n+1)!} = \frac{r+1}{n+2} \quad (8)$$

Note that the expected value of p (the mean value of p) is different from the mode (the peak value of the distribution) for all cases except $r/n = 0.5$.

Confidence limits for the underlying value of p can be obtained by numerically integrating (4) with respect to p for any given values of n and r . Starting with $p = 0$ and increasing it incrementally, the area of the distribution from 0 to any given value of p can be calculated. Since the total area of the distribution is equal to one, confidence limits can easily be placed on upper and lower approximations of p . For example, if the area under (4) for a given value of r and n is 0.05 from $p = 0$ to 0.60, then there is a 5 percent chance that the true underlying probability for this case is less than 0.60.

NUMERICAL MODEL VERIFICATION

The above analysis answers the question of, given r/n 'yes' responses, what is the likely underlying probability p of the system? In order to numerically verify the results, this question must be rephrased to: given a known underlying probability p , what is the likelihood of getting r 'yes' responses out of n trials? An algorithm was written to answer the latter question for $n = 10$ and $r = 5$ through 9. Probabilities were incremented from 0 to 1 in 0.001 steps, with 40,000 trials were run for each probability. In each trial, ten numbers were randomly generated and the results were checked for r 'yes' responses. The total number of $r/10$ 'yeses' was recorded for each p , and the area under the distribution was calculated from 0 to p for each probability. The results were then compared with the above analysis for calculating the mean, the mode and confidence limits on the underlying probability for any given observation of $r/10$ 'yes' observations.

Results for the theory based calculations can be compared to the ones from the numerical experiment. The largest differences between the numerical and analytical results occurred for $r = 9$. In this case, the maximum difference between the cumulative distributions is 0.0019, or less than 0.2% of the maximum. The 10% confidence level is 0.69 and the 90% confidence level is 0.95 in both cases. When the cumulative distribution for the experimental case is plotted versus the theory-based calculations, the result is a line with a correlation coefficient (Pearson's R) of 1.000. The mode for both cases is 0.9, which equals the expected value of n/r .

DISCUSSION

The most obvious conclusion from the above analysis is that there are no certain rules in rough sets. Rules are generated based from a sample of similar cases, and it is hoped that those cases are representative of all cases the rough set model will ever see. The typical probability normally used to evaluate rules, $p = r/n$, represents the peak of the distribution that represents all possible values of p for a given combination of r and n . The distribution, however, is skewed to the left for all values of $r/n > 0.5$. The minimum error over large number of rules will therefore occur for the probability that divides the distribution into two equal areas, $p = (r+1)/(n+2)$, rather than r/n . Even with a completely consistent set of examples, the minimum error over a large number of rules will always occur by choosing $p < 1$, irrespective of the number of consistent examples supporting the rule. For example, if a person flips a coin three times in a row, on average they will come up with three heads once in eight times. Having seen a person flip this coin three times, all of which came up heads, one cannot assume that the coin will always come up heads. Now suppose in a given rough set model there are numerous combinations of inputs that all have three examples in them, all with 'yes' responses. The average probability of getting a 'yes' response, over all these rules is 0.8, not 1.

Sometimes it is desirable to have a rule used only when it has a high probability of being correct. Confidence limits can be used to determine what rules to use. Note, however, that high confidence limits require a large number of examples. For example, if one wishes to have a 99% confidence that $p > 0.9$ for a rule to fire, it requires a minimum r/n of 43/43, 62/63, or 78/80. Other times it is a necessary to make a "best guess" as to what the correct answer is, in that case the decision indicated by r/n is always the most appropriate choice.

Often with rough set models it is necessary to decide between conflicting rules. The mean probability, $\bar{p} = (r+1)/(n+2)$ can be used to determine which rule is stronger. Often the cost for a wrong decision is greater than the reward for a correct decision, such as in the case of screening for cancer. Mean probabilities can be used with a cost functional to determine the optimal decision. Let tp represent a correct 'yes' predictions for a rough set model, tn represent a correct 'no' prediction, fp an incorrect 'yes' prediction and fn an incorrect 'no' prediction. A cost function, C , can be defined as follows:

$$C = a_1 tp + a_2 tn - a_3 fp - a_4 fn \quad (9)$$

where $a_1 - a_4$ are the relative costs of each decision. Let p_y be the mean probability of a true positive (tp), $(1 - p_y)$ the mean probability of a false positive (fp), p_n the mean probability of a true negative (tn) and $(1 - p_n)$ the probability of a false negative. For a positive rule to fire, $a_1 p_y - a_3 (1 - p_y)$ must be greater than 0; conversely, $a_2 p_n - a_4 (1 - p_n)$ must be greater than 0 for a negative rule to fire (otherwise a no decision is better). To

choose between conflicting positive and negative rules, the benefits of each rule must be compared. For a 'yes' rule to have more advantage than a 'no' rule,

$$a_1 p_y - a_3 (1 - p_y) > a_2 p_n - a_4 (1 - p_n) \quad (10)$$

Solving for p_y , we get

$$p_y > (a_2 + a_4) / (a_1 + a_3) * p_n + (a_3 - a_4) / (a_1 + a_3) \quad (11)$$

for a 'yes' rule to control the decision, otherwise the 'no' rule prevails.

The analysis in this paper was carried out for a decision attribute with only two possible values. It is easy to see that this can be expanded to any number of categories. If one is only interested in whether a decision is correct or not, then the analysis holds as is. Otherwise, the probability description given in (1) can be modified to include more than two states, and the calculations redone.

APPLICATIONS

The rough set methodology was applied to two applications, detection of the space shuttle electronic "signatures" and prediction of decompression sickness. The space shuttle has numerous electrical systems that periodically turn on and off. It is often desirable to know when individual appliances are operating, but the number of these devices makes using telemetry to send this information back to earth problematic. The electrical power usage in the shuttle, however, is regularly monitored by mission control. Fluctuations in the power indicate that different apparatus is turning on and off. In the past, human operators examined these fluctuations to determine which piece of equipment was turning on and off. Automation of the electrical power "signatures" recognition would eliminate the need for human monitors.

Rough sets was used to classify ten different electrical power signatures, including a "none of the above" category. On a model development set, the rough sets technique was able to correctly classify 84.6% of over 5,000 cases, with 14.6% no decisions and 0.9% misclassified. When electrical signatures in the "none of the above" category were removed, the rough set model correctly classified 98.7% of the signatures, with a no decision in 1% and 0.3% misclassified. These preliminary results indicate that additional work on rough set model development for electrical "signature" recognition is justified.

Decompression sickness (DCS), commonly known as the "bends", occurs when people experience rapid changes in external pressure. This most commonly occurs when divers resurface too rapidly from deep dives, but may also happen when pilots fly at high altitudes. Astronauts performing an extravehicular activity (EVA), or space walk, may also be at risk of developing DCS due to the low pressure in space suits. A preliminary rough set model of decompression sickness was developed from retrospective data on

1018 exposures. Fourteen physiologic and case history inputs were available for each subject, and the outcome was the development or absence of DCS. The model was tested on 706 subjects that were not among the 1018 cases used for model development. The rough set model was able to correctly classify subjects as experiencing DCS or not 83% of the time. This compares well with the 79% correct classification seen with stepwise logistic regression, and warrants further investigation of the rough set model.

REFERENCES

- Chan, C.C., "Incremental Learning of Production Rules from Examples Under Uncertainty: A Rough Set Approach", *Int. J. Software Eng. and Knowledge Eng.*, vol. 1, No. 4, 1991, 439-461.
- Grzymala-Busse, J.W., "Knowledge Acquisition Under Uncertainty: A Rough Set Approach", *J. Intel. Robotic Syst.*, vol. 1, 1988, 3-16.
- Pawlak, Z., "Rough Sets", *Int. J. Computer Inf. Sci.*, vol. 11, 1982, 145-172.
- Pawlak, Z., Wong S.K.M., and Ziarko, W., "Rough Sets: Probabilistic versus Deterministic Approach", *Int. J. Man-Machine Studies*, vol. 29, 1988, 81-95.
- Slowinski K., and Slowinski, R., "Sensitivity Analysis of Rough Classification", *Int. J. Man-Machine Studies*, vol. 32, 1990, 693-705.
- Slowinski, R., "Strict and Weak Indiscernibility of Objects Described by Quantitative Attributes with Overlapping Norms", *Foundations of Computing and Decision Sciences*, vol. 18, 1993, 361-369.
- Szladow, A., "Rough Sets: Working with Imperfect Data", *AI Expert*, vol. 8, 1993, 36-41.

S2-33
038283

12A

297253

ELECTRONIC DESIGN AUTOMATION: INTEGRATING
THE DESIGN AND MANUFACTURING FUNCTIONS

Ray Bachnak
Franklin University
EM3
August 2, 1996

Charles Salkowski
Manufacturing & Process Development Branch
Manufacturing, Materials, and Process Technology Division
Engineering Directorate



Ray Bachnak



Charles Salkowski

ELECTRONIC DESIGN AUTOMATION: INTEGRATING
THE DESIGN AND MANUFACTURING FUNCTIONS

Final Report
NASA/ASEE Summer Faculty Fellowship Program -- 1996
Johnson Space Center

Prepared by:	Rafic Bachnak, Ph.D.
Academic Rank:	Professor
University & Department:	Franklin University Electronics Department 201 S. Grant Ave. Columbus, Ohio 43215
NASA/JSC	
Directorate:	Engineering
Division:	Manufacturing, Materials, & Process Technology
Branch:	Manufacturing & Process Development
JSC Colleague:	Charles Salkowski
Date Submitted:	August 2, 1996
Contract Number:	NAG 9-867

ABSTRACT

As the complexity of electronic systems grows, the traditional design practice, a sequential process, is replaced by concurrent design methodologies. A major advantage of concurrent design is that the feedback from software and manufacturing engineers can be easily incorporated into the design. The implementation of concurrent engineering methodologies is greatly facilitated by employing the latest Electronic Design Automation (EDA) tools. These tools offer integrated simulation of the electrical, mechanical, and manufacturing functions and support virtual prototyping, rapid prototyping, and hardware-software co-design. This report presents recommendations for enhancing the electronic design and manufacturing capabilities and procedures at JSC based on a concurrent design methodology that employs EDA tools.

INTRODUCTION

The continuous increase in complexity of electronic systems is making the design and manufacturing of such systems more challenging than ever before. As a result, designers have been moving from the traditional design approach, a sequential process, to concurrent methodologies where the electronic designer becomes aware of the physical layout process and the manufacturing and assembly issues. This integrated environment improves communications among the various design teams and reduces the rise of multiple time iterations.

With design capacities exceeding a million gates and clock rates of more than 300 MHz, system analysis and verification become the major obstacles in the design phase. This is especially true because of signal integrity problems such as timing delays, level distortions, and noise. Furthermore, as technologies evolve, designers will find it impossible to design efficient systems without the use of sophisticated tools. Since 1989, many companies have been successfully using EDA tools. These tools provide integrated simulation of the electrical, mechanical, and manufacturing functions and lead to a correct by design approach [1-11].

Adopting concurrent design methodologies and employing EDA tools based on processes that support virtual prototyping and hardware-software co-design have proven to reduce cost, decrease time to market, and improve product quality. The rest of this report is organized as follows. First, the benefits of using concurrent engineering and EDA tools are described. Second, industry design and manufacturing practices are summarized. Third, the results of evaluating the design capabilities and procedures at JSC are listed. Finally, recommendations to improve the electronic design and manufacturing functions at JSC are presented.

CONCURRENT DESIGN

Designers have realized that to achieve high productivity the processes used are as important as the tools employed. In recent years, the trend has been a move toward more concurrent design methodologies. A major advantage of concurrent design is that it brings together team members from different disciplines. This results in early detection of design flaws and leads to fewer design changes, a reduction in time to market, and the improvement in overall quality. According to a study cited in [12], concurrent design techniques can reduce product development time by up to 70% and improve quality by up to 600%. Figure 1 shows the relationships between various processes in an integrated design and manufacturing environment that employs concurrent engineering. This environment facilitates hardware-software co-design, virtual prototyping, and rapid

prototyping. It also allows for the interaction between electrical, mechanical, and manufacturing engineers.

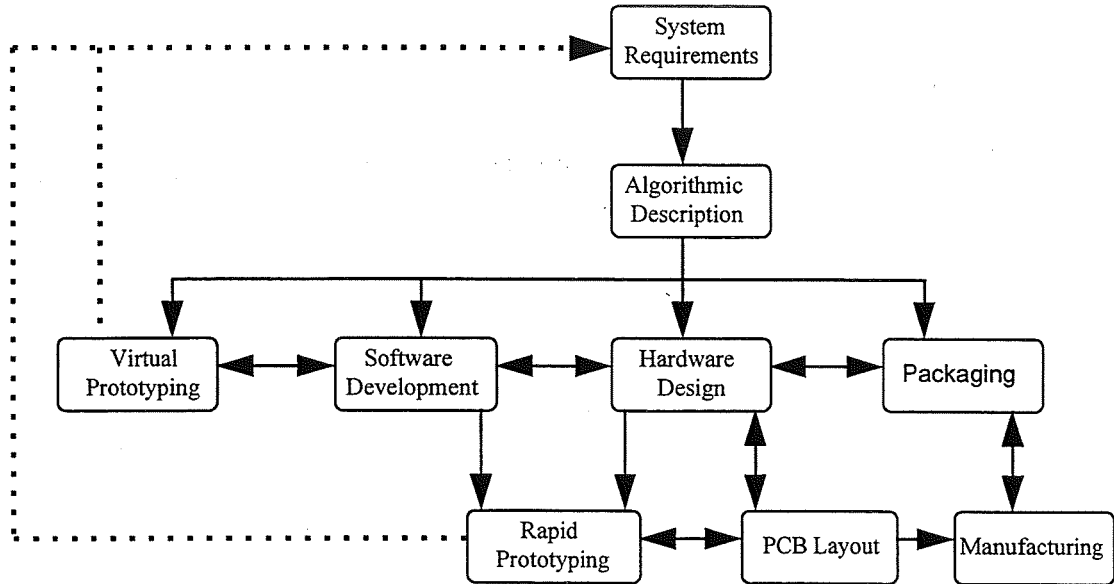


Figure 1.- Integrated Design and Manufacturing Environment

In general, testing hardware and software independently does not lead to complete verification since some problems occur only from the interaction of hardware and software. Delaying integration until the hardware design is complete may impact the cost and time schedule. In addition, if testing is delayed until the board is manufactured, the pressure will be on the software developer to resolve the problems. Concurrent design supports hardware-software co-design and allows for interaction between software and hardware engineers. In this environment, problems can be diagnosed and corrected at the earliest possible phase of the design cycle when the software and hardware engineers can coordinate their efforts so that problems are fixed either in hardware or software depending on the best solution.

While hardware prototyping may still be necessary at some point in the development cycle, taking full advantage of software simulation can significantly improve the overall process. A relatively new technique, virtual prototyping, is used to graphically simulate the operation of a system using a model that best matches reality. In addition to detecting design flaws, virtual prototyping guarantees that the system's operation and performance meet the initial system requirements. Although this approach leads to an increase in the time invested at the beginning of the design process, it reduces the time required for software and hardware integration.

Another important feature of concurrent design is that it facilitates Rapid Prototyping (RP). RP is best achieved by working at a high level of design automation using Hardware Description Languages (HDLs). HDLs take the hardware architecture description and automatically translate it into a physical implementation using various devices such as Application Specific Integrated Circuits (ASICs), programmable logic devices (PLDs), custom Integrated Circuits (ICs), and Field Programmable Gate Arrays (FPGAs). Gate arrays are used for fast turn around prototyping when the design requires better performance than can be achieved with PLDs. Custom ICs can be optimized for performance and functionality but they are time consuming and costly for normal prototyping. While the advantages are many, according to [4] less than 20 percent of the electronic designers in the US have adopted HDLs for RP.

ELECTRONIC DESIGN AUTOMATION

EDA tools provide an effective environment to integrate the design and manufacturing processes. A state of the art EDA system is able to:

- Perform electrical, mechanical, and manufacturing simulation.
- Analyze various design levels, from IC to complete systems.
- Perform mixed-signal (analog and digital) simulation.
- Perform high-level synthesis (behavioral and HDL).
- Support hardware-software co-design, virtual prototyping, and rapid prototyping.
- Provide a centralized database of files accessed by all software modules.
- Offer simultaneous access to all teams.
- Automate data exchanges and provide a standard format for information to be communicated both within the organization and with customers and vendors.

Some EDA companies such as Cadence, Mentor Graphics, Synopsys, and Viewlogic, offer a wide range of software tools that support most of the design functions listed above. The user, however, must recognize that each step of the design process has its own specialized set of tools. Therefore, an organization must carefully determine its design needs and identify those tools that satisfy them. The elements of an EDA system may be grouped as follows:

- Entry tools (Include schematic capture, block diagram and state diagram entry tools, and hardware description language editors).
- Simulation tools (Include analog and digital simulators, timing simulators, HDL simulators, and signal integrity analysis, electromagnetic interference, thermal, vibration, and fatigue analysis, and faults analysis).
- Synthesis tools (Include HDL entry and simulation and behavioral languages).
- PCB tools (Include layout editors, routing tools, and design rule checkers).

INDUSTRY DESIGN AND MANUFACTURING PRACTICES

EDA tools have been successfully used by many companies representing a wide range of industries including automotive, communications, semi-conductors, aerospace, and computers. A review of articles reporting the results of using EDA tools by more than 23 different companies revealed that in addition to handling complex designs, the use of EDA tools reduces development time by up to 75%, decreases cost by up to 50%, and improves product quality significantly.

In spite of the many advantages of EDA tools, it is estimated that only 35% of all designers use them. Furthermore, a 1996 survey by Integrated System Design Magazine [13], completed by 140 EDA users, revealed that not all users take full advantage of the capabilities of EDA tools. The results of the survey are shown in Figure 2. As can be seen in the Figure, schematic entry is still used in twice as many design groups as HDL entry.

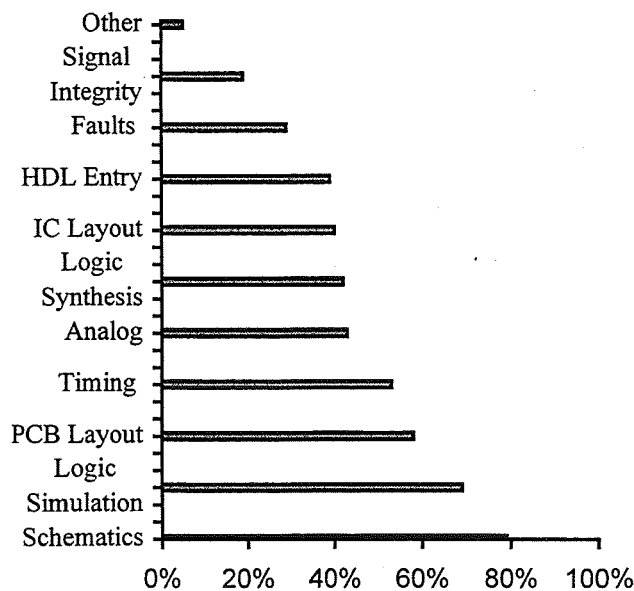


Figure 2.- Percentage Use of EDA Tools for Various Design Functions

Data from the same survey (see Figure 3) indicate that schematic entry is the most time-consuming task. While HDL entry and logic synthesis combined required only 10% of the design cycle, schematic entry requires 23%. This implies that HDL-based design implementations are more efficient than schematic entry approaches.

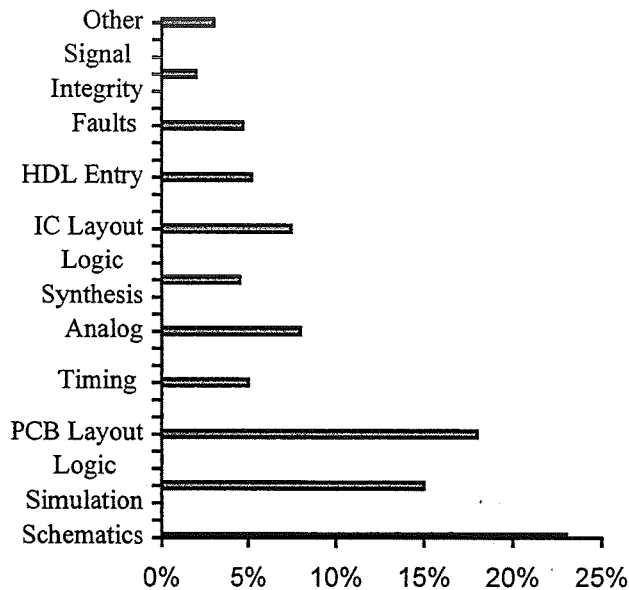


Figure 3.- Percentage of Total Design Time Used for Each Process

As electronic equipment becomes more complex, the capital and technical requirements of electronics manufacturing increase. As a result, many original equipment manufacturers are focusing on product development and using contractors for manufacturing [14]. The Institute for Interconnecting and Packaging of Electronic Circuits (IPC) forecasts that contract manufacturing will grow 20% annually through the year 2000. It is anticipated that by 1997, about 30% of all expenditures for PCB assembly will go to contract manufacturers. To decide whether to create manufacturing capability in-house or outsource, a number of business and technical issues must be assessed to ensure that the allocation of assets best matches the goals established for the organization. The financial ability to invest in manufacturing and the anticipated returns on investment are two major factors that should be considered.

DESIGN AND MANUFACTURING CAPABILITIES AT JSC

To assess the current JSC electronic design and manufacturing procedures and capabilities, I interviewed designers working on different projects in EM, EV, and ER. All the individuals I met were very helpful and exhibited a high level of dedication and professionalism. It was obvious however, that there are some weaknesses in the design capabilities and procedures. The following is a list of observations:

- There is lack of communication and coordination between different design groups.
- There are no standard manufacturing procedures.

- There is no standard software package (Software used include OrCAD, AutoCAD, VIEWlogic, Protel, CADSTAR).
- There are no electrical or mechanical simulation capabilities of complete systems -- Software is used mainly for schematic entry.
- There is duplication of work.
- The majority of individuals support the consolidation of the electronic design functions.
- The majority of individuals prefer in-house PCB rapid prototyping capabilities.
- Some individuals prefer in-house electronic manufacturing capabilities.

CONCLUSION AND RECOMMENDATIONS

The use of EDA tools based on concurrent engineering methodologies that support software-hardware co-design, virtual prototyping, and rapid prototyping is essential for a successful electronics design and manufacturing operation. To improve the current design and manufacturing functions at JSC, the following actions should be implemented:

- Form an overseeing committee that coordinates efforts regarding planning, training, software, hardware, etc. The committee must be derived from all major design groups at JSC to guarantee competent planning and effective communication.
- Acquire EDA tools that offer simultaneous access to all design teams (electrical, mechanical, manufacturing, etc.) and have the following capabilities: Schematic capture, HDL, electrical and mechanical simulations, PCB layout and simulation.
- Establish an EDA support center responsible for processes/procedures, training, technical support, integration of design tools, network administration, library development, equipment upgrading, licenses, etc.
- Consolidate the electronic manufacturing operations -- All orders are submitted to a centralized facility.
- Provide proper training for all technical personnel -- This is very crucial for a smooth and successful transition to the new environment.
- Maintain PCB rapid prototyping capabilities -- Communicate information to all customers and provide quality products.
- Postpone the decision regarding establishing in-house manufacturing capabilities until the electronic design functions are consolidated

The transition from the current structure to an integrated design environment can be completed within two years. This aggressive schedule assumes the support and commitment of everyone involved in the process. Acquiring EDA tools, developing procedures, and providing training may be carried out in five phases as follows:

I. Pre-Planning (1 month)

- Identify individuals who should be involved in the planning phase -- Project managers, design engineers, software specialists, etc.

II. Planning (4 months)

- Identify JSC design and manufacturing needs -- Survey designers, managers, technicians, and other appropriate technical personnel.
- Specify required design capabilities (software and hardware).
- Select software and hardware that satisfy the required design capabilities.
- Order hardware and software.
- Develop some design procedures based on concurrent design methodologies.
- Identify a pilot project and select the first group of individuals for training.

III. Equipment Procurement and Installation (1 month)

IV. Initial Training (3 months)

- Provide proper training to a group of 12 individuals including those who will constitute the support group.

V. Pilot Project (6 to 12 months)

- Implement design procedures and processes.
- Develop library.
- Refine processes and procedures.

VI. Full Conversion to the New Environment (12 months -- Start 3 months after pilot project begins) -- 40 to 50 people

- Provide proper training to groups of eight to ten designers at a time.
- Provide support at all levels in the design process.
- Continue developing library and revising processes and procedures.

REFERENCES

- [1] K. Lai, "A New Dawning in EDA," Integrated System Design Magazine, June 1996.
- [2] G. Zach and J. Wilson, "An Evolution in System Design and Verification," ISD Magazine, March 1996.
- [3] S. Schulz, "Trends in Simulation and Synthesis," ISD Magazine, September 1995
- [4] P. Clemente, R. Crevier, and P. Runstadl, "RTL and Behavioral Synthesis: A Case Study," VHDL Times, Vol. 5, No. 1, 1996.
- [5] B. Barrera and T. Feist, "FPGAs Streamline Design Process," EE Times, April 22, 1996.
- [6] E. King, "Virtual Prototype Finds Design Flaws," ISD Magazine, May 1996.
- [7] R. T. Maniwa, "Putting it Together: Prototyping Methods," ISD Magazine, September 1995.
- [8] A. Borriore and A. Pincetti, "Virtual Prototyping Proves Real Asset," EET Times, January 22, 1996.
- [9] S. Gilbrech, "FPGA Flexibility Enables Concurrent Board Design and Layout," ISD Magazine, March 1996.
- [10] R. Maniwa, "Focus Report: Formal Verification, Cycle-Based Simulation, Timing Analysis, and ESL Entry," ISD Magazine, June 1996.
- [11] N. Barkus and G. Hinde, "EDA's Impact on the Design Process," Printed Circuit Design, pp. 26-29, June 1995.
- [12] J. Smith, R. Tomasek, M. Jin, and P. Wang, "Integrated System Simulation," Printed Circuit Design, February 1995.
- [13] S. Schulz, "Results of the 1996 USE/DA Survey on EDA Business Practices," ISD Magazine, June 1996.
- [14] G. Derman, "Manufacturing Technologies Interconnects Packaging," EE Times, June 13, 1994.

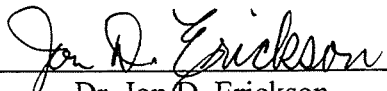
294257

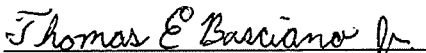
14p.

DEVELOPMENT OF METHODS TO EVALUATE SAFER FLIGHT
CHARACTERISTICS

Thomas E. Basciano Jr.
University of Cincinnati
ER2
August 24, 1996

Jon D. Erickson, Ph.D.
Simulation & Graphics Branch
Automation, Robotics, and Simulation Division
Engineering Directorate


Dr. Jon D. Erickson


Thomas E. Basciano Jr.

53-03
038284

DEVELOPMENT OF METHODS TO EVALUATE SAFER FLIGHT
CHARACTERISTICS

Final Report
NASA / ASEE Summer Faculty Fellowship Program - 1996
Johnson Space Center

Prepared by : Thomas E. Basciano Jr.
Academic Rank : Undergraduate Student
University & Department : University of Cincinnati
Aerospace Engineering
Cincinnati, Ohio 45221
NASA / JSC
Directorate : Engineering
Division : Automation, Robotics and Simulation
Branch : Simulations and Graphics
JSC Colleague : Jon D. Erickson, Ph.D.
Date Submitted : August 24, 1996
Contract Number : NAG 9-867

ABSTRACT

The goal of the proposed research is to begin development of a simulation that models the flight characteristics of the Simplified Aid For EVA Rescue (SAFER) pack. Development of such a simulation was initiated to ultimately study the effect an Orbital Replacement Unit (ORU) has on SAFER dynamics. A major function of this program will be to calculate fuel consumption for many ORUs with different masses and locations. This will ultimately determine the maximum ORU mass an astronaut can carry and still perform a self-rescue without jettisoning the unit. A second primary goal is to eventually simulate relative motion (vibration) between the ORU and astronaut. After relative motion is accurately modeled it will be possible to evaluate the robustness of the control system and optimize performance as needed.

The first stage in developing the simulation is the ability to model a standardized, total, self-rescue scenario, making it possible to accurately compare different program runs. In orbit an astronaut has only limited data and will not be able to follow the most fuel efficient trajectory; therefore, it is important to correctly model the procedures an astronaut would use in orbit so that good fuel consumption data can be obtained. Once this part of the program is well tested and verified, the vibration (relative motion) of the ORU with respect to the astronaut can be studied.

INTRODUCTION

With the construction of the International Space Station in the near future, the risk to astronauts performing extravehicular activities (EVAs) rises greatly. Not only will the frequency of EVAs increase, adding to the possibility of a “break away”, but the station will not be able to retrieve the astronaut if such an event occurs. This problem prompted NASA to develop the Simplified Aid For EVA Rescue (SAFER) maneuvering unit which would allow the astronaut to perform a self-rescue.

The SAFER pack is a self-contained unit which attaches to the Primary Life Support System (PLSS) on the space suit. It consists of 24 cold gas nitrogen thrusters which allow for six degree of freedom maneuvering. In addition, the SAFER unit also includes an Automatic Attitude Hold (AAH) system that nulls any undesired angular velocities. The AAH is initiated by the astronaut after the hand controller is deployed from its stowed location in the base of the SAFER unit. This will detumble the astronaut, at which point the station can be located and then the astronaut can translate back to the point of separation.

The SAFER pack was tested on STS-64 and performed admirably. However, in the future astronauts will be asked to carry Orbital Replacement Units (ORUs) and tools into position on the station, which will undoubtedly change the flight characteristics of the SAFER unit. An example of such a situation, where ORUs were carried by astronauts, occurred during the STS-76 mission where the astronauts carried and attached Mir Environmental Effects Payloads (MEEPs) to the Mir docking module (Figure 1). If an astronaut were to become separated from the station, the optimum situation would be to keep the ORU tethered. Keeping the ORU tethered would prevent the harm a jettisoned ORU could do to the station, as well as saving a valuable piece of equipment from drifting into space. The addition of these extra tethered units will obviously change the flight characteristics a great deal, affecting the ability of the astronaut to perform a self rescue. Not only will the mass offset affect the flight dynamics but also the vibration, or relative motion, of the ORU with respect to the astronaut will cause undesired effects. Relative motion was observed with the structure of the Manned Maneuvering Unit (MMU), which led to double the calculated fuel consumption. The SAFER unit was carefully constructed to avoid problems with relative motion, however, a small amount of relative motion was recorded on STS-64 (Figure 2). This motion was mostly attributed to the reaction of the astronaut's body with the space suit and movement of the limbs, and posed no problem for the superior SAFER control system. Unfortunately, with the addition of the tethered ORU this relative motion once more becomes important.

Currently, the only place engineers can run simulations is the Virtual Reality lab (VR lab) at NASA Johnson. The VR lab is an excellent training facility with full

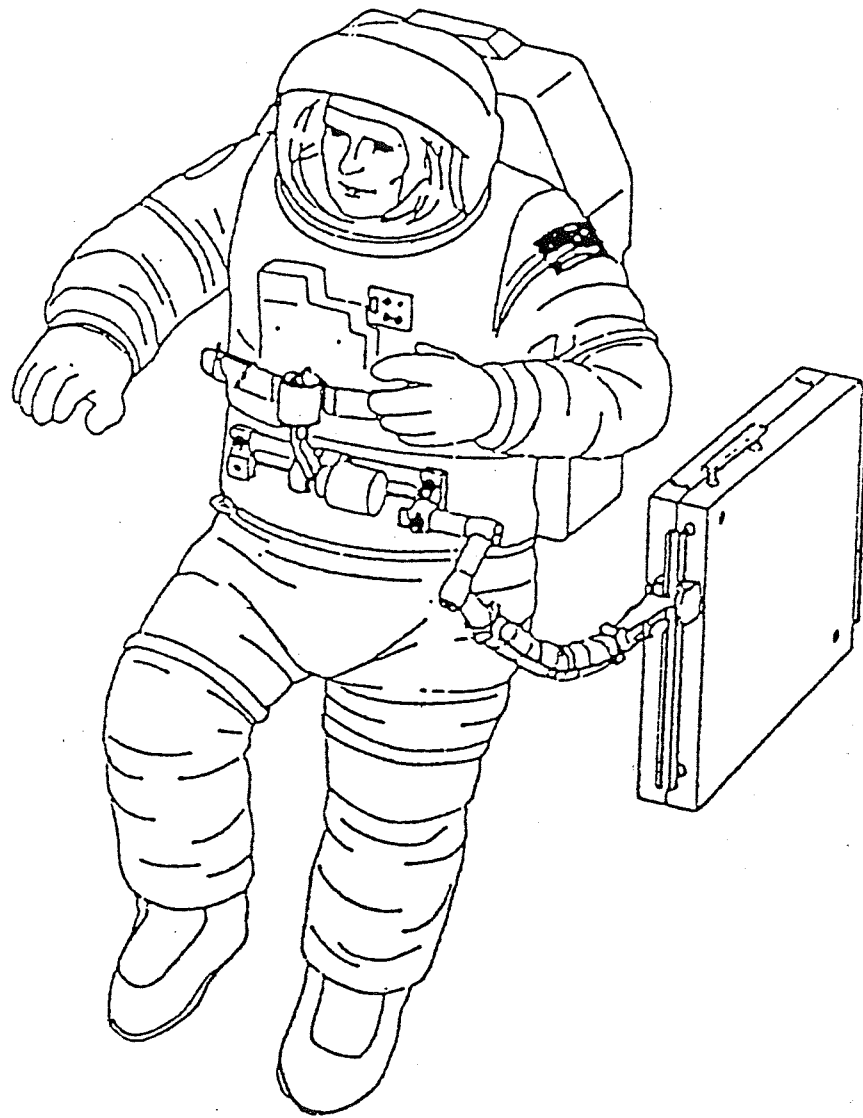


Figure 1. - Crewmember translating with a MEEP.

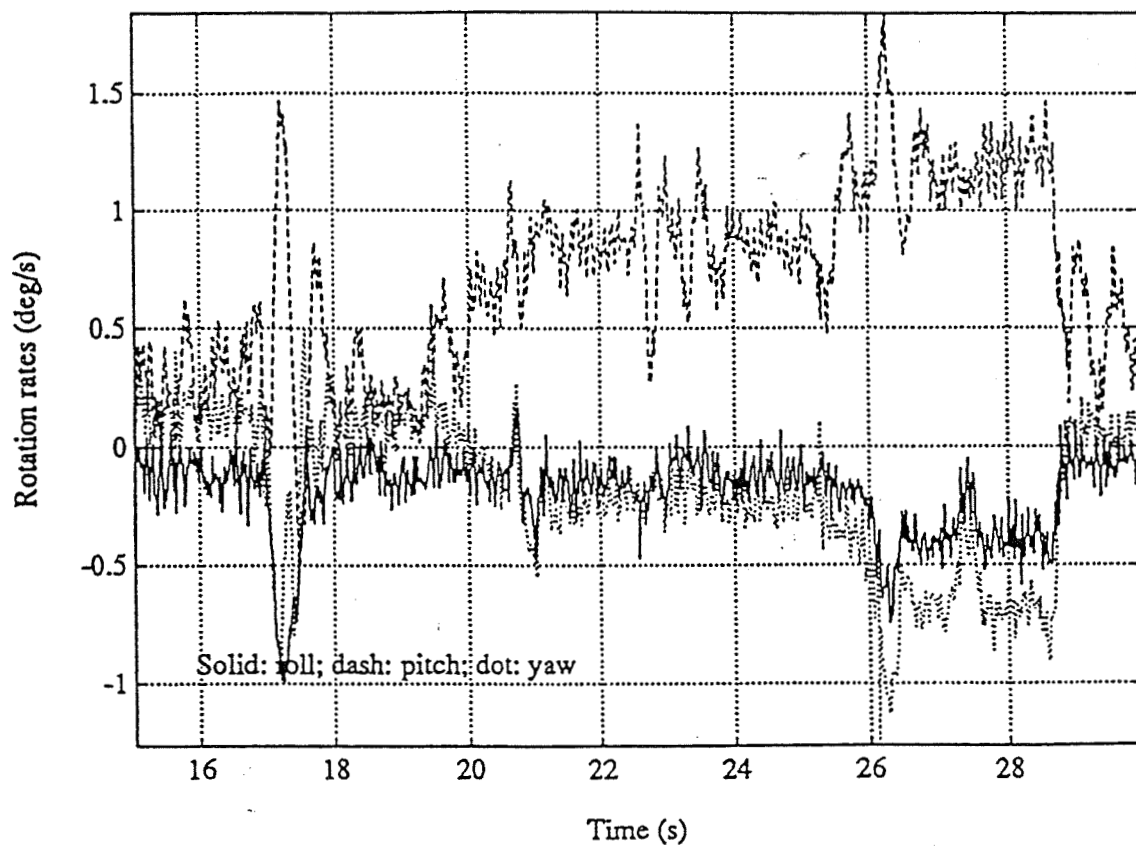


Figure 2. - STS-64 EV2 Engineering Evaluation positive x maneuver

animation and virtual reality capability. There are several problems with using the VR lab for the proposed relative motion study. First, the parameters in VR lab program are not easy to modify. Second, down time in the simulator reduces the amount of training time the astronauts receive. Finally, data from the runs is not easily accessible or directly comparable because commands to the SAFER simulation must be input manually, and human error can cause significant differences for one run to another. It is apparent that using the VR lab for engineering studies is not practical and would cut into valuable time for astronaut training. To alleviate the mentioned problems and to allow study of various engineering parameters, it is obvious that a new program will need to be developed.

For the effects of an ORU (including relative motion) to be studied accurately a standardized full self-rescue scenario must be modeled. Generally, a standardized full rescue scenario will allow quantitative comparison between runs. The most important comparison is fuel consumption, which will determine ultimately whether or not the astronaut will be able to return to the station. However, this program will also need to display angular velocity, attitude, velocity, and position information to evaluate control system performance. Of course, the program will be flexible enough for the user to easily vary several different parameters to evaluate and optimize performance.

SELF RESCUE

Modeling a full self-rescue scenario, starting with initial conditions at break away and finishing with return to the point of separation, is a critical part of simulation development. As mentioned previously, this scenario will allow accurate comparison between program runs. At first this may seem like an easy task; however, the difficulty arises with using only the limited visual clues available to the astronaut in orbit. Most likely the astronaut will not be able to use the most fuel efficient trajectory to return to the station. It is imperative to model the correct trajectory, as it will be executed in orbit, to obtain good fuel consumption calculations.

Modeling of a standardized self rescue procedure consists of several different phases currently based on separation rates observed in KC-135 tests and time estimates of procedures studied in VR lab simulations. The first phase is initial drift time. This takes into account the time an astronaut takes to realize what has happened, stow carried equipment, and deploy the SAFER hand controller. The next stage is the deceleration phase, which consists of the AAH counteracting any angular velocities that may be present from the separation. After angular velocities have dropped sufficiently (below the control system deadband) the astronaut must locate the station. Because of vision limitations and the position after the detumble, it is likely the astronaut will not immediately see the station, or know where it is located relative to the current position. Locating the station is achieved by performing, at most, a 360° pitch and then a 360° yaw. Somewhere in this range the astronaut will be able to see the station. Finally, the astronaut can translate back to the station. This is the most difficult part of the scenario

to model, because orbital mechanics take effect. The most fuel efficient trajectory to use is described by the Clohessy - Whiltshire (CW) targeting equations. A CW burn is precisely initiated along a vector angled away from the Line Of Sight (LOS). However, the astronaut does not have precise velocity or position information. Finding the correct angle for the CW burn would be no more than a guess. Conversely, if the astronaut initiates a burn along the LOS, the only vector he has accurate information on, he ends up far from the station. An example of these orbital effects is shown in Figure 3; the outbound trajectory is solid, a correct CW burn dashed, and burn of the correct CW magnitude directed along the Line Of Sight (LOS) is dash dot.

The solution to this problem is to use inertial LOS targeting [3]. This uses more fuel than CW, but makes use of limited visual clues in orbit to get the astronaut back to the station. To initiate inertial LOS targeting a burn is directed along the LOS until desired velocity back toward the station is achieved. Then at regular intervals the astronaut checks the position of the station relative to the stars. If the station has drifted more than some allowable distance with respect to the stars, the astronaut applies thrust for some predetermined interval (based on mass) perpendicular to the LOS and in the same direction as the drift.

RESULTS

The first part of the simulation, up to the inertial LOS targeting, has been successfully programmed and reasonable comparisons can be drawn from the information. Figure 4, and Figure 5 display angular velocity for two different cases. Figure 4 was run with the mass properties for a large astronaut based on data obtained from training data. Figure 5 was produced by adding the mass properties of a 50 kg ORU to the astronaut mass properties. The initial break away conditions were angular velocities of 30 deg/s about each axis and 2.5 ft/s translation in the X direction. The 30 deg/s is a worst case value used by NASA to evaluate performance. In both cases the initial drift time, the time between break away and initiation of the AAH, was 30 seconds. Once the angular velocities have been significantly reduced, the astronaut will begin the process of locating the station by means of a 360° pitch and 360° yaw. To keep the total drift time, time between initial break away to start of translation, to a minimum the "recommended" time to complete the search procedure has been set at about 50 seconds. This leaves 25 seconds for the 360° pitch maneuver and the other 25 seconds for yaw, which corresponds to maintaining an angular velocity of approximately 15 deg/s for 25 seconds. Examining the figures, it is apparent that the graphs are quite similar, due to the standardization of the self-rescue routine. With all parameters controlled it is possible to accurately compare the fuel consumption between the two runs. The fuel consumed in Figure 4 is 0.2679 kg while that of Figure 5 is much greater at 0.7972 kg., which is as we expected. The farther the center of mass is displaced from the designed center of mass, the more the thrusters, which are no longer optimized, must work to perform maneuvers.

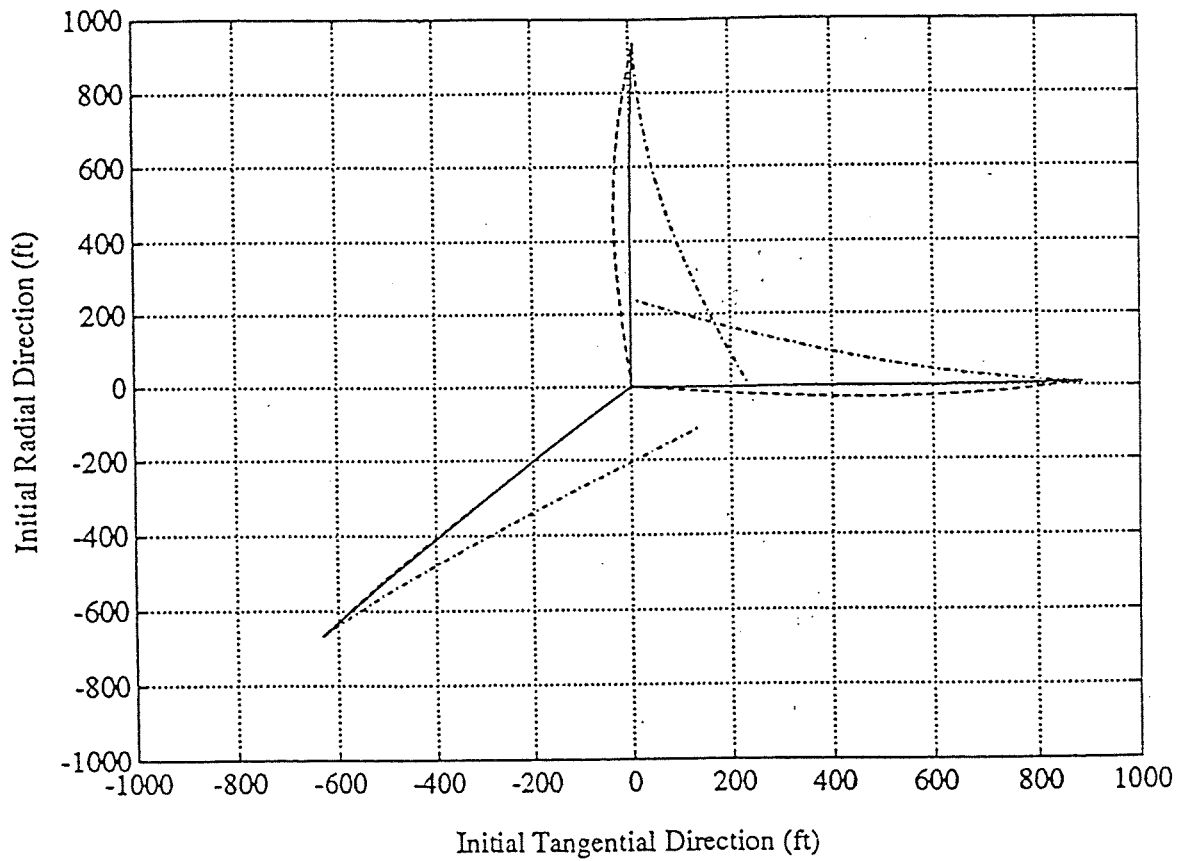


Figure 3. - Trajectories in non-rotating coordinates

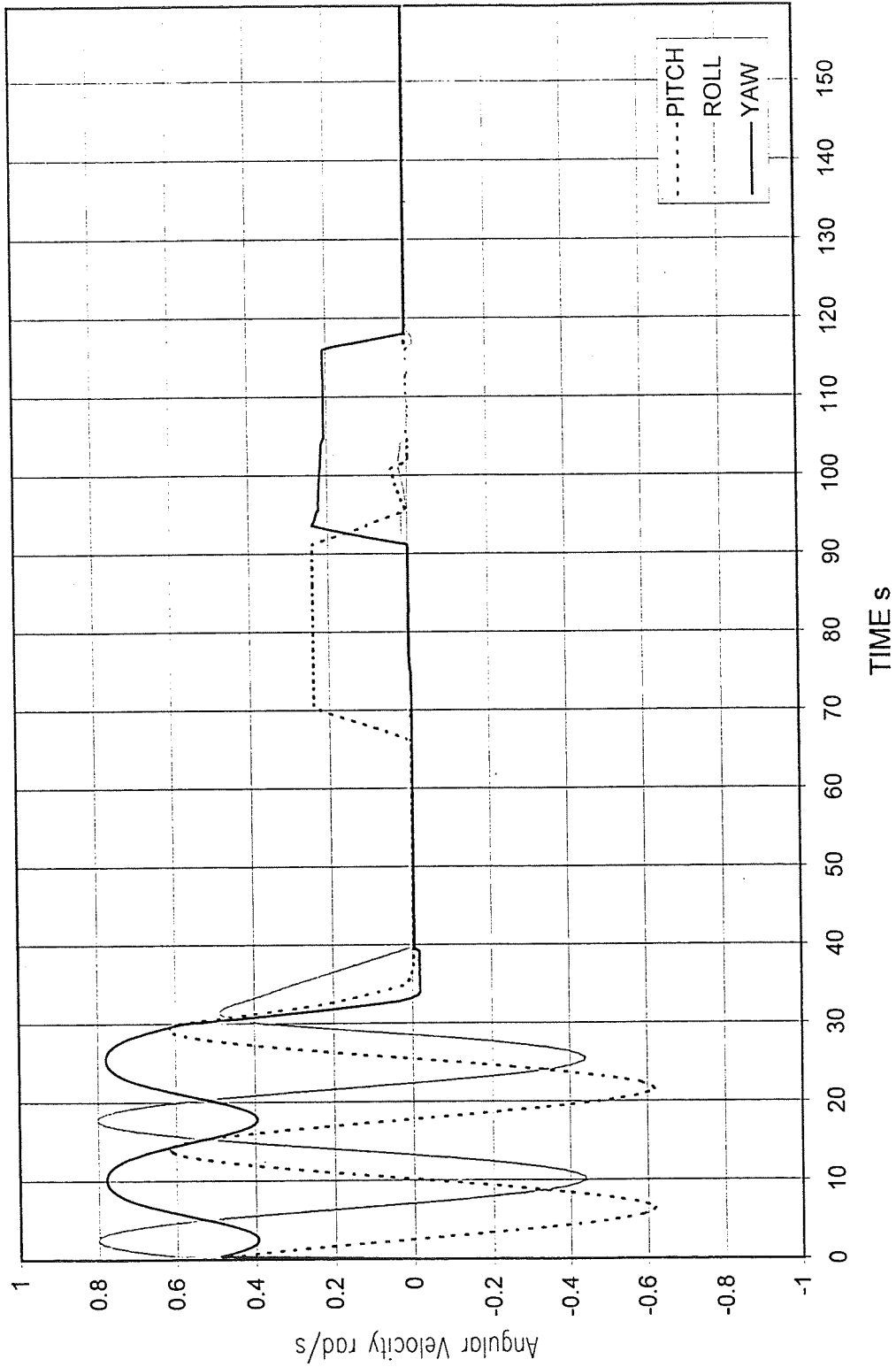


Figure 4. - Angular rates for an astronaut without an ORU

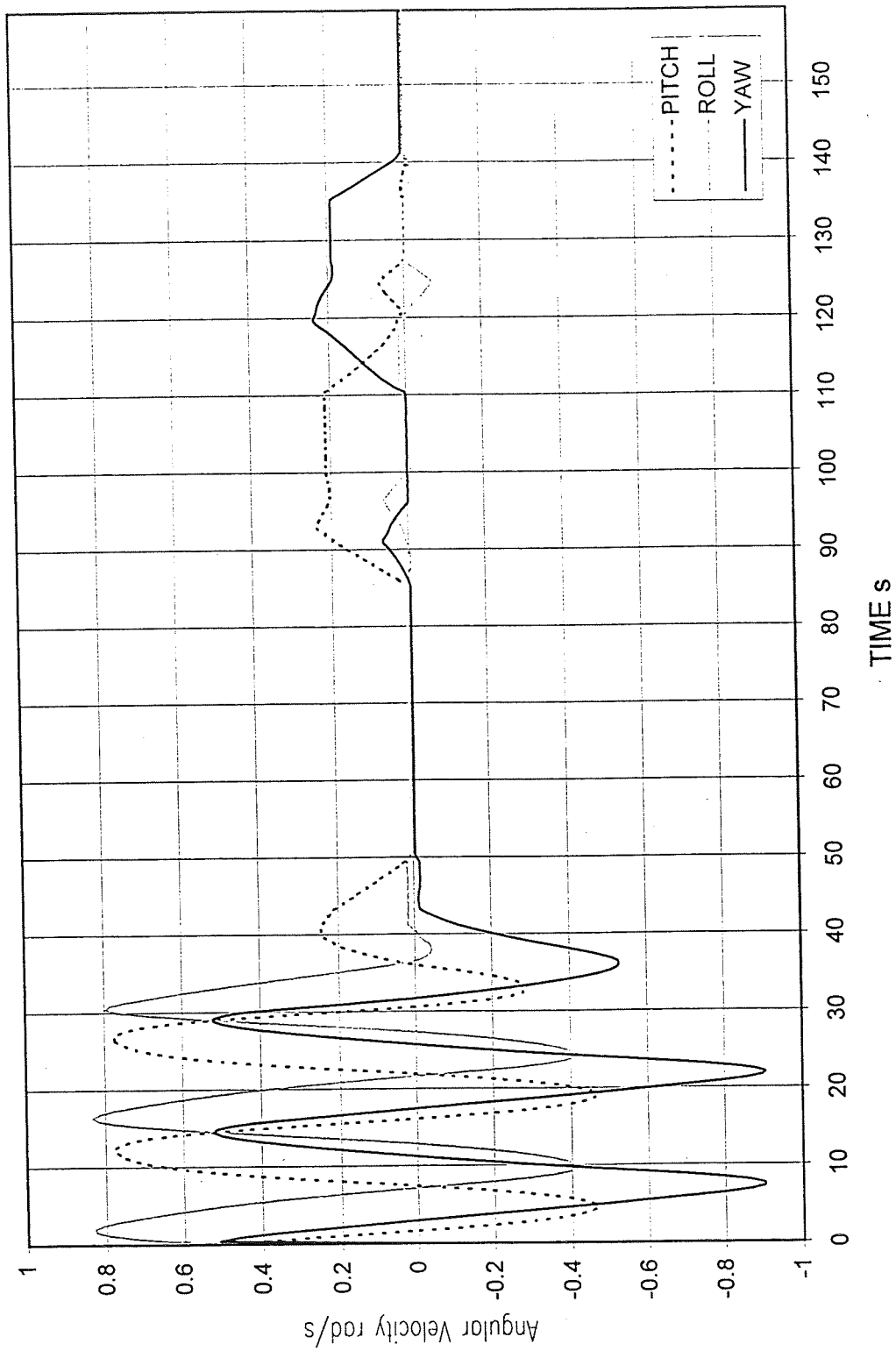


Figure 5. - Angular rates for an astronaut with a 50 kg. ORU

A closer examination of the angular velocities for the station search procedure reveals that the effects of cross-coupling are clearly present in Figure 5; these effects obviously cause the control system to use more fuel.

These cases are very simple, but illustrate the capability that the finished program will give to the engineer. After seeing the effects of cross-coupling in the angular velocity plots the engineer may decide that a more aggressive control system will need to be designed. The fuel consumption figures will also allow the engineer to make recommendations on the maximum mass that the astronaut can safely carry. The mass properties used for Figure 5 were based on an ORU carried to the left of and behind the astronaut. By simply typing in a new ORU location, the engineer will be able to find the optimum, or most fuel efficient, position of the ORU.

CONCLUSION

Based on the work thus far it is evident that a portable, flexible program could be used quite effectively to analyze SAFER flight characteristics. Based on the preliminary data, NASA has expressed interest in continuing code development. By the end of this year the modeling of relative motion should begin; however, good data on the effects of ORUs on SAFER dynamics will have been obtained. Modifying these values by some safety factor, will give moderate accuracy and assure safety of the astronauts, until relative motion can be researched in more detail.

As construction of the International Space Station draws near, it will become very important to find the limits of the SAFER unit so that recommendations on ORU mass and position can be made. As more research is conducted it will be possible to understand the causes of relative motion and model them with increasing accuracy. To verify this final stage of the program it is inevitable that empirical data will need to be collected. Air bearing floor and KC-135 tests seem the most likely candidates to obtain precise results. Until this empirical data can be collected, a good routine can be developed using estimated quantities. As new data is uncovered the simulation will be refined.

REFERENCES

- [1] "Simplified Aid for EVA Rescue (SAFER) Operations Manual", JSC-26283, NASA Johnson Space Center, Sept., 1994.
- [2] Williams, T. W., Tanygin S. and Bolender L., "SAFER Mass Properties Determination: Results from On - Orbit Data", ASS Paper 95-339, Aug. 1995.
- [3] Baugham, D. and Williams, T. W., "Self - Rescue Strategies for EVA Crewmembers Equipped with the SAFER Backpack", NASA Conference Publication 3265, pp. 357 - 371, May 1994.
- [4] "Manned Maneuvering Unit Operational Data Book", MMU-SE-17-73 Rev. B., Martin Marietta, July 1985.
- [5] "Quaternion Supplemental Workbook", QUAT-S 2102, Johnson Space Center, November, 1984.
- [6] Williams, T. W., "On - Orbit Mass Properties Determination for the SAFER / Astronaut System", AAS Paper 94-187, 1994.

MEASUREMENT OF CARBON DIOXIDE ACCUMULATION AND
PHYSIOLOGICAL FUNCTION IN THE LAUNCH AND ENTRY AND
ADVANCED CREW ESCAPE SUITS

54-54
038-285

16 p.

294259

Final Report

NASA/ASEE Summer Faculty Fellowship Program--1996
Johnson Space Center

Prepared by: Phillip Bishop, Ed.D.

Academic Rank: Professor

University and Department University of Alabama
Dept. of Human Performance
Studies, Tuscaloosa, AL

NASA/JSC
Directorate: Space and Life Sciences

Division: Medical Sciences

Branch: Space Biomedical Research
Institute, Exercise
Countermeasures Project

JSC Colleague: M.C. Greenisen

Date submitted: 10 July 1996

Contract Number: NAG9-867

Approved by: Michael C. Greenisen

Date of Approval: 02 July 96

MEASUREMENT OF CARBON DIOXIDE ACCUMULATION AND
PHYSIOLOGICAL FUNCTION IN THE LAUNCH AND ENTRY AND
ADVANCED CREW ESCAPE SUITS

Final Report

NASA/ASEE Summer Faculty Fellowship Program--1996
Johnson Space Center

Prepared by:	Phillip Bishop, Ed.D.
Academic Rank:	Professor
University and Department	University of Alabama Dept. of Human Performance Studies, Tuscaloosa, AL
NASA/JSC Directorate:	Space and Life Sciences
Division:	Medical Sciences
Branch:	Space Biomedical Research Institute, Exercise Countermeasures Project
JSC Colleague:	M.C. Greenisen
Date submitted:	10 July 1996
Contract Number:	NAG9-867

ABSTRACT

The Launch and Entry Suit (LES) and Advanced Crew Escape Suit (ACES) are worn by astronauts for launch and entry. Previous work by Waligora, et al., 1992, Waligora and Gilbert, 1992, and Dalrymple 1996, have found that carbon dioxide (CO₂) accumulation in the LES/ACES helmet may be problematic. CO₂ accumulation is important because high inspired levels of CO₂ reduce physical function and pose a safety hazard (e.g. levels of CO₂ accumulation of 3.6% in the Extravehicular Mobility Unit are sufficient to terminate Extra Vehicular Activities). My task was to design a suitable test protocol for determining the important physiological aspects of LES/ACES use. Three basic issues arose. First was the determination of the astronaut's CO₂ inspiration during visor-down use at rest and during walking at 3.5 mph. A sub-issue was the impact of a pneumotach on CO₂ since it has been previously observed that when the Aerosport pneumotach was used, performance seemed improved, which might be attributable to a lowered respiration rate when using the pneumotach. The second issue was the energy costs of walking in the LES/ACES with various G-suit inflation levels, since G-suit inflation increases metabolic costs and metabolic costs influence the CO₂ production in the LES/ACES helmet. Since G-suit inflation improves orthostatic tolerance after space flight, but likely increases the energy costs of walking, the balance between G-suit inflation and CO₂ accumulation is an important safety consideration. The third issue which arose from pilot work was the substantial reduction in physical function after a 10 min visor-down period prior to walk.

INTRODUCTION

In the event of an emergency egress after landing, the LES/ACES serves as a protective garment and together with the integrated Emergency Oxygen Supply (EOS) provides safe breathing air. Should a contingency egress be necessary, crew members exit the space craft with the helmet visor down, breathing 100% O₂ from the EOS and walk/run a distance of 400 meters upwind from the vehicle. Previously, a pilot study determined the CO₂ distribution pattern in the non-conformal helmet under simulated emergency egress conditions. During this study, subjects wore the LES with G-suit inflated to 1.5 psi and visor down, inspiring 100% O₂, while attempting a 5 min walk at 3.5 mph on a treadmill (equivalent to 400 meters).

Those pilot study results showed CO₂ build-up in the helmet occasionally exceeded 7.5%. Three of five subjects were unable to complete the 5 min walk. Three subjects complained of O₂ starvation during the study. These results agree with previous unpublished findings by Waligora, et al. 1992, Waligora and Gilbert, 1992, who in preliminary tests found that carbon dioxide (CO₂) accumulation in the both conformal and non-conformal helmets could be problematic. Based on the results of these pilot studies, a follow-up study is proposed. The prior studies suggested there was a potential problem with CO₂ accumulation, but did not compare the Aerosport pneumotach, and did not examine the impact of seated rest immediately before the walk. The 6 min seated rest would represent the best-case scenario since nominal landing procedures at Kennedy Space Center (KSC) require visor-down above a flight altitude of 10k feet (NASA Shuttle entry key cards, NASA Doc. #48019).

OBJECTIVES

To determine if the inspired CO₂ levels are within acceptable ranges during simulated landing and contingency egress:

- 1) What is the % CO₂ inspired and expired while:
 - a) seated quietly for 6 min, visor down, in the LES/ACES (simulating emergency approach and landing period) while breathing 100% O₂?
 - b) treadmill walking at 3.5 MPH for 5 min while wearing the LES/ACES ensemble and breathing 100% O₂?
- 2) What is the % CO₂ inspired and expired during above simulated egress conditions breathing through the Aerosport pneumotach in a manner similar to the Crew Transport Vehicle Locomotion Egress study, Detailed Supplemental Objective (DSO) 331. Observations suggest that the pneumotach effects respiration and gas mixing within the helmet, resulting in lower CO₂ inspiration.
- 3) How does the G-suit inflation level affect the energy costs of walking at 3.5 mph (5.6 km/hr), 0% grade? (Appropriate use of the G-suit during ambulation can only be determined by evaluating the costs and benefits of various G-suit inflations during ambulation).
- 4) What is the impact on performance of a 6 minute visor-down period prior to the walk (simulation of nominal landing procedures at KSC)? And how does a 6 min visor-down rest period affect performance in an immediately succeeding 5 min walk at 3.5 mph (similar to DSO 331 with a simulation of visor-down above 10k feet as per NASA Shuttle entry key cards, NASA Doc. #48019).

METHODS

- 1) Subjects N=12 with physical characteristics similar to the Astronaut Corps will be drawn from the Exercise Countermeasures Project and Crew and Thermal Systems Division.
- 2) Six subjects will be evaluated on each test day. For example, 3 subjects will be tested with the G-suit inflated to 3 clicks (1.5 psi) and the other half at 0 clicks (each "click" adds 0.5 psi pressure to the G suit).

3) Another set of six subjects will be completed on a successive day; half of the subjects will be tested at 3 clicks of G-suit inflation (1.5 psi) and the other half at 0 clicks. All G-suit inflation levels will be counterbalanced to avoid ordering effects.

4) On subsequent test days, subjects will be retested in untested G-suit configurations and rest/walk sequencing (i.e. a crossover design). This will give us some test-retest reliability information because some aspects of the test such as seated rest in the LES/ACES will be replicated exactly.

Goal -- at least 10-12 subjects completed in a month.

Test Protocol

1) Subject will be weighed and instrumented with a heart rate (HR) monitor, skin and rectal thermocouples and then will don the LES/ACES. Subject will don a specially configured LES/ACES helmet with one CO₂ sampling capillary located on the microphone boom of the communications headgear as close as practical to the mouth/nose routed through the special Aerosport helmet adapter (with the other adapter openings sealed). Or, for Aerosport pneumotach tests, a sampling capillary will be located at the pneumotach opening to determine the impact of the pneumotach on inspired CO₂. This is needed to determine the influence of the pneumotach since it has been observed that the pneumotach appears to positively influence the visor-down walk ventilatory performance. This measure could lead to a solution to anticipated high inspired CO₂ levels by altering the ventilation pattern because of the resistance, thereby reducing hyper-ventilation. The pneumotach/no-pneumotach order of trials will be counterbalanced.

Subject will not be cooled, and G-suit will be inflated to the appropriate G-suit inflation pressure during all walks. All walks will be at 3.5 mph with visor down, breathing 100% O₂ until a subject reaches one of the limiting criteria:

- a) Completion of 5 min. walk
- b) Upon subject request
- c) Upon reaching 6% inspired CO₂ level
- d) Achievement of 90% of age-predicted HR max.

2) After all instruments are functionally verified, subject will be evaluated in one of the following tests:

Phase I- Immediately after visor-down, subject will walk with (or without, in counterbalanced order) the pneumotach for 5 min, and CO₂ and respiratory rate will be monitored to determine the impact of the pneumotach on performance and inspired CO₂ levels. G-suit will be inflated to 0 or 1.5 psi in counterbalanced order. The two different G-suit inflations will be tested on different days.

Phase II- Subjects will perform 6 min of seated rest immediately prior to walking as in Phase I, except the two G-suit pressures will be 0.5 and 1.0 psi (counterbalanced order). No helmet ventilation will be provided between the rest and walk to simulate an egress evacuation of the shuttle with appropriate CO₂ accumulation prior to the walking phase. The two different G-suit inflations will be tested on different days with order counterbalanced.

Phase III- Replication of Phase II with 0 and 1.5 psi G-suit inflation, in counterbalanced order.

3) Following each Phase walk, the visor will be immediately opened, and the subject will be connected to the suit cooling system.

4) When the subject is ready, she/he will walk again at 3.5 mph at the G-suit inflated to the appropriate pressure for that test Phase, visor up, in order to determine the energy costs of LES/ACES locomotion with the G-suit setting at 0 through 1.5 psi. The additional energy costs of walking with the G-suit inflated can thereby be determined. After this walk which will require approximately 3 to 5 min, subject will again be seated and permitted to recover.

Rest periods between any two test walks will be a minimum of 10 minutes. However, subjects may recover as long as they desire. Liquid cooling and drinking water will be provided during rest.

CO₂ will be measured continuously with the Perkin-Elmer mass spectrometer whose analog outputs are connected to a CODAS data collection system. VO₂ will be measured with the Aerosport (only in the visor-up configuration). Temperatures will be measured with the Squirrel data collection system. Data collection sheets are shown in Appendix A.

Preliminary results

A pilot study of LES/ACES helmet CO₂ accumulations was conducted on three subjects during June 1996. The first two subjects, "A" and "B" were measured walking with and without the Aerosport mouthpiece and during rest. The complete LES was not worn, but only the neck dam and helmet supplied with 100% O₂. The treadmill was elevated to elicit a metabolic rate of 1.7 L/min, similar to the LES with G-suit not inflated (Barrows, et al., 1995), but speed was kept at 3.5 mph. The third subject, "#1" was fully outfitted with G-suit inflated to 1.5 psi. The entire Phase I protocol as proposed was completed with G-suit at 1.5 psi. Findings for the helmet-only simulation are displayed in Table 1.

Table 1. Pilot study results for helmet-only simulation.

Subject (trial)	Inspired CO ₂ at rest (%):				
	min1	min2	min3	min4	min5
A (w/o pneum)	1.6	1.6	1.8	1.7	1.6
A (w pneum)	1.6	1.7	1.6	1.6	1.6
B (w/o pneum)	2.0	1.8	2.2	2.1	2.0
B (w pneum)	2.0	1.9	1.9	1.8	1.9
Subject	Inspired CO ₂ during 3.5 mph walk (%):				
Subject	min1	min2	min3	min4	min5
A (w/o pneum)	2.5	2.7	3.0	3.1	3.5
A (w pneum)	2.3	2.9	3.4	3.3	3.2
B (w/o pneum)	2.5	2.9	2.7	2.7	2.8
B (w pneum)	2.3	2.5	2.7	2.9	3.0

The actual LES pilot walk was conducted on 26 June 1996. A full LES inflated to 1.5 psi was used. The subject was healthy, highly fit and experienced in LES use. After 30 sec of visor-down 10 min rest period, CO₂ inspired had risen from a nominal 0.3% (ambient) to an average of 1.6 (sd=0.21)% (regardless of pneumotach use). During the last 2 min of rest, inspired CO₂ was 1.6 (0.16) (regardless of pneumotach use). This indicates high test-retest reliability for this phase of testing.

Without the pneumotach, immediately following the 10 min rest period, the subject was able to walk only 100 seconds at 3.5 mph. Average inspired CO₂ over the whole walk was 3.0% (0.84). With the pneumotach, the subject was able to walk only 120 seconds at 3.5 mph. Average inspired CO₂ was 2.3 (0.63)%. Average respiratory rate was 27.3 breaths per min without the pneumotach, and 23.6 with the pneumotach. In both walks, heart rate reached about 160 bpm (84% of predicted maximum). On a previous occasion under the same conditions, this subject was able to walk 300 seconds without the 10 min visor-down rest immediately preceding the walk (from Dalrymple, in progress).

Based upon all these pilot results it was concluded that during the walking part of the test, the pneumotach appears to reduce the inspired CO₂ (by 30%) and respiratory rate (by 16%), and slightly increase endurance (by 20%). Although this effect was not clearly seen in the simulation (Subjects A and B), in the actual LES the pneumotach appears to exert some effect. Both subjects, A and B were able to complete 5 min walk in the helmet alone. Most importantly, in the LES, the 5 to 6 min period which might be expected between visor-down order on the Kennedy Space Center landing checklist and the start of contingency egress could reduce performance capabilities.

Expected findings

Based upon the above pilot work and that of previous investigators, it is anticipated that the following will be observed:

a) That inspired CO₂ levels will rapidly exceed 1% under all conditions and will exceed 4% in most subjects during walking. The

rise in CO₂ will be proportional to the metabolic rate. In the EMU, 3 to 8 mmHG of CO₂ with symptoms, or greater than 8 without symptoms, terminates EVA. At EMU pressure (4.3 psi or 222 mmHG), 3 mmHg of CO₂ is equivalent to 1.3%, and 8 mmHg of CO₂ is equivalent to 3.6%. The impact of 1-4% CO₂ on physical performance during LES/ACES walking is unknown.

b) That the use of the Aerosport pneumotach will reduce the ventilation rate such to slow the rate of increase in inspired CO₂ and increase performance.

c) That the metabolic costs of G-suit inflation will be significantly higher and linearly increase with G-suit inflation pressure (i.e. the energy costs of walking with 0.5 psi G-suit inflation will be substantially higher than 0 psi).

d) It is anticipated that a substantial number of rested, fit, 1G-acclimatized subjects will be unable to walk 5 min at 3.5 mph, with the visor down and G-suit inflated to 1.5 psi. The 6 min visor-down rest period will further reduce the walk-completion success rate for all G-suit levels.

DISCUSSION

Comparisons between the pressure suits worn by military pilots of high-altitude aircraft and US astronauts could be potentially misleading. The USAF SR-71 pressure suit is similar to the LES/ACES. However, the SR-71 suit has no neck dam, and uses a conformal helmet with less dead space and an exhale port near the mouth. The LES/ACES has a neck dam, and uses a non-conformal helmet. Aircrews generally spend the majority of their time sitting quietly and in emergency they eject. In contrast, in contingency egress, Shuttle crews must physically leave the shuttle under their own power. Active egress is a crucial safety issue.

REFERENCES

Barrows, LH, JJ McBrine, JC Hayes, MD Stricklin, and MC Greenisen. Physiological responses to wearing the space shuttle suit and the prototype advanced crew escape suit compared to the unsuited condition. NASA Tech., Paper 3297

Dalrymple, G, N Packham, MC Greenisen. CO2 distribution patterns in the LES helmet during walking at 3.5 mph. NASA Tech. Paper in progress.

Waligora, JM, K V Kumar, S Freeman-Perez, LL Hnatt and DK Beene. Carbon dioxide washout characteristics of the advanced crew escape suit utilizing a conformal helmet. Unpublished paper, JSC, NASA Dec. 01, 1992.

Waligora, JM, and JH Gilbert. CO2 washout test of the launch and entry Suit. Unpublished paper, JSC, NASA, June 5, 1992.

NASA Doc. #48019, Shuttle entry key cards, p. 4-5, as per Tom Hanson, DT36/BAR, Space Flight Training Division.

Appendix A
Data Collection Sheet for CO2 Helmet Study Summer 1996

Name _____ Date _____
Age _____ HT _____ in _____ cm Wt _____ lbs _____ KG

G-Suit setting _____ psi Resting HR _____ bpm
6 Min seated rest Visor Down

Seated HR _____ Initial Tre _____, Tback _____, Tarm _____, Tthigh _____,
T calf _____
CO2 : min 1 _____, min 2 _____, min 3 _____ min 4 _____,
min 5 _____, min 6 _____ min 7 _____, min 8 _____,
min 9 _____, Final _____ Final HR _____

Subject's Comments _____
_____ I

Investigator's Comments _____

***Recovery Visor-up under some test conditions, immediate walk
for others***

Walk 3.5 mph 0% grade Visor Down, G-suit inflated _____ psi

Standing HR _____ Initial Tre _____, Tback _____, Tarm _____, Tthigh _____,
T calf _____
CO2 : min 1 _____, min 2 _____, min 3 _____ min 4 _____,
Final _____ Final HR _____ Ve Rate _____ b/min

Subject's Comments _____

Investigator's Comments _____

REST PERIOD- with cooling and visor up

Time begin _____

Seated HR _____ Initial Tre _____, Tback _____, Tarm _____, Tthigh _____,
T calf _____ Final seated HR _____

Time end _____ elapsed time _____ min

Subject's Comments _____

Investigator's Comments _____

Name _____ Date _____

Walk 3.5 mph 0% grade Visor Down With Aerosport pneumotach and nose clip, G-suit inflated ____ psi

Standing HR ____ Initial Tre ____, Tback ____, Tarm ____, Tthigh ____,
T calf _____
CO2 : min 1 ____, min 2____, min 3____ min 4 _____,
CO2 Final _____ Final HR _____ Ve Rate _____ b/min

Subject's Comments _____

Investigator's Comments _____

REST PERIOD- with Cooling and visor up

Time begin _____

Seated HR ____ Initial Tre ____, Tback ____, Tarm ____, Tthigh ____,
T calf _____ Final HR _____

Time end _____ elapsed time _____ min

Subject's Comments _____

Investigator's Comments _____

VO2 measured walk Visor UP, G-suit inflated ____ psi

Standing HR ____ Initial Tre ____, Tback ____, Tarm ____, Tthigh ____,
T calf _____ VO2 Initial (stand)____, min 1 ____, min 2____,
min 3____, min 4 _____, Final _____ Final HR _____ Ve Rate
_____ b/min

Subject's Comments _____

Investigator's Comments _____

LES/ACES Non-Conformal Helmet CO2 Concentrations
Questionnaire

Name _____ Date _____

- 1) Did you have any feeling of breathlessness during any phase of testing? Which?
- 2) Did you feel any phase of the testing was particularly demanding? Which?
- 3) Did you have any feelings of anxiety, headache, drowsiness, nausea or any other unusual feelings during any phase of testing? What? Which?
- 4) Did you find any phase of testing physically demanding? Which? What body part?
- 5) Do you have any additional comments regarding this testing?
- 6) Other

35-72
038286
10A
294260

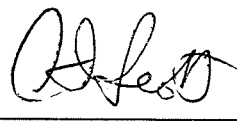
ANALYSIS OF FLOW FROM ARC-JET SPECTRA

H.E. Blackwell
Texas Southern University
ES3
August 2, 1996

Carl D. Scott
Thermal Branch
Structures and Mechanics Division
Engineering Directorate



H.E. Blackwell



Carl D. Scott

ANALYSIS OF FLOW FROM ARC-JET SPECTRA

Final Report

NASA/ASEE Summer Faculty Fellowship Program - 1996
Johnson Space Center

Prepared By: H.E. Blackwell, Ph.D.

University & Department: Texas Southern University
Physics
Houston, TX 77045

NASA/JSC

Directorate: Engineering

Division: Structures & Mechanics

Branch: Thermal

JSC Colleague: Carl D. Scott

Date Submitted: August 7, 1996

Contract Number: NAG 9-867

ABSTRACT

Materials testing is carried out at the JSC Atmospheric Reentry Materials and Structures Facility. A flow diagnostics program is under development to characterize the energy distribution in arc-jet flows used to simulate atmospheric entry. Heat transfer to materials depends on flow properties which includes the composition of and energy distribution among the atoms, ions, molecules, and molecular ions which make up the flow.

This project involves analysis of shock layer characteristics from the radiation emitted and experimentally collected from near the front of the shock to near the surface of the material. The analysis has yielded information on relative populations of neutral molecules and molecular ions within the layer. In determining non-equilibrium temperatures within the layer, some insight into the spectral constants used to compute radiative emission has been gained.

NOMENCLATURE

$A^3\Sigma_u^+$ = electronic state of molecular nitrogen
 $A^2\Pi_u$ = electronic state of molecular nitrogen ion
 $B^2\Sigma_u^+$ = electronic state of molecular nitrogen ion
 $B'^3\Sigma_g^-$ = electronic state of molecular nitrogen
 $B^3\Pi_g$ = electronic state of molecular nitrogen
 $X^1\Sigma_g^+$ = electronic ground state of nitrogen
 $X^2\Sigma_g^+$ = electronic ground state of nitrogen ion
 T_e = electron temperature
 T_r = rotational temperature
 T_v = vibrational temperature

INTRODUCTION

It is now generally agreed that additional experimental shock front and shock layer measurements are necessary in order to clarify issues such as rotational coupling and provide additional data on rates at high temperature for a number of processes. The flow diagnostics program under development at JSC will characterize the energy distribution in arc-jet flows which are used to simulate atmospheric entry. In this work we pay particular attention to those flow properties which include the composition of and energy distribution among the atoms, ions, molecules, and molecular ions which make up the flow.

ANALYSIS

Shocks in pure nitrogen have been analyzed because the spectral regions used for analysis are cleaner, i.e., they contain less undesired radiation which increases the complexity to analysis. The electronic states and the systems which place radiation within the wavelength range covered, 3000 Å to 8500 Å, is shown in Figure 1. The principal radiation from the nitrogen molecule and the molecular ion is generally grouped into regions which represent transitions between upper, v' , and lower, v'' , vibrational states which differ by the same number, i.e., $v' - v'' = \Delta v = 0, 1, 2$, etc. In the spectrum between 200 nm and 500 nm the bands of primary interest are $N_2^+(1-)$, $\Delta v = -2, -1, 0, 1, \text{ and } 2$, resulting from electronic molecular state transitions $B^2\Sigma_u^+ \rightarrow X^2\Sigma_g^+$. Above 500 nm the bands of primary interest come from N_2 , $B^3\Pi_g \rightarrow ^3\Sigma_u^+$, called the first positive system.

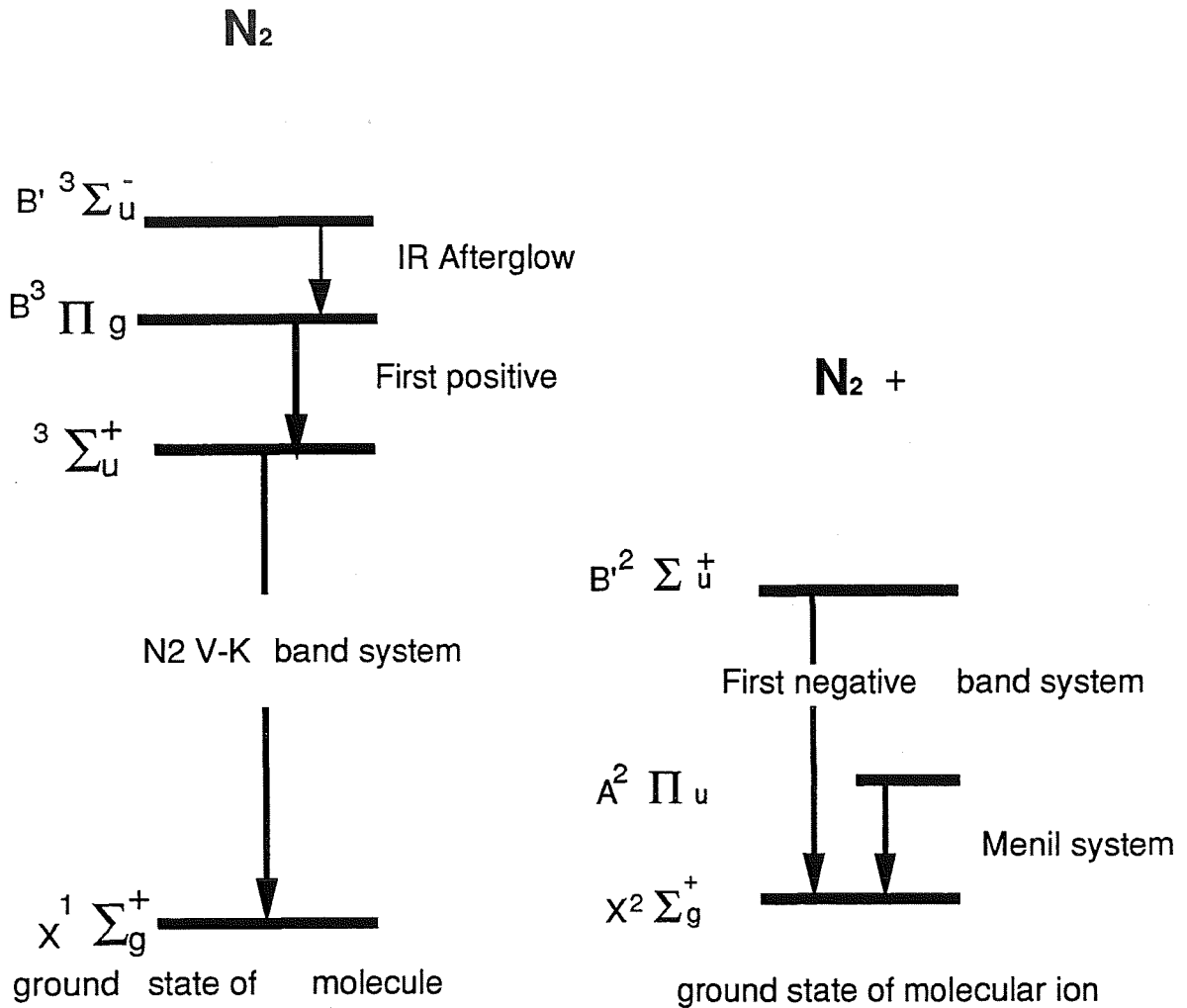


Figure 1. N_2 and N_2^+ energy states and band systems.

Measurements were obtained using a constricted arc heater in the arc jet facility at the NASA Johnson Space Center. The arc, powered by a direct current power supply, heats the gas to high enthalpy. The hot gas flows through a small settling chamber, then through a converging-diverging conical nozzle with an exit diameter of 38.1 cm, and into the chamber which contains the shock-forming test article. Radiation from the shock layer was focused on the entrance slit of a spectrometer using a 0.5 m focal length lens fixed at a perpendicular distance of 0.5 m from the nozzle axis of symmetry. The spectra were measured with a SPEX Triplemate 0.6 m spectrometer having a 1024-element linear diode array detector and were recorded using an optical multichannel analyzer (OMA) system.

A typical spectrum from the shock layer collected from near the front of the shock is shown in Figure 2.

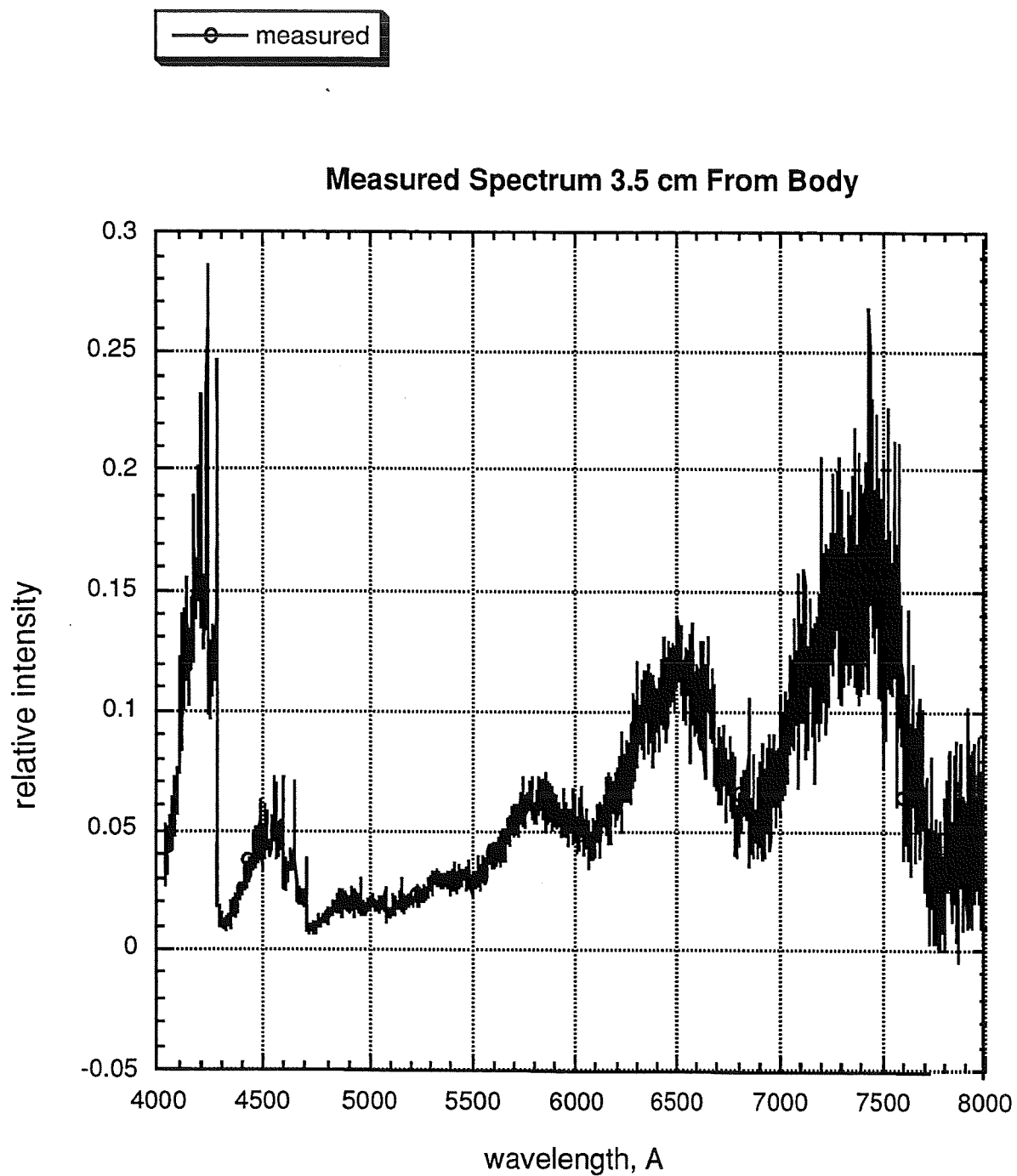


Figure 2. Spectrum obtained experimentally 3.50 cm from the test body.

In the present analysis computed spectra for N_2^+ and N_2 were necessary, as the experimental spectra were obtained from shocks in a nitrogen arc-jet flow. Temperatures within the radiating shock layer may range from 2000 to 10000 K, and may differ for the different species. Also, the energy goes into different modes, translational, electronic, vibrational, and rotational. An earlier technique for determining temperature utilized a Non-Equilibrium Air Radiation code

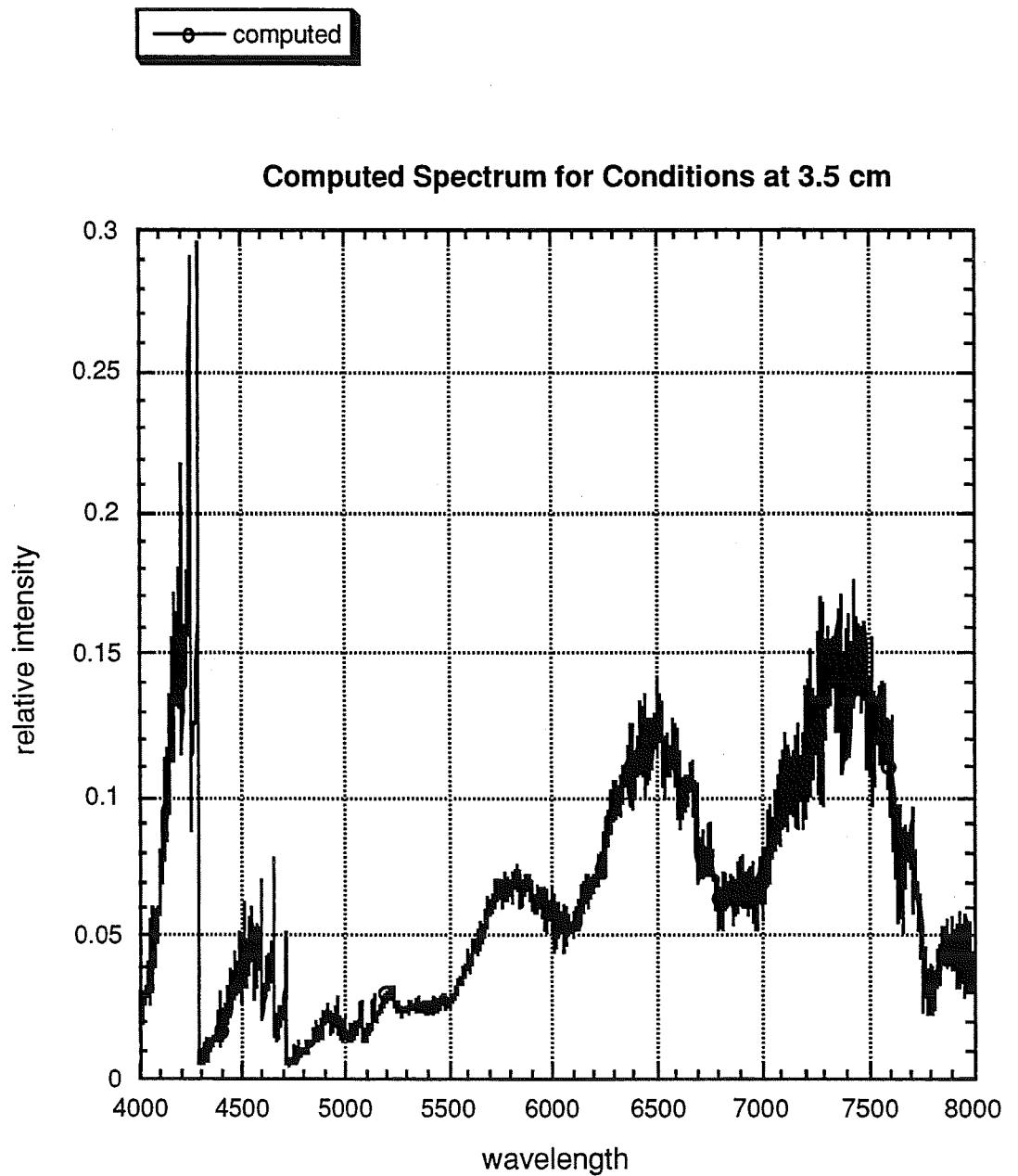


Figure 3. Spectrum computed using PSI code.

(NEQAIR) to determine the rotational temperature of the molecular nitrogen ion. The measurement was made using NEQAIR to attempt a match of the spectra or find appropriate rotational line emission ratios for N_2^+ , $\Delta v = -1$, the band at 4280 Å.

All species are generally assumed to have the same rotational temperature. The temperature obtained was then input to a spectral fitting code by Physical Sciences, Inc. for simulation of the measured spectra in other wavelength regions in order to obtain a vibrational temperature.

This study uses the PSI code alone to estimate both rotational and vibrational temperatures. Using that code the spectrum shown in Figure 3 could be obtained.

RESULTS

This work concentrated more on the long wavelength region of the spectrum, between 5000 Å and 8000 Å. While radiation from the neutral molecule, 1st positive system, dominates the radiation near the front of the shock, radiation from the A state of the molecular ion, the Menil system, is present. Vibrational temperature for the two systems were found to differ.

Radiation from the ion begins to dominate as one moves into the layer toward the body. At the closest observation point to the body, radiation from the neutral atom becomes strong indicating that N_2 populations have decreased due to dissociation. We will soon prepare a paper discussing these results.

Study of populations led to a measurement, for the first time, of the electronic excitation temperature. This temperature appears to differ from both rotation and vibration for the non-equilibrium layer. This matter also, with some additional work, will be published.

A review of the total spectrum, the range shown in Figure 2, has uncovered a number of problems associated with the analysis and determination of rotational and vibrational temperatures. The radiation from higher lying states must be incorporated in the calculated spectra for better fit with measurement.

Accuracy of the work depends on the accuracy of constants used in the simulation of the spectra. We have made some progress in this area, uncovering some fundamental relations, which should merit an early publication in order to assist other analysts with their work.

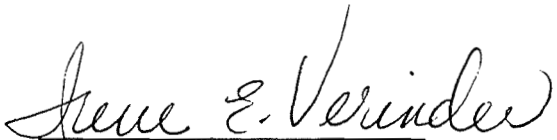
56-24
038287

DESIGN CRITERIA FOR X-CRV HONEYCOMB PANELS - 20A
A PRELIMINARY STUDY

Vincent Caccese
University of Maine
ES5
August 2, 1996

Irene Verinder
Mechanical Design and Analysis Branch
Structures and Mechanics Division
Engineering Directorate


Vincent Caccese


Irene Verinder

DESIGN CRITERIA FOR X-CRV HONEYCOMB PANELS -
A PRELIMINARY STUDY

Final Report
NASA/ASEE Summer Faculty Fellowship Program-1996
Johnson Space Center

Prepared by:	Vincent Caccese
Academic Rank:	Associate Professor
University and Department:	University of Maine Dept. of Mechanical Engineering
NASA/JSC Directorate:	Engineering
Division:	Structures and Mechanics
Branch:	Mechanical Design and Analysis
JSC Colleague:	Irene Verinder
Date Submitted:	August 2, 1996
Contract Number:	NAG 9-867

ABSTRACT

The objective of this project is to perform the first step in developing structural design criteria for composite sandwich panels that are to be used in the aeroshell of the crew return vehicle (X-CRV). The preliminary concept includes a simplified method for assessing the allowable strength in the laminate material. Ultimately, it is intended that the design criteria be extended to address the global response of the vehicle. This task will require execution of a test program as outlined in the recommendation section of this report.

The aeroshell of the X-CRV is comprised of composite sandwich panels consisting of fiberite face sheets and a phenolic honeycomb core. The function of the crew return vehicle is to enable the safe return of injured or ill crewpersons from space station, the evacuation of crew in case of emergency or the return of crew if an orbiter is not available. A significant objective of the X-CRV project is to demonstrate that this vehicle can be designed, built and operated at lower cost and at a significantly faster development time. Development time can be reduced by driving out issues in both structural design and manufacturing concurrently. This means that structural design and analysis progresses in conjunction with manufacturing and testing.

Preliminary tests results on laminate coupons are presented in the report. Based on these results a method for detection material failure in the material is presented. In the long term, extrapolation of coupon data to large scale structures may be inadequate. Test coupons used to develop failure criteria at the material scale are typically small when compared to the overall structure. Their inherent small size indicates that the material failure criteria can be used to predict localized failure of the structure, however, it can not be used to predict failure for all failure modes. Some failure modes occur only when the structure or one of its sub-components are studied as a whole. Conversely, localized failure may not indicate failure of the structure as a whole and the amount of reserve capacity, if any, should be assessed.

To develop a complete design criteria experimental studies of the sandwich panel are needed. Only then can a conservative and accurate design criteria be developed. This criteria should include effects of flaws and defects, and environmental factors such as temperature and moisture. Preliminary results presented in this report suggest that a simplified analysis can be used to predict the strength of a laminate. Testing for environmental effects have yet to be included in this work. The so called "rogue flaw test" appears to be a promising method for assessing the effect of a defect in a laminate. This method fits in quite well with the philosophy of achieving a damage tolerant design.

1.0 INTRODUCTION

The aeroshell of the crew return vehicle (X-CRV) vehicle is comprised of composite sandwich panels consisting of fiberite face sheets and a phenolic honeycomb core. A first step in developing structural design criteria for these sandwich panels is the primary focus of this report. It includes a simplified method for assessing the allowable strength in the laminate material. Ultimately it is intended that the design criteria be extended to address the global response of the vehicle. This task will require execution of a test program as outlined in the recommendation section of this report.

The function of the crew return vehicle is to enable the safe return of injured or ill crewpersons from space station, the evacuation of crew in case of emergency or the return of crew if an orbiter is not available. The shape of the X-CRV is based upon the USAF/Martin X-24A lifting body vehicle. A significant objective of the X-CRV project is to demonstrate that this vehicle can be designed, built and operated at lower cost and at a significantly faster development time.

Substantial cost and weight savings can be achieved in aerospace vehicles through the use of composite materials. For example, the NASA/DoD advanced composites technologies program has a projected goal of 30%-50% weight reduction and a 20%-25% cost savings when compared to a baseline aluminum wing and fuselage structure of a commercial vehicle in production (Smith et. al, 1995). The predicted savings are to be achieved by a synergism of innovative design and manufacturing techniques. Similar efficiencies are also anticipated for an aerospace vehicle such as the X-CRV. To this end, the experimental version of the crew return vehicle, the X-CRV, uses a composite sandwich as the structural element for the outer mold line (OML). One of the primary advantages in construction of this type over aluminum structures is that the part size can be relatively large. The cost savings accrue due to a reduction of labor required to fabricate and assemble these parts. Development time can be reduced by driving out issues in both structural design and manufacturing concurrently. Furthermore, structural design and analysis progresses in conjunction with manufacturing and testing.

1.1 Development of Design Criteria

The focus of this report is to summarize a preliminary assessment of a simple and operational criteria that can be used in the structural design of the X-CRV composite outer aeroshell. A structural design criteria can first be developed based upon classical mechanics failure criteria. These criteria are used to predict failure of the material locally. Preventing material failure is a first step in assuring the structural integrity.

Test coupons used to develop failure criteria at the material scale are typically small when compared to the overall structure. This is especially true in a vehicle such as the X-CRV. When these test coupons are fabricated they are effectively cut away from a larger sample of the base material. Their inherent small size indicates that the material failure criteria can be used to predict localized failure of the structure, however, it can not be used to predict failure for all failure modes. Some failure modes occur only when the structure or one of its subcomponents are studied as a whole. These failure modes and are not predicted by coupons tests. Conversely, localized failure may not indicate failure of the structure as a whole and the amount of reserve capacity, if any, should be assessed.

In the long term, extrapolation of coupon data to large scale structures may be inadequate. Experimental verification of the failure criteria using components representative of the

global structural response is imperative. Testing of two-way panels is recommended for use in the verification process. The validity and conservativeness of the design criteria can then be assessed with confidence and results of panel tests can be correlated to finite element models of the structure.

In the end, the design criteria employed should be one that is reasonably accurate and operationally simple. In choosing this criteria a realistic look at the design process is required. Ideally, a more complicated engineering solution is typically thought of as being more accurate. In an ideal situation the more complicated solution may be the engineers choice because intuition tells us that it will yield a more optimum design at the expense of some design time. Realistically, however, designs are subject to change caused by updates to the desired service, cost concerns, and to correct for errors. Feeding this information back into a more complicated analytical model may not be desirable. It will increase the likelihood of errors and delay the design. Therefore, the choice of a reasonably accurate, conservative, simpler criteria is better, especially for preliminary design.

1.2 Failure Criteria

The rationale behind mechanics failure criteria is that data from relatively simple tests can be used to predict the failure of a material as it is subjected to more complex states of stress and strain. Failure criteria are based largely upon observation of test data and can be thought of as operational rather than mechanistic. Failure criteria are empirical expressions that are related to the material failure process.

In polymer composites, better correlation between predictions and experiments have been observed when failure criteria is applied to the laminate rather than on a ply-by-ply basis (Norr et. al , 1983). In other words, a more accurate evaluation of the structural response will be determined from tests and analysis performed at the macroscopic scale. The ultimate strength of a laminate can be predicted using the relevant strength data for a single ply. This, however, is a relatively complex problem. It is more appropriate to rely upon test data for laminate strength values. The basic material tests for the laminate consists of standard coupon tests that are typically used to quantify material properties. These test are done on a routine basis and data from these tests are input into the failure model. The same holds true for evaluation of a composite sandwich and it will be more accurate to evaluate this sandwich material at a scale large enough to represent the behavior of the structural component.

There are numerous material failure criteria that have been developed in the past. Rowlands (1985) gives a comprehensive summary of a multitude of criteria. Two of the criteria used frequently in the analysis of composite materials, the maximum strain criteria (St. Venant) and the Tsai-Wu criteria, will be emphasized in this report.

For the most part, failure criteria all agree in failure prediction when the material is subjected to simple states of stress such as uniaxial tension, uniaxial compression or pure shear. They differ when the effects of combined loading are to be predicted. Furthermore, failure criteria are to be used with caution because they will not predict all failure modes, especially those that occur at the sub-component or component scale.

1.2.1 Tsai-Wu failure criteria - The Tsai-Wu failure criteria for orthotropic lamina can be written as follows:

$$F_1\sigma_x + F_2\sigma_y + F_{11}\sigma_x^2 + 2F_{12}\sigma_x\sigma_y + F_{22}\sigma_y^2 + F_{66}\sigma_s^2 = FI$$

where

FI= the failure index

$$F_1 = \frac{1}{X_t} - \frac{1}{X_c}, \quad F_2 = \frac{1}{Y_t} - \frac{1}{Y_c}, \quad F_{11} = \frac{1}{X_t X_c}$$

$$F_{22} = \frac{1}{Y_t Y_c}, \quad F_{66} = \frac{1}{S^2}, \quad F_{12} = -\frac{1}{2} \sqrt{F_{11} F_{22}}$$

X_t = tensile strength in X - material direction

Y_t = tensile strength in Y - material direction

X_c = compressive strength in X - material direction

Y_c = compressive strength in Y - material direction

S = shear strength referenced to the X - Y plane

This criteria uses linear and quadratic stress terms. The non-linearity of this criteria indicates that the failure index will not be directly proportionally to the applied loads.

1.2.2 Maximum Strain Failure Criteria- Using this theory failure is predicted when the applied strain in a principal material direction exceeds the maximum allowable principal strain in that direction. Mathematically speaking, failure occurs when any of the following inequalities are violated.

$$\varepsilon_x^+ < \varepsilon_{xt}, \quad \varepsilon_x^- > -\varepsilon_{xc}, \quad \varepsilon_y^+ < \varepsilon_{yt}, \quad \varepsilon_y^- > -\varepsilon_{yc}, \quad |\gamma_{xy}| < \gamma_{xy}$$

where

$\varepsilon_{xt}, \varepsilon_{xc}, \varepsilon_{yt}, \varepsilon_{yc}, \gamma_{xy}$ are the ultimate strains,

t indicates tension and c compression

$\varepsilon_x^+, \varepsilon_x^-, \varepsilon_y^+, \varepsilon_y^-$ are the applied strains

In this case the resulting strains are directly proportional to the applied loads. A margin of safety can be determined by direct scaling.

1.2.3 Ply-by-Ply Analysis- In design of composites strain compatibility is assumed between adjacent elements of the composites. In other words, the strain between two adjacent infinitesimal coupons of materials is the same. A composite in bending will have a linear strain distribution through the thickness. However, the state of stress between two adjacent elements is not the same when the two elements have different compliance's. The stress state will be discontinuous through the thickness. This makes a ply-by-ply stress analysis of a composite laminate operationally tedious.

1.3 Damage Tolerant Criteria

In developing values for allowable material behavior a damage tolerant design is desired where a component will maintain its structural integrity while a given defect is present. Damage tolerant design relies on accepting that damage will occur, on implementing a system to detect damage, and on a design where adequate strength is maintained in the damaged structure. Damage tolerance in composites is complex primarily due to the non-homogeneous nature of the material. Behavior of most carbon fiber reinforced composites is nearly linear up to failure and the failures are sudden. In manufacturing of composites a larger number of defects may exist when compared to metallic structures.

Influence of an allowable defect can be incorporated into the design process. Defects in composites can occur due to manufacturing preparation and production, machining, processing and of the assembly of the component. Some of these defects include voids, delaminations, disbonds, foreign object inclusions, resin starved or rich areas, incomplete resin cure, misaligned fiber orientation, fiber gaps, wrinkled layers, and poor surface conditions. In sandwich panels additional defects may include poor core splice, disbonds from facesheets, crushed core and core gaps. Assembly defects may result from scratches gouges, incorrect drilling of holes and tool impact damage. The decision to repair or reject the component will be based upon the size and nature of the defect and its influence on the structural performance. Accurate methods of evaluating the effect of the defect on the structure and detection of the defect in the first place are required.

Undesirable structural response due to accumulation of damage under hysteresis loading, impact and fatigue should be mitigated. Damage due to impact depends upon the energy level of the impact. High energy impacts will typically produce visible damage and procedures can be set in action to mitigate the effects of this type of damage on the structure. Low energy impact damage can be detrimental to the long-term life of the structure and this damage is often difficult to detect. In composites damage is expected to occur at quite low impact energy levels. This is especially true for sandwich panels. Thickening of the facesheets will help to lessen damage. Impact from an object such as a toolbox dropped from 1 foot may produce significant damage in the composite structure.

Tension fatigue is not normally a problem in composites. Tests have shown that for specimens with holes tension fatigue life is not a major concern. Specimens loaded to 90% of their ultimate tensile strength have achieved fatigue life of over 1 million cycles (Hoskin and Baker, 1986). On the other hand, compression specimens have shown a reduced fatigue life similar to that of metals. One million cycles was not achieved unless the compressive stress was limited to less than 40 percent of the ultimate strength.

Damage tolerant design takes into account the type and size of defect that may be present in the structure. Once the size and nature of the allowable defect is established, its effect on the structure can be accounted for in the design process. Figure 1 shows the effect of such a hole on the failure strength. In this case a 0.25 inch hole will reduce the failure strength to 60% of its unflawed value. A crack of a 0.25 inch length will have a similar effect on the tensile strength of the material.

One method for reducing the design allowables in composites design is the rogue flaw test. In this test a 1/4 inch diameter hole (flaw) is incorporated into a 1 inch wide tensile specimen. In doing so, stress concentrations will occur around the flaw and the ultimate strength and strain will be reduced by a substantial amount. This results in allowables that can be used at the material scale. Other damage tolerant criteria can be developed following a similar philosophy.

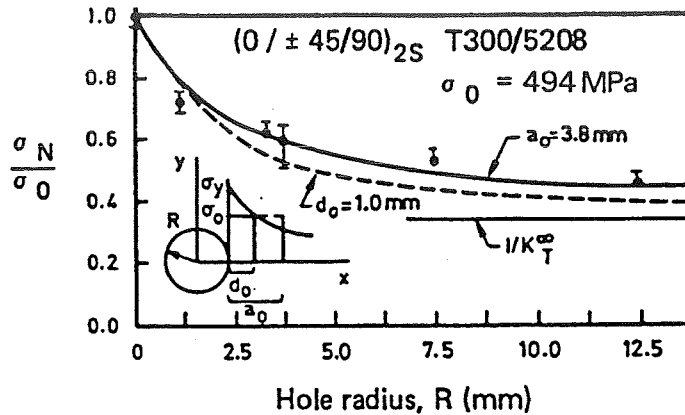


Figure 1 - Effect of Hole on Tensile Strength of a graphite/epoxy Laminate, predicted and experimental (from Hoskin and Baker, 1986).

1.4 Influence of Environmental Conditions

Temperature extremes and moisture, especially in combination can significantly influence the structural properties of a composite. These effects must be considered in design. Tests should be conducted on representative samples to assess the environmental influence. Moisture is absorbed and desorbed in composites by a diffusion process. This process is relatively slow and is highly temperature dependent. Moisture can reduce the glass transition temperature and in combination with high temperature it can reduce strength. The cyanate resin, for example, undergoes a modulus decrease of 23% and a flexural strength decrease of 30% at 325° F/wet conditions when compared to dry room temperature conditions. Compressive properties of fiber dominated laminates are typically more affected by these conditions since a modulus reduction of the resin increases the likelihood of fiber buckling at a lower stress.

2. APPROXIMATE DEFINITION OF ALLOWABLE STRENGTH

The purpose of this section is to describe the theoretical considerations in development of allowable strength values for the Fiberite/Phenolic Honeycomb sandwich panels. The sandwich panels are made from two primary constituents, namely, the face sheets made of Fiberite 3454-2AJ tape and the honeycomb core made of Hexel Flexcore HRP/F35-4.5 phenolic core. For purposes of this report an example configuration consisting of 1.5 inch thick Flexcore and face sheets with 14 layers [45,-45,90,0,90,0,90]s will be discussed in regard to defining the allowable strength.

2.1 Constituent Materials

The fiberite ply consists of a fiber that is graphite based and a Cyanate Resin 954-2A. For analysis purposes these constituent materials were assumed to be isotropic and their baseline properties are given in Table 1.

A theoretical ply material was constructed using the graphite fiber and cyanate resin properties listed above. The ply calculation facility of the IDEAS program was used for this purpose. In these computations the parameters were chosen as summarized in Table 2.

TABLE 1A- PROPERTIES OF FIBER AND RESIN MATERIALS

	Graphite Fiber	Cyanate Resin
Longitudinal Modulus, E_x , (psi)	78×10^6	44×10^6
Poisson's Ratio, ν_{xy}	0.25	0.38
Shear Modulus, G_{xy} , (psi)	31.2×10^6	15.9×10^6
Ultimate Tensile Strength, (psi)	583×10^3	10.0×10^3
Ultimate Tensile Strain, μstrain	7455*	25,900
Specific Gravity	1.91	1.24

* Approximate based on ideally brittle behavior.

TABLE 1B- PROPERTIES OF CORE MATERIAL

	Flexcore
Compressive Modulus, (psi)	49×10^3
Minimum Stabilized Compressive Strength (psi)	470
Shear Modulus, X direction (psi)	22×10^3
Shear Modulus, Y direction (psi)	12×10^3
Minimum Shear Strength, X direction (psi)	220
Minimum Shear Strength, Y direction (psi)	110
Specific Gravity	0.0721

TABLE 2 - INPUT FOR IDEAS PLY PROPERTIES CALCULATION

Matrix	Cyanate
Fiber	Graphite
matrix vol. fraction, V_m	0.44
fiber vol. fraction, V_f	0.56
reinforcing factors	no
theory for elastic constants	Mechanics of Materials
theory for thermal properties	Levin

2.2 Fiberite Ply Properties

Calculated ply properties were determined using the ply definition module of the IDEAS computer code. These properties can be compared to material data given by Fiberite. The ply properties for a unidirectional fiberite sheet are summarized in Table 3. The last column of this table gives nominal values that will be used in a demonstration model presented in Section 2.3. The nominal strain values assume elastic-brittle behavior and are computed by taking the nominal measured failure strength divided by the elastic modulus.

TABLE 3 - SUMMARY OF FIBERITE PLY PROPERTIES

	Calculated IDEAS	Fiberite data sheet	Nominal
Longitudinal Modulus, E_x (psi)	43.9×10^6	45.5×10^6 (T) 42.7×10^6 (C)	$*44.1 \times 10^6$
Transverse Modulus, E_y (psi)	1.12×10^6		1.12×10^6
Poisson's Ratio, ν_{xy}	0.307		0.307
Shear Modulus, G_{xy} (psi)	0.36×10^6		0.36×10^6
Long. Tensile Strength, X_t (psi)		310.8×10^3	310.8×10^3
Long. Comp. Strength, X_c (psi)		130.4×10^3	130.4×10^3
Trans. Tensile Strength, Y_t (psi)		3.4×10^3	3.4×10^3
Trans. Comp. Strength, Y_c (psi)		1.5×10^3	1.5×10^3
Shear Strength, S (psi)		10.5×10^3	10.5×10^3
Long. ult. tensile strain, ϵ_{ux} , $\epsilon_{ustrain}$			7048
Long. ult. comp. strain, ϵ_{ux_c} , $\epsilon_{ustrain}$			2957
Trans. ult. tensile strain, ϵ_{uy} , $\epsilon_{ustrain}$			3036
Trans. ult. comp. strain, ϵ_{uy_c} , $\epsilon_{ustrain}$			1339
Ultimate shear strain, γ_u , $\gamma_{ustrain}$			29,176

* Tensile and compressive properties were averaged

2.3 Fiberite Laminate Face Sheet

An example face sheet can be constructed using the ply material summarized in Table 3 for demonstrating a simplified analysis procedure. This example is of a 14 ply laminate with a layer thickness of 0.0048 inches. The lay-up for this laminate is [45,-45,90,0,90,0,90]s. In this development the primary material axes of the laminate are designated by x and y subscripts whereas direction of applied stress and strain are designated by a 1 or 2 subscript.

Stiffness properties were calculated using the laminate definition module of the IDEAS program. Strength estimations can be made for this laminate based on the assumption that when the laminate is subjected to a unidirectional state of stress along a primary material axis, only the fibers oriented along the direction of the stress will contribute to the ultimate strength. This gives what is called the Simplified Analysis Limit. A classic failure criteria such as Tsai-Wu or Maximum Strain can be used to predict strengths under combined states of stress assuming that the laminate acts as an ideally orthotropic material.

2.3.1 Parameters for TSAI-WU Strength analysis.

In a TSAI-WU analysis five laminate strength parameters are required, namely, X_t , Y_t , X_c , Y_c , and S . These parameters can be determined using five separate tests, two tension tests, two compression tests and a shear test. Without test data they can be approximated by making the assumption stated above as the Simplified Analysis Limit.

Tensile Strength Parameters - This test can be thought of as a uniaxial tension test with the material oriented in the zero or ninety degree direction. In the longitudinal, 0, direction there are a total of 4 plies and there are a total of 6 plies at 90. The stress at failure is calculated as:

$$X_t = (4/14) * 310.8 \times 10^3 = 88.8 \times 10^3 \text{ psi}$$

$$Y_t = (6/14) * 310.8 \times 10^3 = 133.2 \times 10^3 \text{ psi}$$

Compressive strength - This test can be thought of as a compression test, global buckling prevented, with the material oriented in the zero or ninety degree direction. The stress at failure is calculated as:

$$X_c = (4/14) * 130.4 \times 10^3 = 37.2 \times 10^3 \text{ psi}$$

$$Y_c = (6/14) * 130.4 \times 10^3 = 55.8 \times 10^3 \text{ psi}$$

Shear strength - The shear strength can be thought of as applying a state of pure shear, $\tau_{xy} = \sigma$, on an element that does not buckle. In pure shear a rotation of 45 degrees will yield a state of stress that can be defined as follows:

$$\sigma_1 = \sigma \quad \sigma_2 = -\sigma \quad \tau_{12} = 0$$

For this laminate σ_1 will be oriented along the +45 degree axis of the laminate and will be in tension. The stress σ_2 will be oriented along the -45 degree axis of the laminate and will be in compression. The controlling factor will be the compressive strength of the -45 degree plies. There are two plies to resist this stress. Accordingly, the shear strength can be approximated as:

$$S = (2/14) * 130.4 \times 10^3 = 18.6 \times 10^3 \text{ psi}$$

The tensile, compressive and shear strengths listed above can be used in the Tsai-Wu expression across the laminate. When this is done the coefficients in the Tsai-Wu expression become.

$$F_1 = -1.56 \times 10^{-5}, \quad F_2 = -1.04 \times 10^{-5}, \quad F_{11} = 3.03 \times 10^{-10}, \\ F_{22} = 1.35 \times 10^{-10}, \quad F_{12} = -1.0 \times 10^{-10}, \quad F_{66} = 2.88 \times 10^{-9}$$

Tensile and Compressive Tests at 45 degrees

Once these parameters are chosen other states of stress can be analyzed to assess the validity of this hypothesis. For starters, a theoretical uniaxial tensile test at an axis of +45 degrees can be applied to the laminate. This results in a state of stress along the primary material axes as follows:

$$\sigma_x = 0.5 * \sigma \quad \sigma_y = 0.5 * \sigma \quad \tau_{xy} = -0.5 * \sigma$$

The stress, σ , that brings the Failure Index to 1.0 will be $\sigma = 45.2 \times 10^3$ psi

Failure can also be predicted using the same criteria as done in the calculation of the tension strength parameter. Failure occurs when the plies along the tension direction fail. Since there are two +45 degree plies the tensile strength is predicted as:

$$S_{45t} = (2/14) * 310.8 \times 10^3 = 44.4 \times 10^3 \text{ psi}$$

For practical purposes these two values are nearly the same.

Unfortunately, the same does not hold true for a compression test at 45 degrees. In this case the compressive strength is predicted as:

$$S_{45c} = (2/14) * 130.4 \times 10^3 = -18.6 \times 10^3 \text{ psi}$$

The compressive stress, σ , that brings the Failure Index to 1.0 is $\sigma = -28.5 \times 10^3$ psi

2.3.2 Parameters for Maximum Strain Analysis

Parameters for use in the maximum strain analysis will be developed based upon properties of the laminate. The effective modulus of the laminate calculated based upon classical lamination theory are as follows:

$$E_x = 15.8 \times 10^6 \\ E_y = 21.7 \times 10^6 \\ G_{xy} = 3.42 \times 10^6$$

The maximum strain can be computed based upon the stress at failure determined by the Simplified Limit Analysis. This analysis will achieve the same stress level at failure during simple tension, compression and shear loading. For the demonstration laminate the strain parameters are as follows:

$$\epsilon_{u_{xt}} = \frac{88.8 \times 10^3}{15.8 \times 10^6} = 5620 \mu\epsilon, \quad \epsilon_{u_{yt}} = \frac{133.2 \times 10^3}{21.7 \times 10^6} = 6138 \mu\epsilon, \quad \epsilon_{u_{xc}} = \frac{37.2 \times 10^3}{15.8 \times 10^6} = 2354 \mu\epsilon,$$

$$\epsilon_{u_{yc}} = \frac{55.8 \times 10^3}{21.7 \times 10^6} = 2571 \mu\epsilon, \quad \gamma_{u_{xy}} = \frac{18.6 \times 10^3}{3.42 \times 10^6} = 5444 \mu\epsilon$$

Table 4 provides a summary of properties for the [45,-45,90,0,90,0,90]s laminate.

TABLE 4 - SUMMARY OF THE LAMINATE PROPERTIES

Laminate	[45,-45,90,0,90,0,90]s	Long. Tensile Strength, X _t (psi)	44.4 x 10 ³
Long. Modulus, E _x (psi)	15.8 x 10 ⁶	Long. Comp. Strength, X _c (psi)	18.6 x 10 ³
Trans. Modulus, E _y (psi)	21.7 x 10 ⁶	Trans. Tensile Strength, Y _t (psi)	66.6 x 10 ³
Poisson's Ratio, V _{xy}	0.149	Trans. Comp. Strength, Y _c (psi)	27.9 x 10 ³
Poisson's Ratio, V _{yz}	0.149	Shear Strength, S (psi)	18.6 x 10 ³
Poisson's Ratio, V _{zx}	0.149	Long. ult. tensile strain, e _{ux} , _{ustrain}	5620
Shear Modulus, G _{xy} (psi)	3.42 x 10 ⁶	Long. ult. comp. strain, e _{ux} , _{ustrain}	2354
Shear Modulus, G _{yz} (psi)	0.342 x 10 ⁶	Trans. ult. tensile strain, e _{uy} , _{ustrain}	6138
Shear Modulus, G _{zx} (psi)	0.347 x 10 ⁶	Trans. ult. comp. strain, e _{uy} , _{ustrain}	2571
Laminate Thickness, in.	0.0672	Ultimate shear strain, γ_u , _{ustrain}	5444

3. TENSION TESTS OF FIBERITE LAMINATES.

The validity of the simplified approach needs to be verified by testing. This section presents a preliminary testing program which can be thought of as a first step in the validation process. More tests are required. In this phase tests were conducted on two different lay-ups of laminates similar to what would be a facesheet in a honeycomb panel. These facesheets were made of the Fiberite 3454-2AJ tape and the lay-ups were as follows:

8 Ply - [0,90,45,-45]s and 16 Ply - [90,0,0,90,0,60,-60,0]s

Stiffness properties of these laminates can be computed theoretically as given in Table 5.

TABLE 5 - MODULUS AND POISSON'S RATIO, 8-PLY AND 16-PLY LAMINATES.

	8 - Ply	16 - Ply
Longitudinal Modulus, E _x (psi)	15.2 x 10 ⁶	22.8 x 10 ⁶
Transverse Modulus, E _y (psi)	15.2 x 10 ⁶	17.6 x 10 ⁶
Effective Modulus at 45 Degrees, (psi)	15.2 x 10 ⁶	7.9 x 10 ⁶
Poissons Ratio, V _{xy}	0.33	0.13
Shear Modulus, G _{xy} (psi)	5.72 x 10 ⁶	2.37 x 10 ⁶

Strength and strain parameters can be calculated using lamination theory and the simplified method presented in Section 2. These values are presented in Table 6.

TABLE 6 - STRENGTH AND MAXIMUM STRAIN PARAMETERS.

	8 Ply	16 Ply
	Simplified Theory	Simplified Theory
Long. Tensile Strength, X_t (psi)	77.7×10^3 107.3×10^3	155.4×10^3 160.9×10^3
Long. Comp. Strength, X_c (psi)	32.6×10^3	65.2×10^3
Trans. Tensile Strength, Y_t (psi)	77.7×10^3 107.3×10^3	77.7×10^3 122.7×10^3
Trans. Comp. Strength, Y_c (psi)	32.6×10^3	35.6×10^3
Shear Strength, S (psi)	32.6×10^3	15.2×10^3
Long. ult. tensile strain, ϵ_{ux} , μ strain	5112	6815
Long. ult. comp. strain, ϵ_{xc} , μ strain	2145	2857
Trans. ult. tensile strain, ϵ_{yt} , μ strain	5112	4415
Trans. ult. comp. strain, ϵ_{yc} , μ strain	2145	2023
Ultimate shear strain, γ_u , μ strain	5699	6414

Tensile test specimens were cut from a 12" by 12" sheet of the laminate material. The specimens were 8" in length and 0.5" in width. Three sets of five were cut from each sheet for a total of thirty samples. The first set was cut in the direction of the plies in the outer layer. The second and third sets were cut at 90 degrees and 45 degrees to this direction. Specimens were designated as follows:

$$*P-@@-0\#$$

where * represents the number of plies (8 or 16), @ represents the angle of cut relative to the direction of the top ply layer, and # represents the specimen number in the set. For example, specimen 16P-90-03 is a 16 ply specimen cut at 90 degrees to the top ply (this is the laminate's strong or X-direction) and is the third specimen in the series. Holes of 1/8" diameter were drilled in the center of the fourth and fifth specimen of each set.

One of the objectives of this preliminary study was to develop some experience in testing these materials. Obviously, due to the small sample size this series of tests does not represent a statistically significant sample and the reader is cautioned to not rely too heavily on these results. The intention was to gain some initial insight into the behavior of these laminates and to develop a starting point for further study.

It was found that testing of straight specimens is more of an art than a science. The desired failure in a specimen is one where it fails in the gage area. Several gripping techniques were attempted. ASTM D3039 (1995) recommends use of an emery cloth between the grip and the specimen for straight laminates and this method was selected for these tests. The response of the specimen is sensitive to grip method grip pressure and alignment of the specimen in the machine. Use of a fixed grip tends to increase the problem of alignment, therefore, ball and socket grip connections are recommended at top and bottom.

Even with all of these precautions taken a majority of the specimens failed near to the grip area. Intuition tells us that this will most likely be the case. Failure in a specimen will initiate at a flaw or due to a stress concentration in the specimen. The likelihood is small that a flaw will be more severe than the stress concentration near the grips.

Other recommended methods for gripping are use of tabs or fabrication of tapered specimens. The tabs will help mitigate damage to the outer layers of the laminate and may help to reduce the concentration of stress at the grips. The effectiveness of the tabs can only be assessed by testing. Fabrication of tapered specimens is possible. Care should be taken to make the taper gentle enough so that stress concentrations are not excessive at the taper. This would only move the problem from one region to another. If a comprehensive laminate testing program is to be undertaken an attempt at developing a tapered specimen should be made. If this is not successful or practical it should be followed by studying the feasibility of using tabs.

In testing of simulated flawed specimens with holes the gripping problems do not exist. These test results are expected to be more consistent, and they were. Failure will virtually always occur through the flawed region.

3.1 Test Results

Results of the Fiberite laminate tests are summarized in Table 7, including the results of both the straight specimens and the specimen with holes. The computations of modulus of elasticity, E , and ultimate stress were based upon the nominal thickness. The last column of this table provides a ratio of the strength of the laminate to the strength determined by the simplified method. For the off axis specimens cut at 45 degrees (8P-45 and 16P-45) the ratio was based upon the limiting value of stress determined by the maximum strain criteria using the parameters presented in Table 6.

Referring to the predicted modulus of elasticity presented in Table 5 and the experimentally determined modulus given in Table 7 it can be seen that this parameter can be predicted with good accuracy using classic lamination theory. The average percent difference in this prediction is -0.3% for the 8-Ply laminate, -3% for 16P-0, 6% for 16P-90 and -0.2% for 16P-45.

In the 16-ply laminate tested on its strong axis (16P-90, Figure 3) one-half of the plies in this case are oriented in the strong direction. The cross plies being at 60 degrees indicates that a relatively small amount of load sharing will be contributed by these plies. Also, this causes the simplified analysis limit to be relatively close to the lamination theory limit. Difficulties were observed in achieving the strength indicated by the simplified analysis limit as none of the three tests achieved this limit. In the other direction (16P-0, Figure 4) the simplified analysis limit was achieved in two of the three tests and the lower strength in the third tests was due to problems at the grips. In this case substantial load sharing occurs by the cross plies which are located at an angle of thirty degrees. The 8-ply material (Figures 5-6) is a quasi-isotropic material and one would expect the same behavior in either direction. In this lay-up significant load sharing exists due to the 45 degree plies. Four of the six tests achieved the simplified analysis limit.

In the off-axis tests at 45 degrees (8P-45 and 16P-45) the strength can be predicted using the parameters presented in Table 6. Table 8 gives a summary of these predicted strengths using both the maximum strain and the Tsai-Wu criteria. The maximum strain criteria gives a more conservative prediction of the strength in this orientation. In the tests, the strength of 16-ply material exceeded these predictions as indicated by a ratio greater than 1 in Table 7. For the 8-ply material it may appear, at first glance, that both the maximum strain criteria and the Tsai-Wu criteria are overly conservative and that the strength should reach

the same value as in the X and Y material direction (77.7 ksi) since this material is quasi-isotropic. However, at 45 degrees this material makeup looks like a [-45,45,0,90]_s laminate and Crossman (1983) has shown that this stacking sequence is prone to delamination and generally will exhibit a substantially lower ultimate strength.

TABLE 7 - RESULTS OF THE LAMINATE TESTS.

Specimen	Nom. t	W	t	Peak Load	Ult. Stress	Ult. Strain	E	Ratio
	in.	in.	in.	lbs.	psi	ustrain	Msi	
16P-0-01	0.0768	0.5102	0.0815	3675	93,796	5500	16.7	1.21
16P-0-02	0.0768	0.5020	0.0810	3748	97,215	5500	17.3	1.25
16P-0-03	0.0768	0.5023	0.0802	2850	73,874	4600	17.0	0.95
16P-0-04	0.0768	0.5043	0.0818	2263	58,426	3600	16.1	0.75
16P-0-05	0.0768	0.5045	0.0818	2255	58,200	3700	15.5	0.75
16P-90-01	0.0768	0.5013	0.0797	4803	124,745	4800	26.0	0.80
16P-90-02	0.0768	0.5025	0.0800	5267	136,479	6000	23.3	0.88
16P-90-03	0.0768	0.5042	0.0797	5745	148,373	6400	23.2	0.95
16P-90-04	0.0768	0.5007	0.0803	3160	82,182	4200	19.8	0.53
16P-90-05	0.0768	0.5043	0.0802	3231	83,418	4100	20.4	0.54
16P-45-01	0.0768	0.5058	0.0802	1554	40,002	5000	8.2	1.31
16P-45-02	0.0768	0.5040	0.0807	1371	35,420	4600	7.8	1.16
16P-45-03	0.0768	0.5033	0.0803	1447	37,433	4900	7.8	1.22
16P-45-04	0.0768	0.5030	0.0805	1166	30,183	3700	8.3	0.99
16P-45-05	0.0768	0.5018	0.0808	1222	31,707	4400	7.6	1.04
8P-0-01	0.0384	0.5027	0.0402	1595	82,632	5500	15.1	1.06
8P-0-02	0.0384	0.5022	0.0403	1391	72,135	4600	15.6	0.93
8P-0-03	0.0384	0.5033	0.0402	1143	59,137	4100	15.1	0.76
8P-0-04	0.0384	0.5023	0.0403	1124	58,270	4200	13.9	0.75
8P-0-05	0.0384	0.5035	0.0405	1147	59,324	4400	13.7	0.76
8P-90-01	0.0384	0.5015	0.0407	1610	83,603	5500	15.4	1.08
8P-90-02	0.0384	0.5027	0.0407	1596	82,684	5500	15.0	1.06
8P-90-03	0.0384	0.5022	0.0403	1711	88,730	5600	15.9	1.14
8P-90-04	0.0384	0.5023	0.0403	954	49,457	3600	11.8	0.64
8P-90-05	0.0384	0.5033	0.0403	992	51,325	3500	14.8	0.66
8P-45-01	0.0384	0.5037	0.0402	1191	61,580	4500	14.5	0.95
8P-45-02	0.0384	0.5027	0.0402	1198	62,065	4300	14.0	0.95
8P-45-03	0.0384	0.5027	0.0403	1201	62,220	4200	15.8	0.96
8P-45-04	0.0384	0.5022	0.0400	928	48,125	3700	14.2	0.74
8P-45-05	0.0384	0.5023	0.0400	840	43,547	3600	12.4	0.67

TABLE 8 - STRENGTH PREDICTION AT 45 DEGREES.

Designation	Maximum Strain Criteria	Tsai-Wu Criteria
8P-45 (psi)	65.1 x 10 ³	72.9 x 10 ³
16P-45 (psi)	30.6 x 10 ³	34.4 x 10 ³

The rogue flaw tests of specimens with holes generally achieved 53%-70% (see Table 7) of the value predicted by simplified analysis. In the tests of 16P-45 this percentage was greater primarily due to an underprediction of the strength in this direction by the maximum strain criteria. Theoretically, the stress concentration factor for this hole is greater than 3. The test results indicate a strength reduction factor less than 2 thereby indicating a significant redistribution of stress around the hole prior to failure.

4. RECOMMENDATIONS

The principal outcome of this preliminary study is to recommend an extensive testing program for the XCRV composite sandwich panels. These recommendations are summarized as follows:

1. Perform an exhaustive search of the literature for experimental results which may pertain to this material.
2. Perform a comprehensive test program to evaluate the structural response of the X-CRV sandwich panels at the sub-component and component scale. Correlate these test results to finite element analysis. Include environmental effects, defects and impact.
3. Supplement the laminate coupon tests with additional tests of the laminate and sandwich core system. These tests will help to interpret the results of 2) above. They should be made of constituents used in the above study.
4. Develop a comprehensive design criteria based upon the results of the above studies.

5. CONCLUSIONS

A comprehensive design criteria can not be developed from material coupon tests alone. Structural response from tests at the sub-component and component level are required. This is especially true in composites and composite sandwich panels where theoretical strength analysis is complex. There are a multiplicity of failure modes that depend upon structural geometry, load path and practical issues such as manufacturing techniques.

Experimental study of the sandwich panel as a whole is needed so that the global structural response be understood. Only then can a conservative and accurate design criteria be developed. The design procedure should be operationally simple and related to the methods of the analytical tool that will be used in design, typically finite element analysis. This criteria should include provisions for detecting any and all possible failure modes, both local and global. Conversely, localized material failure may not indicate failure of the structure or the component as a whole. Component testing will result in an assessment of reserve capacity.

A rational approach is required for preliminary design which is often performed in the absence of test results. Preliminary results presented in this report suggest that a simplified analysis can be used to predict the strength of a laminate coupon. Care should be exercised in choosing strength and strain parameters especially when there is not a significant number of plies in the laminate at an angle of 45 degrees or less. Environmental effects have yet to be included in this work. The so called "rogue flaw test" appears to be a promising method for assessing the effect of a defect in a laminate. This method fits in quite well with the philosophy of achieving a damage tolerant design.

REFERENCES

Crossman, F.W., "Analysis of Delamination", in Failure Analysis and Mechanisms of Failure of Fibrous Composite Structures, NASA Science and Technical Information Branch, NASA Conference Publication No. 2278, pp. 191-240.

Finn, S. R., Dickson, J. N., Vause, R. F. D, Carbery, J., Bowman, L.M. , Dost, E. F. and Starnes Jr., J. H.,(1995), "Analysis of a Pathfinder Shell Subjected to Internal Pressure and Mechanical Loads," Proceedings of the Fifth NASA/DoD Advanced Composites Technology Conference, NASA Conference Publication No. 3294, V1, P1, pp. 33-73.

Grimes, G.C., Dusablon, E.G., Malone, R.L., and Buban, J.P., (1993) "Tape Composite Material Allowables in Airframe Design/Analysis", Composites Engineering, Pergamon Press, Great Britain, V.3, N 7-8, pp. 777-804.

Hoskin, B.C., and Baker, A. A., (1986) Composite Materials for Aircraft Structures, American Institute of Aeronautics and Astronautics, New York, N.Y.

McCarthy, J. E.,(1983) "Commercial Transport Aircraft Composite Structures", in Failure Analysis and Mechanisms of Failure of Fibrous Composite Structures, NASA Science and Technical Information Branch, NASA Conference Publication No. 2278, pp. 7-66.

Noor, A.K., Shuart, M.J., Starnes, J.H., and Williams, J.G., (1983), Failure Analysis and Mechanisms of Failure of Fibrous Composite Structures, NASA Science and Technical Information Branch, NASA Conference Publication No. 2278, pp. 1-5.

Rowlands, R.E. (1985), "Strength Failure Theories and Their Experimental Correlation", Chapter 2, Failure Mechanics of Composites, Elsevier Science Publishers B.V., Amsterdam, The Netherlands. pp. 71-125.

Sih, G.C., and Skudra, A.M.,ed. (1985), "Failure Mechanics of Composites", Elsevier Science Publishers B.V., Amsterdam, The Netherlands.

Smith, P. J., Ilcewicz, L. B., and Olson, J.T. (1995), "Advanced Technology Composite Fuselage," Proceedings of the Fifth NASA/DoD Advanced Composites Technology Conference, Nasa Conference Publication No. 3294, V1, P1, pp1 -31.

"Standard Test Methods for Tensile Properties of Polymer Matrix Composite Materials", (1995) ASTM D3039/D3039M, American Society of Testing Materials, Philadelphia, Pa.

"Standard Test Methods for Shear Properties of Sandwich Core Materials", (1995) ASTM C273-94, American Society of Testing Materials, Philadelphia, Pa.

"Standard Test Methods for Flexural Properties Sandwich Construction", (1995) ASTM C393-94, American Society of Testing Materials, Philadelphia, Pa.

STUDIES OF THE INTERACTIONS BETWEEN
VESTIBULAR FUNCTION AND
TACTUAL ORIENTATION DISPLAY SYSTEMS

Roger W. Cholewiak
Cutaneous Communication Laboratory
Princeton University
Princeton, New Jersey 08544-1010

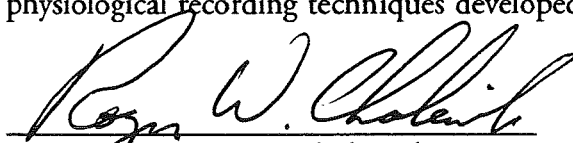
Millard F. Reschke
Space Biomedical Research Institute - SD5
NASA - Johnson Space Center
Houston, Texas 77058

57-53
038288
18P.
294264

When humans experience conditions in which internal vestibular cues to movement or spatial location are challenged or contradicted by external visual information, the result can be spatial disorientation, often leading to motion sickness. Spatial disorientation can occur in any situation in which the individual is passively moved in the environment, but is most common in automotive, aircraft, or undersea travel. Significantly, the incidence of motion sickness in space travel is great: The majority of individuals in Shuttle operations suffer from the syndrome. Even after the space-sickness-producing influences of spatial disorientation dissipate, usually within several days, there are other situations in which, because of the absence of reliable or familiar vestibular cues, individuals in space still experience disorientation, resulting in a reliance on the already preoccupied sense of vision.

One possible technique to minimize the deleterious effects of spatial disorientation might be to present attitude information (including orientation, direction, and motion) through another less-used sensory modality - the sense of touch. Data from experiences with deaf and blind persons indicate that this channel can provide useful communication and mobility information on a real-time basis. More recently, technologies have developed to present effective attitude information to pilots in situations in which dangerously ambiguous and conflicting visual and vestibular sensations occur.

This summer's project at NASA-Johnson Space Center will evaluate the influence of motion-based spatial disorientation on the perception of tactual stimuli representing veridical position and orientation information, presented by new dynamic vibrotactile array display technologies. In addition, the possibility will be explored that tactile presentations of motion and direction from this alternative modality might be useful in mitigating or alleviating spatial disorientation produced by multi-axis rotatory systems, monitored by physiological recording techniques developed at JSC.



Roger W. Cholewiak



Mill F. Reschke

STUDIES OF THE INTERACTIONS BETWEEN
VESTIBULAR FUNCTION AND
TACTUAL ORIENTATION DISPLAY SYSTEMS

Final Report
NASA/ASEE Summer Faculty Fellowship Program - 1996
Johnson Space Center

Prepared by:	Roger W. Cholewiak, Ph. D.
Academic Rank:	Senior Research Psychologist
University & Department	Princeton University Department of Psychology Princeton, New Jersey 08544
NASA/JSC Directorate:	Space and Life Sciences
Division:	Medical Sciences
Branch:	Space Biomedical Research Institute
JSC Colleague	Dr. Millard Reschke, Ph. D.
Date Submitted:	August 2, 1996
Contract Number:	NAG 9-867

STUDIES OF THE INTERACTIONS BETWEEN VESTIBULAR FUNCTION AND TACTUAL ORIENTATION DISPLAY SYSTEMS

Roger W. Cholewiak
Cutaneous Communication Laboratory
Princeton University
Princeton, New Jersey 08544-1010

Millard F. Reschke
Space Biomedical Research Institute - SD5
NASA - Johnson Space Center
Houston, Texas 77058

ABSTRACT

When humans experience conditions in which internal vestibular cues to movement or spatial location are challenged or contradicted by external visual information, the result can be spatial disorientation, often leading to motion sickness. Spatial disorientation can occur in any situation in which the individual is passively moved in the environment, but is most common in automotive, aircraft, or undersea travel. Significantly, the incidence of motion sickness in space travel is great: The majority of individuals in Shuttle operations suffer from the syndrome. Even after the space-sickness-producing influences of spatial disorientation dissipate, usually within several days, there are other situations in which, because of the absence of reliable or familiar vestibular cues, individuals in space still experience disorientation, resulting in a reliance on the already preoccupied sense of vision.

One possible technique to minimize the deleterious effects of spatial disorientation might be to present attitude information (including orientation, direction, and motion) through another less-used sensory modality - the sense of touch. Data from experiences with deaf and blind persons indicate that this channel can provide useful communication and mobility information on a real-time basis. More recently, technologies have developed to present effective attitude information to pilots in situations in which dangerously ambiguous and conflicting visual and vestibular sensations occur.

This summer's project at NASA-Johnson Space Center will evaluate the influence of motion-based spatial disorientation on the perception of tactual stimuli representing veridical position and orientation information, presented by new dynamic vibrotactile array display technologies. In addition, the possibility will be explored that tactile presentations of motion and direction from this alternative modality might be useful in mitigating or alleviating spatial disorientation produced by multi-axis rotatory systems, monitored by physiological recording techniques developed at JSC.

PHYSICAL LIMITS OF VIBROTACTILE SALTATION ON TWO BODY SITES: VOLAR THIGH AND LOWER ABDOMEN

INTRODUCTION The utility of tactile stimulation to provide for an alternative communication channel has been demonstrated when other sensory modalities were occluded, as in cases of deafness or blindness, or overloaded. Tactile patterns can also be used to provide information for spatial orientation, including direction, orientation, velocity, or attitude of the user in 3-dimensional space. These have been demonstrated by pilots maneuvering their aircraft using tactile displays in the complete absence of visual cues. One mode in which such patterns can be generated is to sequentially activate a line of tactors: The resulting sensation will be a moving point or a line drawn on the skin. An alternative to activating every tactor in a series would be to use the phenomenon of sensory saltation that requires as few as two physical sites to provide the sensation of many (e.g. 3-7) energized sites. In order to optimize the display, it would be important to know if the physical separation between the two sites has a limit, beyond which the illusion breaks down. Although a minimal form of the illusion has been explored on sites such as the fingertip, palm, forearm, and abdomen with punctate stimuli, this study extended these data to those sites to be used with tactile displays under construction, with stimulus patterns intended to generate the vector sensations useful for spatial orientation.

Sensory saltation was discovered by F. A. Geldard and C. E. Sherrick (1972) while they were examining a class of spatio-temporal phenomena (specifically the Tau and Kappa effects). These are all perceptual illusions in which judgments of either the spatial or temporal parameters among stimuli are influenced by the levels of the other parameter. Although the majority of these phenomena have been described in the sense of touch, Geldard extended his studies to show that sensory saltation could be demonstrated in the other spatial senses, of vision and audition (Geldard, 1975, 1976, 1977). The original description of the illusion implied motion by including the notion that it mimicked a "rabbit jumping up the forearm" (Geldard, 1975). There are a number of ways in which the sensation of motion like this might be generated on a sensory surface. Simply stimulating each of a linear array of lights or taps, *seriatim*, can produce the impression of one of these moving across the sensory field if the timing, spacing, and intensity are appropriate. A general pictorial representation of this mode may be seen in **Figure 1**, in which elements in the array of stimulators, represented in (A), are driven in the manner shown in (B) to produce the sensation represented in (E). The mode of pattern generation

called sensory saltation is also described in Figure 1, in (C) and (D).

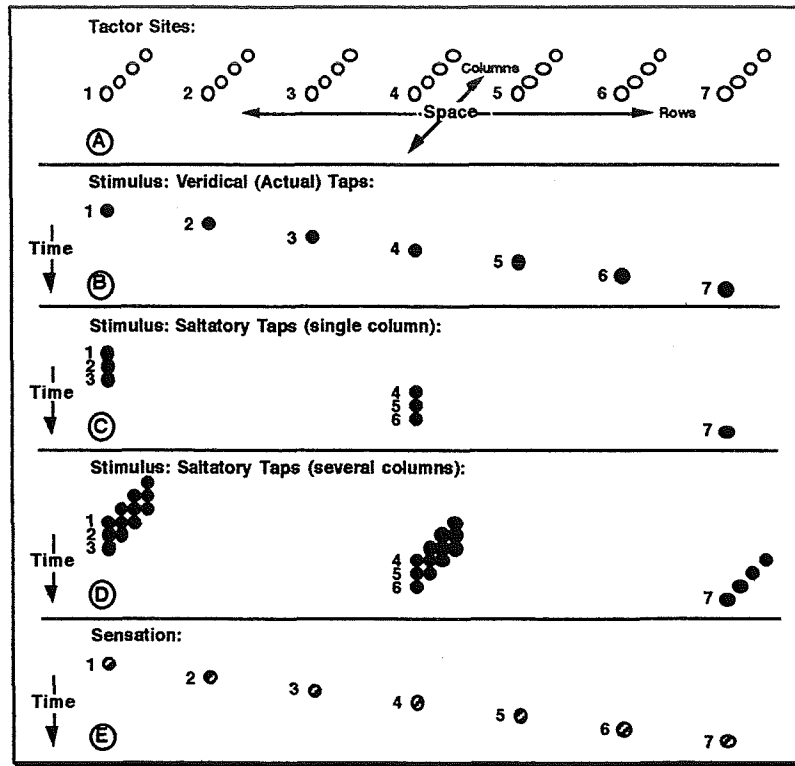


Figure 1. - Saltatory phenomena -spatial and temporal descriptions.

The essence of saltation is a mislocalization of one event, in space, as a consequence of presentation of another immediately following event. Although phenomena such as the Phi effect, and auditory localization are well-known, and illustrate the interdependence of space and time to produce specific emergent experiences in perception, saltation is unique in that the range of times over which it operates is larger than that controlling most other illusions, and the experience is one of mislocalization of specific events. For example, some types of auditory localization depend on critical temporal differences between events on the order of 160-200 μ sec (Evans, 1982). In auditory saltation, however, clicks generated by speakers distributed across the acoustic field, will be mislocalized with inter-stimulus intervals ranging from 20-250 msec. This is the same range of time delays that produce visual and tactile saltation.

Tactile saltation consists of a series of taps at one site that are mislocalized in a linear manner owing to the presence of one or more taps at a nearby second locus, presented temporally close to the last tap at the first locus (e.g., Cholewiak, 1976, Geldard, 1982; Geldard & Sherrick, 1983). Consequently, a series of taps at only a few sites (such as in

(C) in Figure 1) can appear to distribute themselves over an entire spatial extent (represented by the sensations in (E)). Note that four of the sensations are displaced spatially from their sites of generation. The advantage of saltation is that finely defined lines can be generated with many fewer veridical stimulus loci than are felt. Specifically, a well-defined finely dotted line made up of, e.g., seven or more individual taps can be produced with only two or three contactors, using the appropriate spatiotemporal parameters for the saltatory illusion. This trading relationship between space and time can generate finer detail than apparently possible, given the resolving power of the skin. One model of tactile pattern perception likens the skin to blurred vision (Loomis, 1990), in which it is hypothesized that the skin cannot resolve stimuli located close together because it acts like a low-pass filter for spatial detail. A pattern produced by saltation, however, is quite vivid and immediately apparent to subjects without extensive training or instruction. The manner in which apparent spatial frequency is thus increased by altering temporal frequency may be useful in attempts to generate accurate geometric features or flowing sensations on tactile displays. Furthermore, because of the ability to generate a spatially-distributed display with fewer generators than perceived sites, such a mode of presentation can be used in a fault tree. For example, if a line is normally generated by a series of seven taps produced by a line of seven stimulators, the saltatory mode can be invoked if intermediate stimulators fail. Using this mode and its specific spatio-temporal parameters, the same sensation of seven distributed taps (as in (B), above) could be produced by presenting the stimuli with only three tactors distributed over the same space with the equivalent temporal sequence of events (three at the first, three at the fourth, and a single one at the seventh, shown in (C) in Figure 1). Indeed, the sensations are indistinguishable on a number of quantitative and qualitative bases over a large range of temporal burst durations and interstimulus intervals (Cholewiak, 1996).

The temporal parameters of saltation have been well-explored by Geldard and his associates. However, the parameter that has not been as well evaluated with the multiple-tap saltatory generator is the appropriate physical separation (spacing) among tactors. The literature indicates that there is a physical limitation to the separation, but those studies were conducted with a minimal form of the phenomenon, using only two taps (Geldard, 1982; Geldard & Sherrick, 1983, 1986). In these cases, Geldard used the apparent displacement of a single tap to the skin produced by a pair of tactors whose physical separation was varied in several directions around a central point on the finger, palm, forearm, upper chest, or ventral thigh. Indeed there are limitations in distance whose magnitude

depend on the site being stimulated. Furthermore, asymmetries exist that are consistent with the possibility that the underlying neuroanatomical substrate is correlated with cortical receptive fields (see, esp., Geldard & Sherrick, 1983).

The two-tap version of saltation used in these previous studies is a particularly precise, but ephemeral version, certainly much less robust than those using several taps at each locus. The present study explores the spatial limits for saltation using forms of saltation and two body sites that might be practically used for orientation/ mobility displays. The saltatory modes involve multiple stimuli, and the body sites are the ventral thigh and the lower quadrant of the back. The specific question to be addressed concerns the influence of spatial separation between adjacent active tactors necessary for the perception of a continuous string of events across the space defined by the elements.

APPARATUS AND PROCEDURE A vibrotactile array consisting of seven enclosed piezoceramic beam benders (illustrated in **Figure 2, right**) was used to generate the stimuli. The contactors, attached to the benders as shown in **Figure 2, left**, were 7 mm in diameter. Each element was attached to the fabric substrate with Velcro™ so as to allow variable spacing, and was driven with a burst of 250 Hz sinusoidal vibration, with the timing and sequencing of the patterns controlled through the parallel port of a computer. In these initial studies, the bursts of vibration were always c. 40 msec long, as were the interburst intervals. Consequently, a 4-1 pattern involved 4 40-msec bursts of vibration at one locus, separated with an interburst interval of 40 msec, followed after a 40-msec delay with the final 40-msec burst at the terminal location.

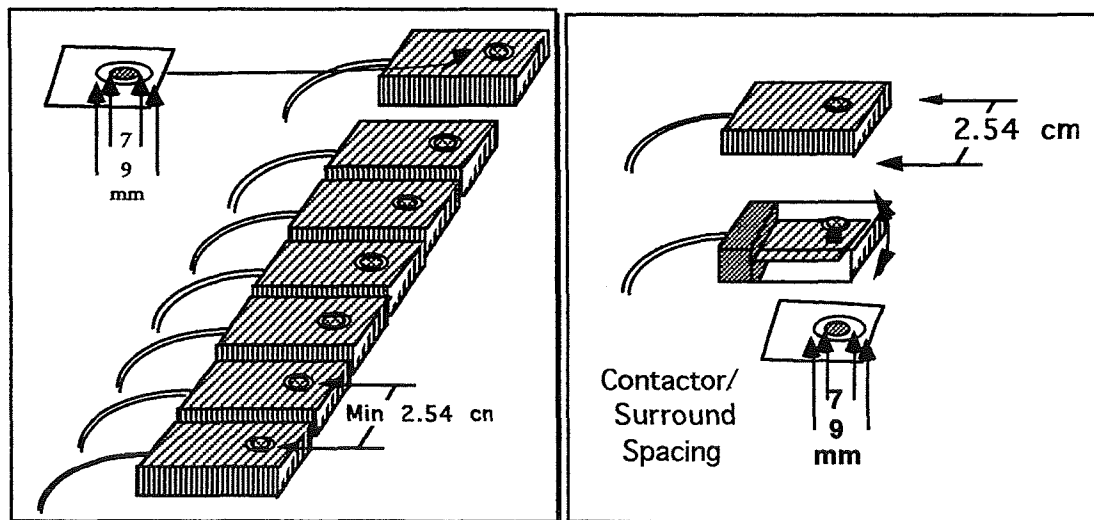


Figure 2. Linear tactile array (L) and individual tactors (R).

The array was either placed along the ventral surface of the left thigh or vertically along the left lower quadrant of the back of the seated participant touching the person through a fabric of "t-shirt" weight, and were held against the body with an elastic Velcro™ wrap.

The perceived intensity of an individual burst of vibration was estimated to be c. 20 dB re sensation level, although owing to local variation in sensitivity (see, e.g., Weinstein, 1968), there was a noticeable variation from site to site. To insure that all tactors touched the skin properly, prior to each testing session an "alignment" series was presented in which participants were required to indicate whether they felt each tactor activated individually with a brief weaker stimulus. If any tactors were not felt, the array was refit and the alignment series retested.

Testing involved the method of limits, in which the separation between the active contactors was functionally increased over successive trials. On each trial, the participant had to respond with a Yes/No keypress whether s/he felt a continuous pattern of individual taps running from the initial site to the terminal site. In cases in which the extent was not complete, a criterion was set that required displacement that covered at least 50% of the interstimulus space. A typical session involved four blocks of 42 trials (7 presentations of each of 6 physical separations, for example). Presentations were blocked by direction (proximo-distal (p-d) or disto-proximal (d-p) along the body's surface), and, in the case of the 4/6 and 1 presentations, by burst number. Consequently, a typical session might have a 6-1 d-p block, a 6-1 p-d block, and 4-1 d-p and p-d blocks of trials. See next section for descriptions of the tested patterns. Subjects wore headphones to mask ambient environmental noise.

STIMULUS PATTERNS: Two different saltatory generation modes are explored: In one version, (3-3-1) a saltatory image will be generated with the 7-element linear vibrotactile array in the manner described above in **Figure 1 (C)** - three bursts at the first and second active loci, with a single final burst of vibration at the terminal locus. The active loci on the 7-tactor array were functionally shifted to be adjacent (tactors 3, 4, & 5), one tactor apart (tactors 2,4, & 6), or two tactors apart (1, 4, & 7). The spacing of the elements on the array was adjustable, so three levels of tactor separation were implemented: 3 cm, 4 cm, or 5 cm. Consequently, a wide range of physical separations were available, depending on the functional and physical separations, ranging from 3 to 30 cm. In practice, the full range could not be used owing to restrictions on the distances available on the

body sites explored. The data indicate that this was not the limiting factor. The second mode tested (4-1 or 6-1) involved a number of bursts generated at the first locus (either 4 or 6 bursts, in separate blocks of trials), while only a single burst is presented at the second location, either adjacent or separated from the first by one or more quiet tactors (up to a limit of 5 quiet ones). In these cases, tactors were only separated by 3 cm, providing a range of functional separations from 3 to 18 cm.

PARTICIPANTS: Three members of the laboratory staff, including the P.I., served as participants in these studies. As indicated in the proposal, experienced, trained observers are more important in studies of this type. Each person served in each condition, typically for as many as 2 or even 3 or more blocks of trials.

RESULTS: Responses for each condition of mode and spacing were averaged across direction, with standard errors calculated to indicated variability. The number of observations/ condition ranged from a minimum of 112 to as many as 238. The results for these sessions are shown in **Figure 3** as the probability that a spatiotemporal pattern will produce a clear perception of mislocalization (i.e., that saltation occurred), as a function of the spacing between (4-1 or 6-1 pattern) or among (3-3-1 pattern) the active elements, with body site and stimulus mode as the parameters.

The data indicate that these stimuli will produce saltation more than 75% of the time using only two active contactors if the physical separation between tactors is less than 10 cm. This is true regardless of whether the back or the thigh is stimulated, and whether the pattern involves 4 or 6 stimuli occurring at the first site and only one at the second site. In the case of the 3-3-1 pattern mode, the data are less well ordered, but suggest that, on either body site, tactors might be placed as much as 12 cm apart and reliably produce saltation. Note that the functions shown in the **Figure** for the 3-3-1 modes consist of data collected in 3 separate blocks of trials (one with tactors separated by 3 cm giving effective distances of 3, 6, & 9 cm, one with tactors separated by 4 cm, producing distances of 4, 8, and 12 cm, and a third session with tactors separated by 5 cm, producing distances of 5, 10, and 15 cm.) It is possible that some of the noise in these functions results from changing criteria as the participant was tested in different sessions across the 3, 4 or 5 cm separations.

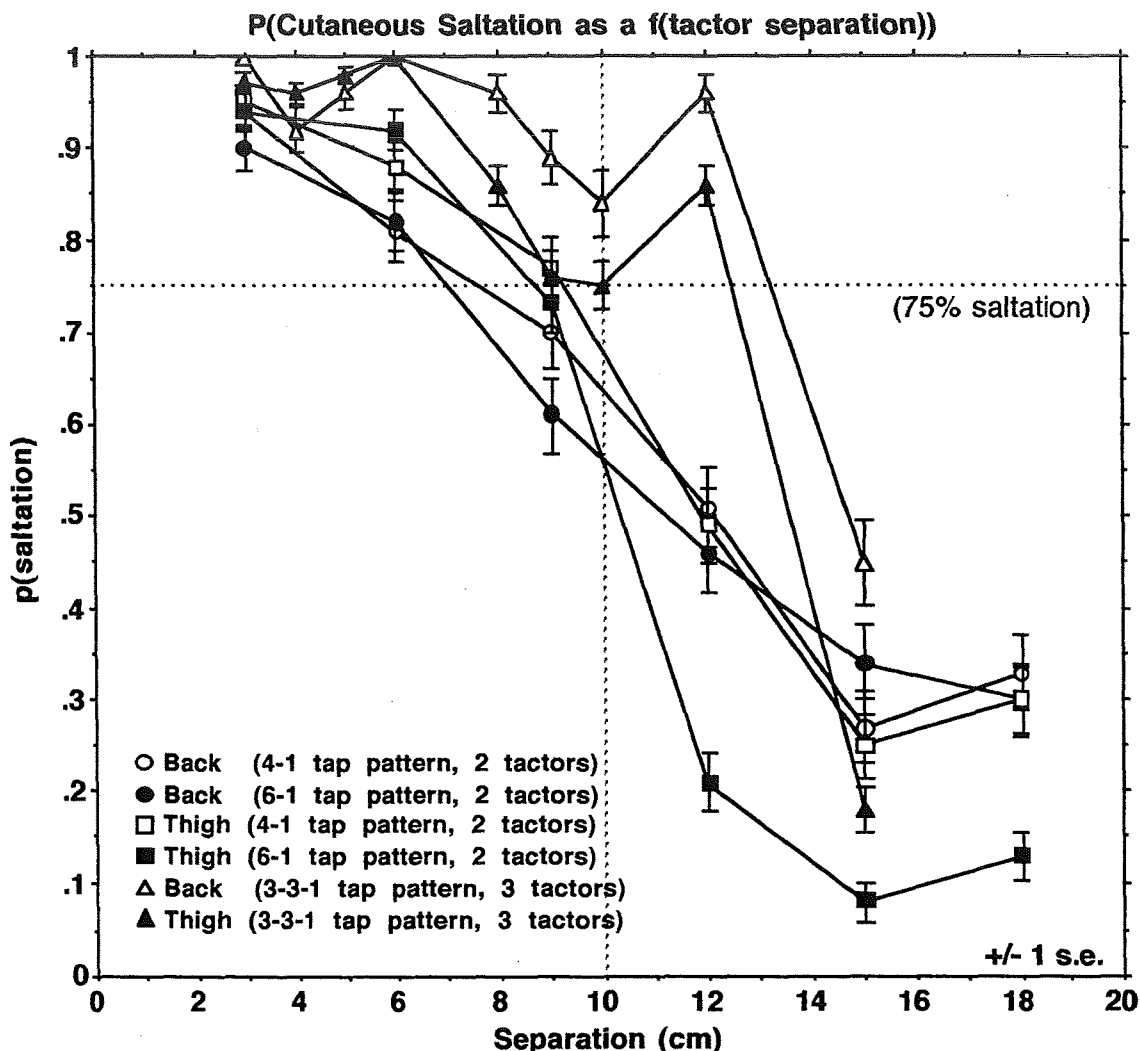


Figure 3. - Probability of saltation as a function of factor separation.

DISCUSSION AND CONCLUSIONS: These data indicate that, in a tactile array to be placed on either the ventral thigh or the lower quadrant of the back, elements should be spaced at the most 10 cm apart to reliably obtain sensory saltation with these pattern generation modes. Interestingly, there is a correspondence between these results and those obtained by Geldard for the more-difficult-to-observe 2-1 "reduced" saltatory pattern on the thigh (Geldard, 1983). In this case, he also found that saltation failed if the factors were separated by more than c. 10 cm, although there was an asymmetry in his results showing that longer separations were possible in the longitudinal direction (along the limb) than in the transverse direction (across the width of the thigh). He did not explore the back. The data collected in the present study suggest that saltatory areas, as generated by a number of different modes, may have equivalent spatial limits.

GROWTH OF THE PERCEIVED MAGNITUDE OF WHOLE BODY TILT USING THE METHOD OF ABSOLUTE MAGNITUDE ESTIMATION

RATIONALE: Having shown that good tactile movement could be produced with stimuli spaced c. 10 cm apart, this study was intended to collect baseline data regarding the perception of spatial disorientation - specifically tilt from vertical - prior to actually combining the tactile cue with the vestibular stimulus. A number of techniques have been used to evaluate individual's perception of whole body tilt, but the majority appear to involve a cross-modality matching of the magnitude of one sensory dimension (perceived whole-body tilt) to that of another sensory dimension (e.g., the location in space of an illuminated line). This project brings to bear the more-direct scaling method of absolute magnitude estimation, or, as Gescheider (1985) describes it, absolute scaling, to the problem of perceived body tilt. The potential advantage of this well-established technique is its independence from sensory interactions (see, e.g. Guedry, 1973; Stevens, 1975).

APPARATUS & PROCEDURE: For the vestibular task, observers were seated on a chair that could be tilted with respect to gravity. The chair could also be rotated, although there was no rotatory stimulus in this study. The rotator system was composed of a Contraves-Goertz Direct-Drive Rate Table (Model 824) mounted on a 1811-G19 Heavy Duty Pedestal. The rate table had a height of 42 in and diameter of 18 in, and could be tilted in the pedestal using a Duff-Norton Super-Pak MPA-6515-10/JB linear actuator. The chair, originally designed for the Microgravity and Vestibular Investigation (MVI) studies performed both as ground-based studies and on the Orbiter in space a number of years ago, had a 4-point restraint harness as well as a fixed helmet to secure the head during stimulation. When the observer was seated and restrained in the chair, a heavy black-fabric hood was drawn over the head and upper trunk to obscure any visual references to vertical. Each block of trials began with the chair in the zero degree tilt position. The constrained random series was begun once the subject was comfortable in the chair and the hood was properly positioned. Using a remotely controlled drive system, the experimenter moved the chair towards the first stimulus level, overshooting and returning in a number of steps to discourage the use of possible temporal cues resulting from the move from one stimulus position to the next. Once the stimulus position was reached, a ten-second settling period was imposed at the end of which the observer was directed to make an estimate (described next) of the magnitude of tilt. The next stimulus was always in the opposite direction. Consequently, the chair moved through zero degrees between

each stimulus position. In between blocks, the chair was returned to the zero position, and a brief rest period was provided in which the subject could remove the hood. As is typical in magnitude estimation procedures, only two blocks were presented to preclude the possibility of the observers learning or categorizing the stimuli. Observers were not told that the same positions were to be presented in each block, nor were they told what the maximal extent of tilt that was possible with the apparatus. When all participants served in the roll-tilt series, the chair was rotated 90 deg in the pedestal, and they returned for the pitch-tilt series.

STIMULUS: The independent variable in this experiment was the degree of whole-body tilt: tilt angle: 5, 10, 15, 20, 25, and 30 deg, presented randomly. In one session, tilt was presented in two roll (side-to-side) directions (right or left), while in a second session, two pitch (front-to-back) tilt directions were presented. Each of the six degrees of tilt in the two directions (12 stimuli) were randomly presented twice per session in two separate blocks of trials. Observers gave their responses verbally.

MAGNITUDE ESTIMATION: After the procedure was briefly described to the participant, but prior to the main study reported here, a brief preliminary training series was conducted to explain and familiarize each person with the method of absolute magnitude estimation. This series required observers to make judgments of the magnitude of line lengths, which is a relatively easy task that appears to stabilize loudness scaling (Stevens, 1975; Zwislocki & Goodman, 1980; Zwislocki, 1983). Lines were presented in the brief training series by presenting a number of lines drawn on white paper to the observer, who gave their estimates verbally.

Observers were read these introductory remarks:

Today we will do a magnitude estimation experiment. Because the magnitude estimation procedure is very sensitive to the actual words that are used in the instructions, I am going to read these to you.

In this experiment, we would like to explore the ideas you have about the sizes of a number of things. Specifically, we would like to find out how intense various stimuli seem to you. In this first familiarization series, we will start with some lines of different lengths. First, I would like you to imagine a long line, . . . and a large number. Now imagine a short line, . . . and a small number. You can do this because you have ideas about the sizes of lines and numbers. I will now actually show you a series of lines. Your task will be to assign a number to every line in such a way that your impression of how large the number is matches your impression of long the line is. You may use any positive number that seems right to you- whole numbers, decimals, or fractions. Just assign a number to each line so that the size of the number matches your impression of the length of the line. Judge each stimulus as if it was presented in isolation. In other words, try not to compare it to the other stimuli that have been presented to you. If you feel that you must make a comparison, make

it with all the lines and all the numbers that you have had experience with or can imagine. Just assign a number to each line so that your impression of the size of the number and your impression of the length of the line match in magnitude. Do you have any questions?

Stimuli were briefly shown to the observer and their responses recorded. Following the visual task, the next set of instructions were read to the observer:

OK - that was a magnitude estimation procedure. Do you feel comfortable with it? Earlier I asked you to imagine a long line and a large number. You could do this because before we even started today you had ideas about what is big and small for lines and numbers. Now we will do the tilt experiment itself in which you will do several more blocks of magnitude estimation trials. In this case, we will ask you to focus on your perceptions of the magnitudes of numbers and of tilt positions in different orientations. Now, just as with the lines, I would like you to imagine a strong body tilt, . . . and a large number. Now imagine a weak body tilt, . . . and a small number. Again, you can do this because you have ideas about the sizes of numbers and the amounts of whole body tilt.

In this experiment there will be two blocks of magnitude estimation trials. I will present a series to you, one at a time, with a brief break between blocks. In some of the trials the stimulus will be of a high amount of tilt, and in others it will be less. Your task will be to assign a number to every stimulus in such a way that your impression of the magnitude of the number size matches your impression of the magnitude of the amount of whole-body tilt. Use any positive number that seems right to you-whole numbers, decimals, or fractions. As before, judge each stimulus as if it was presented in isolation. In other words, do not try to compare it to the other stimuli that have been presented to you. Respond as quickly and spontaneously as you can. We will support your head by putting it into a helmet, will ask that you wear a hood to mask the visual vertical cues in the room, and will support you firmly in the tilt chair. Try to relax. Any questions?

Finally, the observer was seated in the tilt-chair system, restrained with the harness, had the helmet-hood placed down over the head, and the tilt series began as described above.

PARTICIPANTS: Ten members of the laboratory staff served as participants in this study. There were three females and seven males. None of the observers had participated in magnitude estimation studies previously, and only one had experienced whole-body tilt in which he was required to make estimates of his actual position in degrees from vertical. Each person served in all conditions

RESULTS: Because magnitude estimates have been shown to be logarithmically distributed, geometric means of the estimates from all of the observers were calculated and plotted as a function of actual tilt angle. The group data for the first condition (in which roll was the direction of tilt) can be seen in **Figure 4**. Plotted in the Figure are the estimates for tilt in the positive direction (+ = right), negative direction (- = left) and the average over the two directions. Also shown are bars indicating standard errors of the estimates. Although they were not statistically tested, the variability among the functions suggests that there were no significant differences among the functions. Also shown in the

figure are the power functions fit to [logarithmic transforms of] these data by the method of least squares. Exponents of these functions are all greater than 1 - averaging 1.547 - and the regression coefficients indicate that these data are extremely well-fit by the functions.

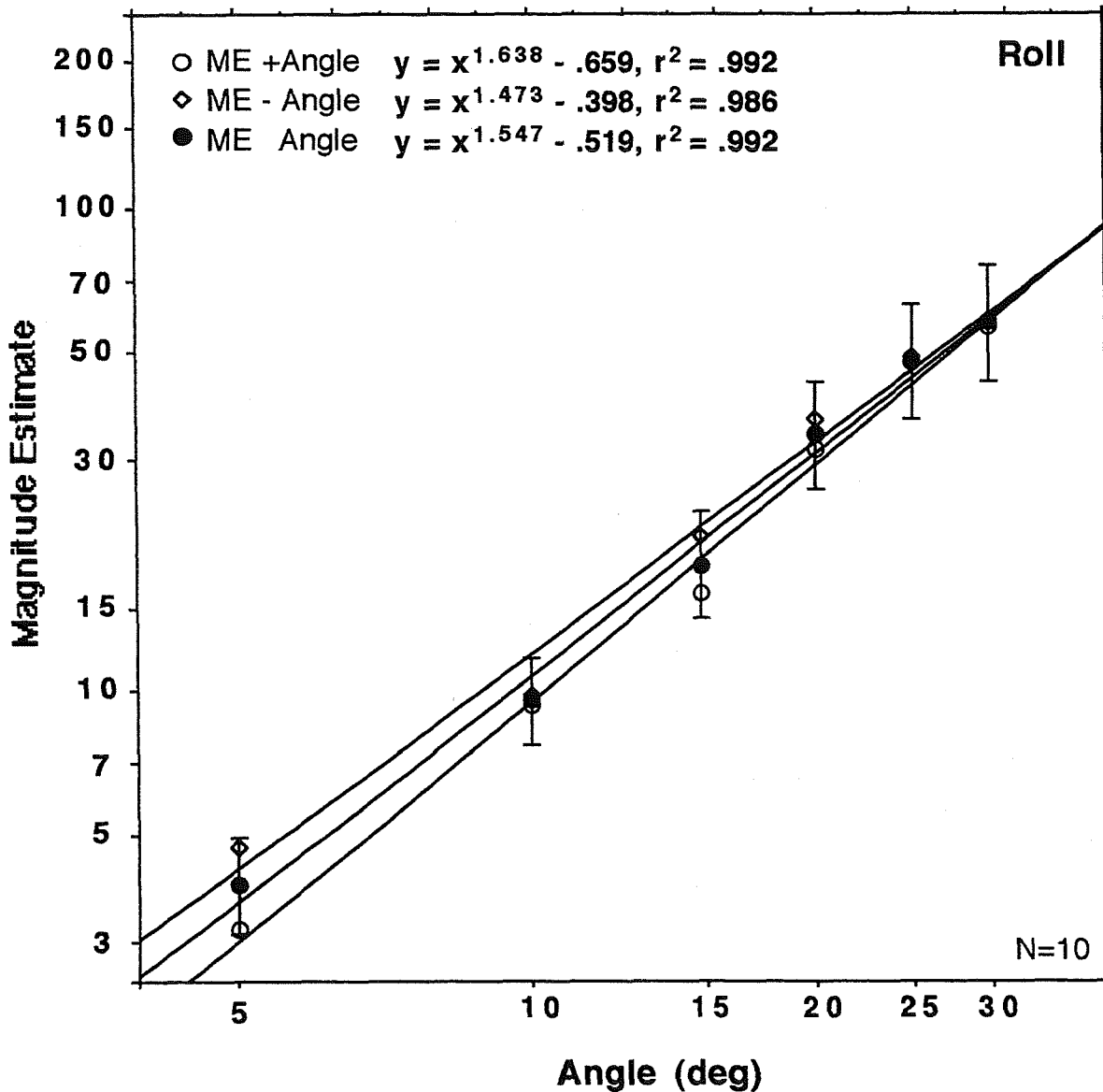


Figure 4. - Magnitude estimates of whole body roll as a function of degree of tilt.

In Figure 5 are plotted the data for estimates of whole body tilt in the pitch direction (to and fro). In this case, note that data are incomplete: only three of the above observers served in this study. The experiment was unexpectedly terminated owing to equipment failure. Error bars are not shown because of the small number of participants for whom data are shown. Nevertheless, points are well fit by the functions, indicated by

the regression coefficients of the power functions fit to [logarithmic transforms of] these data by the method of least squares. As with roll tilt, exponents of these functions are all greater than 1 - averaging 1.255. Caution is advised regarding comparisons of these functions with Figure 4, because individual number usage of the missing observers could influence both the slopes and the intercepts of these functions. However, the function derived from the roll data for the same three subjects is shown in Figure 5, for comparison.

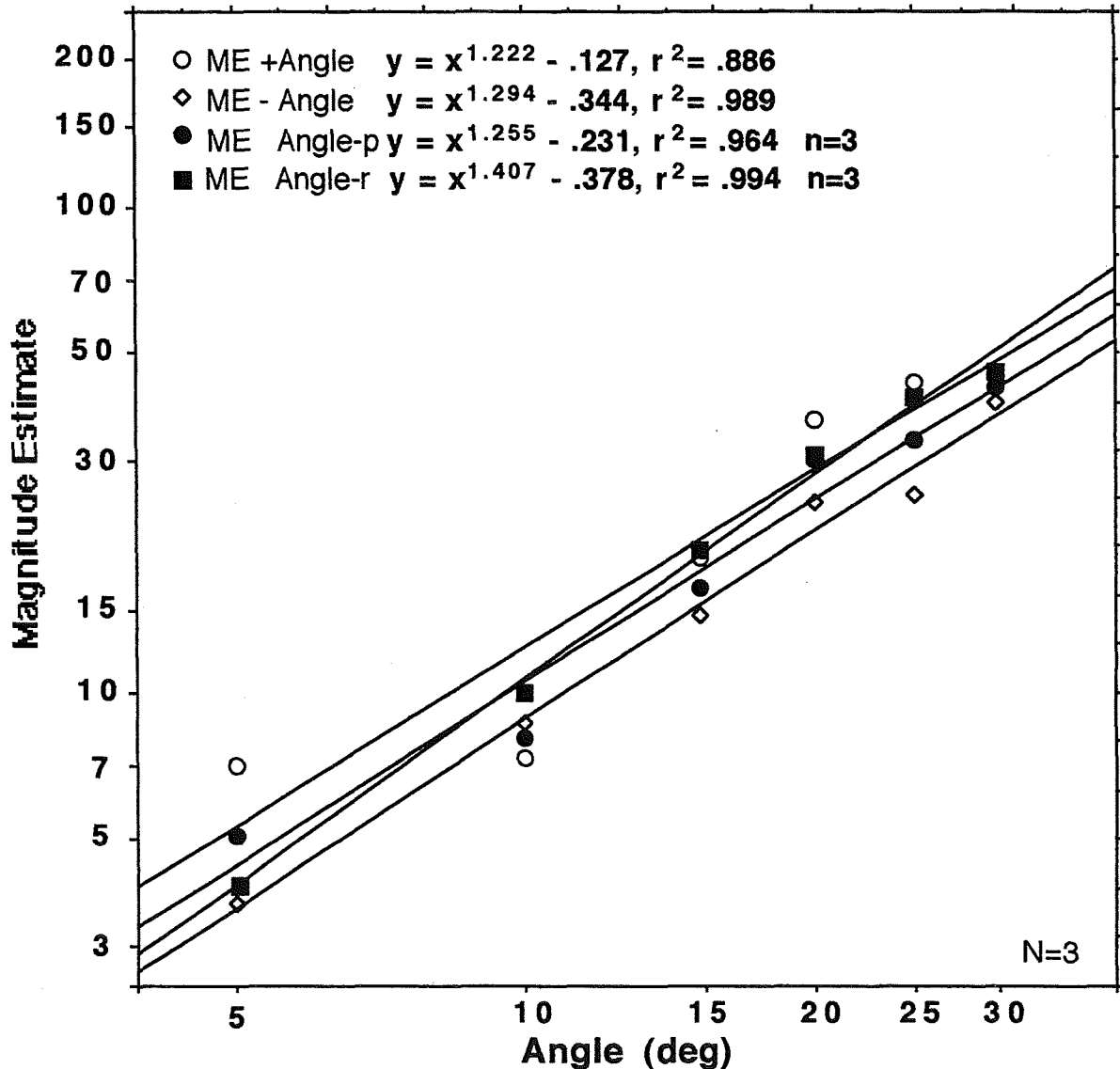


Figure 5. - Magnitude estimates of whole body pitch as a function of degree of tilt.

CONCLUSIONS: The functional relationships illustrate the expansive nature of the degree of roll (or pitch) and the amount of perceived tilt: people feel as though they are more tilted than the physical stimulus would suggest.

NOTE

The author would like to express his appreciation to Ms. Charmaine Mangram for her assistance and participation and Ms. Amy Wiseman for her patient and attentive extended participation as an observer in these studies. This research was conducted while the author was a NASA/ASEE Summer Faculty Fellow at the Space Biomedical Research Institute at the Johnson Space Center, Houston, TX.

REFERENCES

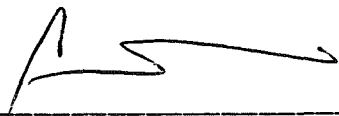
- Cholewiak, R. W. (1976). Satiation in cutaneous saltation. Sensory Processes, 1, 163-175.
- Cholewiak, R. W. (1996). Parameters for the Tactile Display of Spatial Orientation Information. Progress and Productivity Report on ONR Grant No. N00014-95-1-0387 Office of Naval Research, July 1, 1996.
- Evans, E. F. (1982). Functional anatomy of the auditory system. In H. B. Barlow & J. D. Mollon (Eds.), The senses (pp. 251-306). Cambridge: Cambridge University Press.
- Geldard, F. A., & Sherrick, C. E. (1972). The cutaneous "rabbit:" A perceptual illusion. Science, 178, 178-179.
- Geldard, F. A. (1975). Sensory saltation: Metastability in the perceptual world. Hillsdale, NJ: Lawrence Erlbaum Associates.
- Geldard, F. A. (1976). The saltatory effect in vision. Sensory Processes, 1, 77-86.
- Geldard, F. A. (1977). Cutaneous stimulation, vibratory and saltatory. J. Investigative Dermatology, 69, 83-87.
- Geldard, F. A. (1982). Saltation in somethesis. Psychological Bulletin, 92, 136-175.
- Geldard, F. A., & Sherrick, C. E. (1983). The cutaneous saltatory area and its presumed neural basis. Perception & Psychophysics, 33, 299-304.
- Geldard, F. A., & Sherrick, C. E. (1986). Space, time and touch. Scientific American, p. 91-95.
- Gescheider, G. A. (1985). Psychophysics: Method Theory, and Application. Erlbaum: Hillsdale, NJ.
- Guedry, F. E. (1973). Psychophysics of vestibular stimulation. In Handbook of sensory physiology (pp. 3-154). New York: Springer-Verlag.
- Loomis, J. M. (1990). A model of character recognition and legibility. Journal of Experimental Psychology: Human Perception and Performance, 16, 106-120.
- Stevens, S. S. (1975). Psychophysics: Introduction to its perceptual, neural, and social prospects. New York: Wiley.
- Weinstein, S. (1968). Intensive and extensive aspects of tactile sensitivity as a function of body part, sex, and laterality. In D. R. Kenshalo (Eds.), The skin senses (pp. 195-222). Springfield, IL: Thomas.
- Zwislocki, J. J. (1983). Group and individual relations between sensation and magnitudes and their numerical estimates. Perception & Psychophysics, 33, 460-468.
- Zwislocki, J. J., & Goodman, D. A. (1980). Absolute scaling of sensory magnitudes: A validation. Perception & Psychophysics, 28, 28-38.

58-91
038289
doc.
297/265

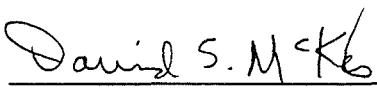
**There's Iron in Them Thar Hills:
A Geologic Look at the Aristarchus Plateau as a
Potential Landing Site for Human Lunar Return**

Dr. Cassandra R. Coombs
College of Charleston
SN
August 1, 1996

Dr. David S. McKay
Earth Science and Solar System Exploration Division
Space and Life Sciences Directorate



Cassandra R. Coombs, Ph.D.



David S. McKay, Ph.D.

**There's Iron in Them Thar Hills:
A Geologic Look at the Aristarchus Plateau as a
Potential Landing Site for Human Lunar Return**

Final Report

NASA/ASEE Summer Faculty Fellowship Program - 1996
Johnson Space Center

Prepared by:	Cassandra R. Coombs, Ph.D.
Academic Rank:	Assistant Professor
University & Department:	College of Charleston Geology Department 58 Coming Street Charleston, S.C. 29424
NASA/JSC	
Directorate:	Space and Life Sciences
Division:	Earth Science and Solar System Exploration
JSC Colleague:	David S. McKay, Ph.D.
Date Submitted:	August 1, 1996
Contract Number:	NAG 9-867

ABSTRACT

Lunar pyroclastic deposits are unique among lunar soils. Composed of very fine grained glass beads rich in Fe, Ti and Mg they yield unique spectral signatures. From the spectra two major classes and five subclasses of lunar dark mantling deposits have been identified. Recent work by me and others has shown that the larger regional deposits are more numerous, extensive, thicker, and widely distributed than previously thought, leading us to suggest that they would make ideal resource feedstock for future lunar surface activities. Returned sample studies and the recently collected Galileo and Clementine data also corroborate these findings. Recent planning for return to the Moon indicates that large cost savings can result from using locally produced oxygen, and recent JSC laboratory results indicate that iron-rich pyroclastic dark mantling deposits may be the richest oxygen resource on the Moon. My earlier work demonstrated that instead of using regolith, bulk lunar pyroclastic deposits are better suited for beneficiation as they are thick (10's m's), unconsolidated, fine-grained deposits. In addition, the lack of rocks and boulders and the typically flat to gently rolling terrain will facilitate their mining and processing. In preparation for the Human Lunar Return (HLR) I have characterized the Aristarchus Plateau (24°N 52°W) as a potential landing site for an in-situ resource utilization (ISRU) demonstration. The geologic diversity and large volume of Fe-rich pyroclastic material present at the Aristarchus site make it an ideal target for extracting O₂, H₂ and halogens. This paper (1) describes the current understanding of the geology of Aristarchus plateau; (2) describes the resource potential of the Aristarchus plateau ; and (3) presents several candidate landing sites on the plateau for future lunar activities.

There's Iron in Them Thar Hills: A Geologic Look at the Aristarchus Plateau as a Potential Landing Site for Human Lunar Return

INTRODUCTION

The NASA Strategic Plan calls for the US to open the space frontier by exploring, using, and enabling the development of space and to expand the human experience into the far reaches of space. [1]. More specifically, Goal 2 of the Human Exploration and Development of Space (HEDS) Enterprise calls for the U.S. to Explore and settle the Solar System [2]. As part of this, NASA is studying a small return mission to the Moon. This mission will be driven by more than pure science. The currently planned mission is focused on in-situ resource utilization and demonstration. However, much good science will accompany the mission. The location of the lunar base at a geologically interesting site such as Aristarchus will permit the investigation of the composition and mode of emplacement of basin ejecta, the impact cratering process, the nature and origin of crater rays, the formation of sinuous rilles, and the compositions and eruption styles of a variety of mare basalt units in the process of characterizing and defining the pyroclastic deposits in situ.

This study is a compilation of both orbital and Earth-based photographic and remote sensing observations. It began in support of NASA's Human Lunar Return mission. This past year NASA Administrator Dan Goldin requested that a feasibility study be conducted to return humans to the Moon. To be viable, this mission must not only return humans to the Moon but provide something new. That something new is technology. For the first time in history, this mission will investigate the potential for generating needed O₂ and He and other resource materials from another planetary surface, in this case, the lunar dark mantling deposits. Aristarchus is a site that is not only geologically interesting, but one that can provide an added benefit - resources. Careful evaluation of the returned Apollo sample data and imagery combined with the recent Clementine UV/VIS data confirm the resource potential at Aristarchus.

BACKGROUND

The Aristarchus Plateau is located in central northeastern Oceanus Procellarum on the lunar nearside (25°N 52°W). For years the Aristarchus Plateau has been a subject of interest to lunar scientists. It is one of the most geologically diverse regions for its size on the lunar surface. Recognized early in the Apollo days as being unique, it became an early candidate Apollo landing site when early site selection discussions stressed the need for geologic diversity and traverse distance.

The plateau is geologically diverse. Its surface is riddled with impact craters and secondary crater chains, volcanic constructs and pyroclastic deposits as well as many sinuous rilles and scarps (Figure 1). Among the geologic features are a blanket of anomalously red dark mantling material; the densest concentration of sinuous rilles as well as the Moon's largest lava channel, Schröter's Valley; apparent volcanic vents, volcanic sinks or depressions, volcanic domes; mare materials of various ages and colors; one of the freshest large craters with ejecta of varying unique colors and albedos; and other large craters in different states of flooding and degradation [3]. In addition to these geologic features, the three best authenticated lunar transient phenomena were observed emanating from the plateau area, which may or may not be due to presence of KREEP-rich materials in the region. Previous work by [4] and [5] suggested that pyroclastic deposits would make an ideal lunar base site. Past attention has focused on the production of H₃ as a nuclear fusion fuel and oxygen propellant [6,7,8,9].

What are pyroclastic deposits?

Lunar pyroclastic deposits are very smooth, low albedo (0.079 - 0.096:[10]) units that mantle and subdue underlying terrain. First found as whole and broken glass beads at Apollo 15, numerous classes of glass beads are now recognized in the returned Apollo sample collection. On the Apollo 17 mission orange glass beads and their quench-crystallized equivalents were identified at Station 4, Shorty Crater. Interpretations of their origin have swayed from (1) vapor condensates [11,12], (2) impact melt ejecta from large impacts which had penetrated to more mafic material at depth [13,14]; (3) splash droplets from impacts into lava lakes [15] or (4) pyroclastic material [16,17,18,19,20,21]. The latter, explosive volcanic origin is now commonly accepted for the well studied Apollo 17 and Apollo 15 returned glass beads and partially devitrified spherules. Recent studies have also demonstrated that explosive volcanism is responsible for the formation of the other dark mantle deposits on the lunar surface (e.g., 22,23,24,25,26).

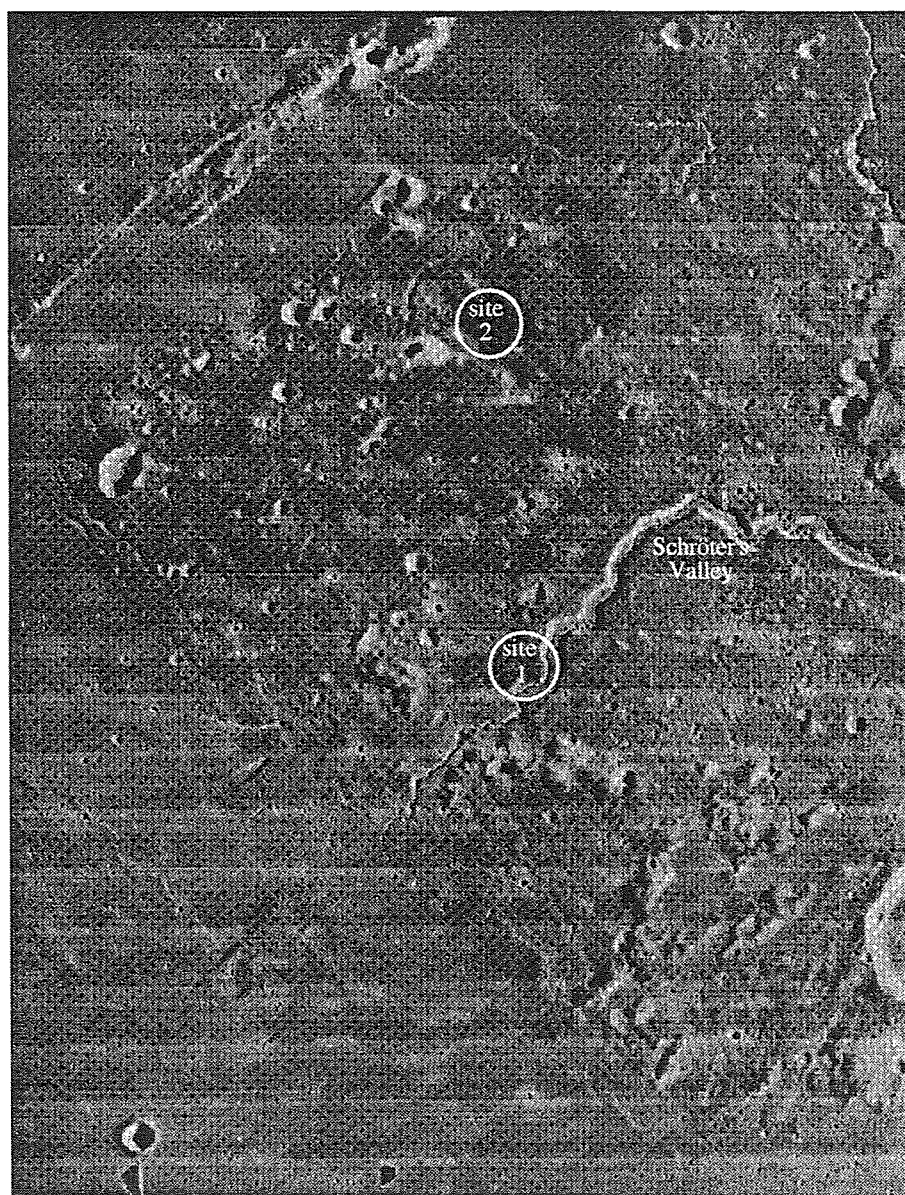


Figure 1: Lunar Orbiter IV photograph of the Aristrarchus Plateau. The circles denote the suggested landing sites. Each is approximately 10 km in diameter.

Modeling by Coombs and Hawke, Hawke et al., and Coombs [4,22,24] has demonstrated the nature and method of emplacement of the explosive volcanic materials. Two different methods are thought to be responsible for these dark mantle materials, based on their distribution and spectral signatures. Work by Gaddis et al., Coombs, and Hawke et al. [23,24,25] and others has demonstrated that regional pyroclastic deposits differ from localized dark-mantle deposits in that they typically cover several thousand square kilometers and were emplaced as a result of strombolian-type or continuous eruption column activity. The localized deposits, on the other hand are, are much smaller in that they are generally less than 250 km to around 550 square kilometers and were emplaced by a more short-lived eruption mechanism like the terrestrial vulcanian eruptions. See [4, 22-26] for more specific information.

DATA

Multiple data sets were used for this preliminary site study. Among them are, Apollo 15 Hasselblad and Metric Mapping Camera images, Lunar Orbiter IV and V panchromatic frames, Clementine multispectral data in the UV/VIS range, ground-based telescopic spectra in the UV/VIS to near-IR, orbital geochemistry and ground-based radar.

Imagery

Hand-held Hasselblad photos from the orbiting Apollo 15 Command Module were used as a cursory tool to locate the pyroclastic deposits on the Plateau. Close inspection of the Apollo 15 metric mapping camera frames revealed sufficient detail to pinpoint potential resource areas, volcanic source vents and rilles, and ejecta blocks in the study areas. In addition, the southward looking metric frames provided a low sun-angle view for more clearly distinguishing feature morphology. The incident sun angle ranges between 10-12° on the frames used. The Lunar Orbiter IV and V frames provided a different view for the study areas. With a spatial resolution of approximately 10 km, and a different lighting angle than the mapping camera the Orbiter frames nicely complement the metric mapping camera images and provide a more effective concept of distance and scale.

Clementine

Following the return of Clementine multispectral data McEwen et al. [27] developed a rudimentary mosaic of the Aristarchus Plateau soon after the Clementine data were received (Figure 2). I used their mosaic as a base for this study. A 30 km by 40 km subset of these data were extracted for closer analysis and assistance with site identification. McEwen et al. [27] examined the initial Clementine data for the Aristarchus region. They mosaiced more than 500 images in three spectral bands using the UV/VIS data; 415 nm, 750 nm, 1000 nm. To create a color ratio image, the 750/415-nm ratio image was assigned to the red channel, the 750/1000-nm ratio image to the green channel and the 415/750-nm ratio image to the blue filter (Figure 3). Most striking in this RGB image are the pyroclastic deposits which are a distinct red and red-orange. The blue areas in the image denote lobes of highland material extending asymmetrically west-northwest of the crater Aristarchus for 75-100 km. This distribution is consistent with previous studies [28, 29]. The yellowish areas in the image correspond to late stage ejecta removed from the crater rim which expose fresh mare basalt. The purplish or reddish units correspond to the red or blue mare units. Given the expected excavation depth of 1/3 - 1/10 the crater diameter, McEwen et al. [27] estimate the pyroclastic mantling thickness at between 10-30 m.

Ground-based spectra

Many spectral studies have been conducted of the Aristarchus region. Coombs[24] and Hawke et al. [25] looked at the localized pyroclastic deposits on the plateau. Ground-based spectra collected of this area indicate an additional Fe-bearing soil component. The spectra are broader and exhibit a longer-wavelength absorption band than the Taurus-Littrow dark mantle deposit. In addition, this higher Fe content helps to maintain the low albedo of these deposits.

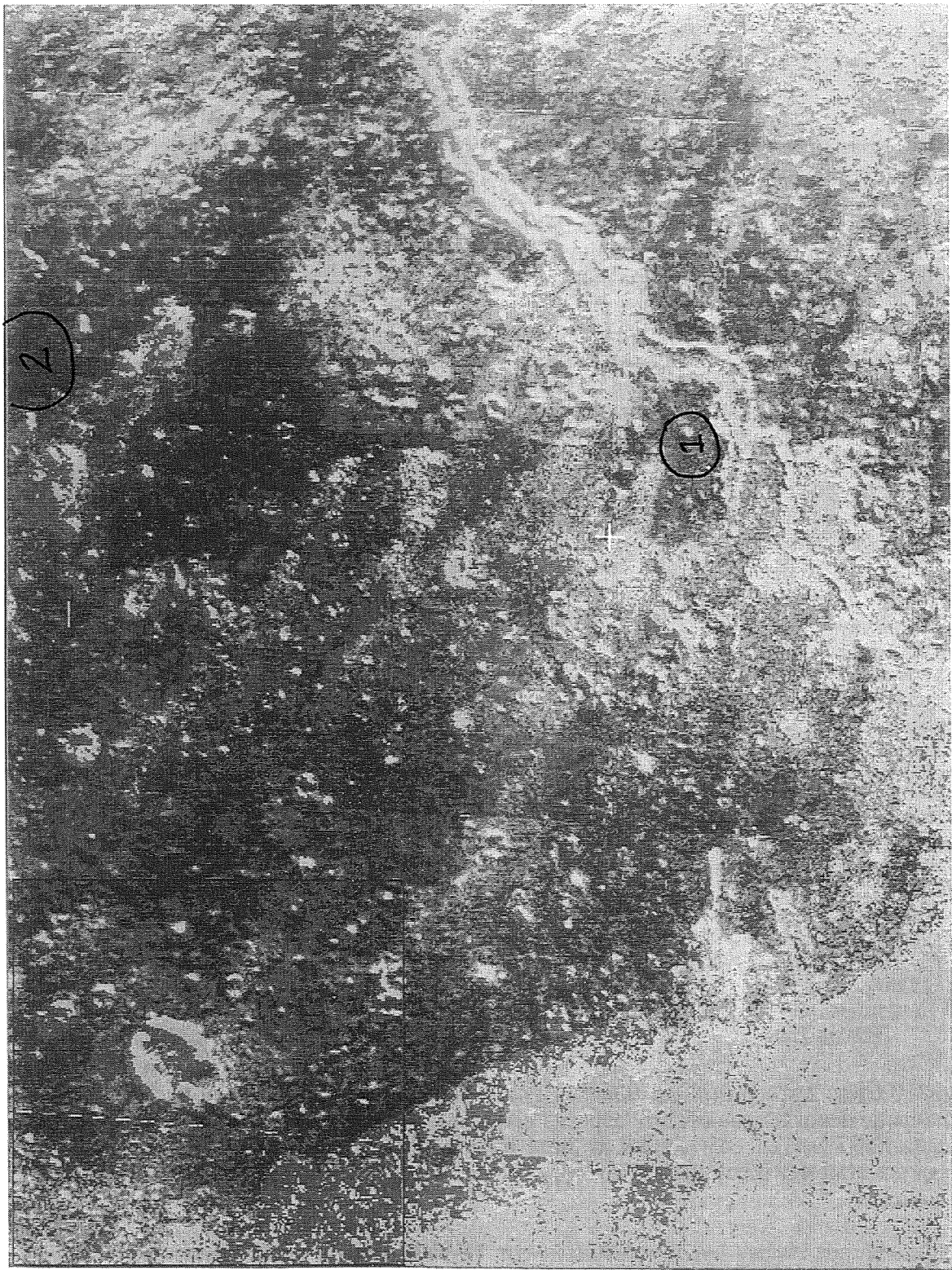
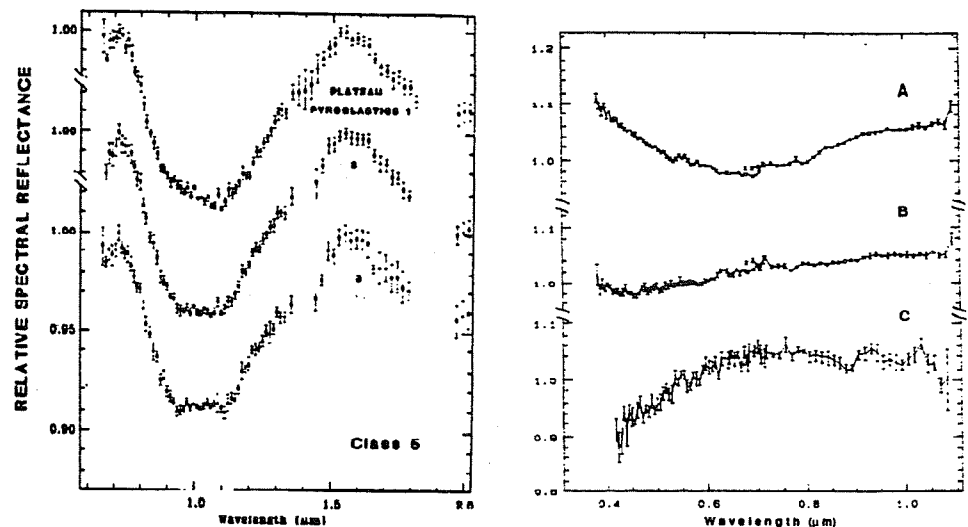


Figure 2: Clementine multispectral mosaic of the Aristarchus Plateau. Red and red-orange areas denote pyroclastic materials where we hope to process O₂ and He. Modified from [27]. Composed of three band ratios: 750/415-nm (red), 750/1000-nm (green), 415/750-nm (blue).

UV/VIS spectra collected from different areas on the plateau indicate a high Fe, moderate Ti composition (Figure 3, right). In particular, the higher resolution spectra presented by Hawke et al. [30] were collected over 120 channels versus the previous 24 channel spectra presented by Pieters et al. [31]. The 1991 spectra have a much improved spectral sampling and slightly enhanced resolution that can be used to identify mineral absorption features that were previously undetectable in the lower resolution data.

Near-infrared (near-IR) spectra for regional pyroclastic deposits presented by Gaddis et al. [23] were divided into two distinct classes. Regional Class 1 spectra exhibit broader, longer-wavelength absorption bands than those that can be attributed to just pyroxenes in mare or highland soils. This spectral signature suggests that an additional Fe-bearing soil component is present to modify the 1- μm band and maintain the low albedo of the materials observed. This finding is consistent with the presence of Fe^{2+} -bearing volcanic glass-rich mantling deposits on the Plateau and is supported by all available spectral evidence [23,24,25,30, 32]. The pyroclastic deposits atop the Aristarchus plateau fall into this category (Figure 3). Another pyroclastic mantling deposit within this spectral subclassification is a fairly large deposit just southwest of Mare Humorum.

Figure 3: UV/VIS spectra collected from Mauna Kea by [30] for three different lunar dark mantle deposits with potential for resource extraction and utilization. Left spectra are near-infrared spectra from the Aristarchus Plateau [32]. Right spectra are in the UV/VIS range from (a) Taurus Littrow (b) Sulpicius Gallus (c) Aristarchus Plateau [30].



Regional Class 2 spectra on the other hand have signatures nearly identical to the Taurus-Littrow dark mantle deposit. Each of these deposits bears a spectral signature indicating a predominance of ilmenite-rich black spheres similar to those returned from the Apollo 17 Station 4 site. Other deposits within this spectral class are Rima Bode, southern Mare Vaporum and southern Sinus Aestuum.

The Aristarchus Plateau has low 0.40/0.56- μm UV/VIS values and relatively high values in the near-IR (see Figure 3, left). The steep infrared continua, low albedo and very broad absorption centered longward of 1 μm has been attributed to Fe^{2+} -bearing glass, as mentioned above [32]. These data are consistent with those presented in previous studies based on multispectral imagery and color-difference photography [32, 33, 34]. The strong Fe^{2+} absorption signature indicated by the Aristarchus spectra does not necessarily connote a dominate composition of black spheres and orange glass as collected at Apollo 17. Instead, work by Davies et al. [35] and Johnson et al. [36] suggest that the Aristarchus spectral signatures are indicative of the presence of glass-rich pyroclastic materials that are compositionally unrelated to those sampled by Apollo 17. Lucey et al. [32] argued that mixtures of Apollo 17 orange glass and black spheres would not yield spectra with the characteristics exhibited by the Aristarchus Plateau mantle deposits.

The large aerial extent of this deposit may protect parts of it from surface contamination by larger impact ejecta, limiting the effects of secondary impacts and lateral mixing. The relatively large thickness (10-30 m) of this deposit is deep enough that the smaller impact craters in the 10-100's m size range have generally not penetrated the dark mantle material and ejected or exposed subjacent blocky material. Perhaps, as previously suggested by Zisk et al. [33], the Aristarchus dark mantle materials are themselves covered with a thin layer of Aristarchus crater ejecta and fine grained highlands-rich materials that are masking the strong pyroclastic characteristic signature.

Orbital geochemistry

The Apollo 15 command module carried several geochemical experiments onboard including a gamma ray spectrometer, an X-ray fluorescence spectrometer, and an α -particle spectrometer [34]. The gamma ray spectrometer is used for detecting iron, magnesium, titanium, thorium and potassium. The X-ray fluorescence experiment investigated the aluminum, silicon and magnesium concentrations while the α -particle spectrometer measured radiation. The footprint for the Apollo 15 instruments was large and thus often overlapped adjacent geologic units impeding specific compositional analyses. However, when combined with other ground-based observations and the recent Clementine data they are very useful. The Apollo 15 data revealed an apparent depressed thermal neutron flux which has been attributed to high concentrations of KREEP and thorium. KREEP and thorium are thought to be associated with the Aristarchus crater and ejecta [36] and may provide an additional resource.

McCord et al. [34] reported that the values of iron, magnesium and titanium for the Aristarchus region are all above the Apollo 15 average (see Table 1) and the percentage of titanium present at Aristarchus (2.2%) is higher than in the mare materials to the west (2%) and in Mare Imbrium to the east (1.4%). These values led [33] to suggest that the titanium content in the mare and Plateau mantling materials may be even larger than indicated if ejecta from Aristarchus is low in titanium and thereby dilutes or masks the titanium concentration in those materials. Further, [33] suggested that the Aristarchus mantling materials are very similar to the high titanium orange glass present and collected at Taurus Littrow by the Apollo 17 astronauts. The X-ray fluorescence experiment obtained an Al/Si ratio of 0.3 ± 0.04 for a region north of Schröter's valley which is very similar to the returned lunar KREEP samples and mare materials at an average of about 0.39. Highlands materials on the other hand are much higher at around 0.54 [38, 39].

TABLE 1: Orbital Geochemical Results*

	Area	Fe(%)	Mg(%)	Ti(%)	Th (ppm)	K(ppm)
Aristarchus	39°W - 54°W ~17°N - 30°N	13.6	6.2	1.4	5.8	1700
Oceanus Procellarum	54°W - 81°W ~10°N - 30°W	9.6	4.9	2.2	6.9	2500
Mare Imbrium	15°W - 39°W ~22°N - 30°N	10.5	4.6	2.0	3.9	1700
Average Apollo 15	-	8.7	4.8	1.45	2.2	1230

*[after 33]

Ground-based radar

A radar survey of the Aristarchus Plateau region was completed by [33 and 40]. Dual polarization 3.8 cm maps for the Moon were acquired by Zisk et al. [33] with a spatial resolution of about 2 km. The most recent 70-cm maps of the Moon were acquired by Thompson [40] at a spatial resolution of about 3 km. Both of these radar image data sets were examined to provide additional information concerning the surface roughness, distribution, and thickness of the pyroclastic deposits. Their studies confirmed the lack of surface signal scatterers in the 1-50 cm size region over much of the plateau. This scarcity of surface signal scatterers is evidenced by the dark radar returns, or darker regions in the images. Figure 4 illustrates the dark radar return from the Aristarchus Plateau and other regional pyroclastic deposits such as Rima Bode. The bright patches represent areas with high surface scatter, or large blocks of rock and lighter, more reflective materials. In addition, the high dielectric losses denoted by the low return suggest the presence of excess Fe and/or Ti.

Radar backscatter echoes are influenced by a combination of surface or subsurface roughness and the bulk dielectric properties of the target materials. For lunar observations, a circularly polarized energy wave is transmitted, and both senses of circular polarization are received. The echo with polarization orthogonal to that transmitted is referred to as polarized, since it corresponds to the return expected from a flat reflecting plate. The echo with polarization identical to that transmitted is referred to as depolarized. The polarized echo is assumed to be the sum of a quasispecular component, due to scattering from facets large with respect to the radar wavelength, and a diffuse return or multiple scattering among wavelength scale objects, either on the target surface or within perhaps 100 radar wavelengths of the surface. The depolarized return is dominated by the diffuse echo. At low angles of incidence (near to nadir viewing geometry), the quasispecular echo will dominate the polarized return, and is very sensitive to tonal changes in regional slope or roughness on horizontal scales of 10-100 m.

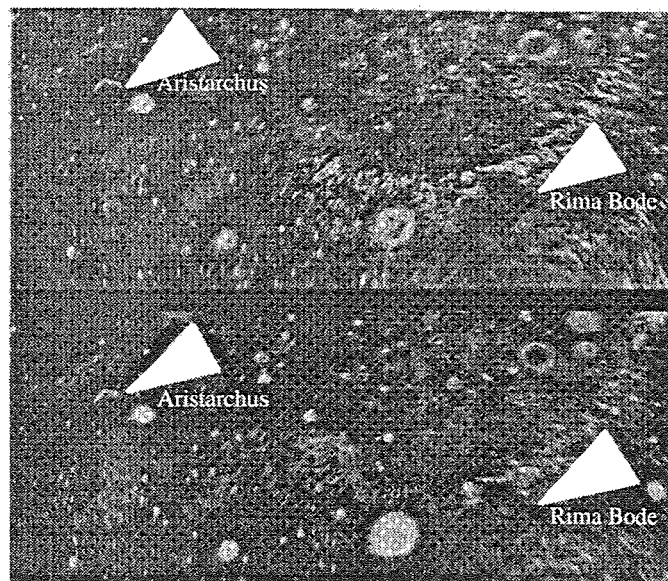


Figure 5: 70-cm radar images of the Aristarchus Plateau and Rima Bode regions (arrows). (a) polarized (b) depolarized. FOV = 2.6°-35.0°N, 62.5°W - 11.4°E.

Spudis and Davis [28] demonstrated that the Aristarchus regional pyroclastic deposit is deeper than the Rima Bode deposit based on the 70-cm radar returns. Results of early analyses indicate that the greatly attenuated polarized and depolarized returns from the Aristarchus Plateau imply a smooth-surfaced, fine grained, highly lossy mantling deposit [33, 40]. The incident 70-cm radar energy is assumed to penetrate the loose pyroclastic debris, traverse the voids within the deposit, and return from the interface between the highlands regolith and mantle [28]. Zisk et al. [33] proposed a

mantle depth of 5-20 m for the Aristarchus Plateau. More recently, McEwen et al. [27] suggested a mantle depth of between 10-30 m based on crater penetration depth/diameter ratios.

Eclipse temperature maps can be generated from infrared observations of the lunar surface. These data and resultant maps can be used to identify lunar surface units with distinct thermal properties. Varying rock surfaces such as large blocky boulders have a different signature than the finer grained regolith fraction. Infrared eclipse temperatures have been measured in the 11 μm band with resolutions of 10-15 km [41, 42]. Once totally eclipsed, significant temperature differences are present between points on the surface. These differences are related to a variety of variables including, albedo, slope, solar illumination, eclipse geometry, and initial temperature of the full moon. The main driving factor in the temperature differentials are due to thermo-physical parameters such as rock/grain size and distribution as well as the thermal inertia of the material [31, 41].

At full moon, the lunar surface brightness temperatures are affected and controlled by two dominant factors, insulation and surface albedo. As with a light sandy beach, directly illuminated areas are warm and those surfaces in shadow or pointing away from the sun are relatively cool. Similarly, the dark mare will tend to be warmer than the lighter highlands, as a black-top road becomes hotter than a lighter concrete road surface. During times of eclipse, planetary surface temperatures cool rapidly except where high-conductivity paths trap heat in a 'sink', or a large, exposed rock.

The Aristarchus plateau IR-eclipse temperatures fell below those for similarly low albedo areas elsewhere on the surface. [31] reports the Aristarchus Plateau several degrees cooler than adjacent areas, setting it apart from other low albedo areas. This low return can only be attributed to the lack of large blocks of rock (>10 cm; [40]).

GEOLOGY OF ARISTARCHUS

The dark mantle material present in the Aristarchus area is superposed on pre-Imbrian and Imbrian materials. The pyroclastic deposit covers 37,400 km². The mare materials present in the vicinity of the Plateau are thought to be part of the Harbinger formation [44]. The pyroclastic deposits are of Eratosthenian and Copernican age (Figure 4).

Domes present just north of Schröter's Valley are thought to be volcanic. Image analysis for this study and previous maps (e.g., 44, 45) indicate the presence of probable source craters atop several of the domes. Craters Herodotus D and Aristarchus R (see map) are flanked by lava flows and smooth dark mantle material. Additionally, Schröter's Valley and the small parasitic rille on the interior floor are Copernican in age.

Mare materials once embayed the highlands material present on the surface of the Aristarchus region. Constructive volcanism began in the region forming the plateau and volcanic domes through the Copernican Era. Lava flows were accompanied by sporadic explosive eruptions in many different locations around the plateau. This activity was accompanied by tectonic uplifting and rifting along the north and northwestern edge of the plateau giving rise to its 1° westward downslope and 100 m rise above the adjacent western boundary with Oceanus Procellarum. Perhaps spawned by the Aristarchus impact event, Cobra Head formed in association with explosive volcanic eruptions that mantled the plateau.

The Aristarchus plateau is an uplifted region extending north-northwest of the craters Aristarchus and Herodotus. Recent Clementine altimetry data show the northwest edge of the plateau sitting nearly 100 m above the adjacent mare terrain in Oceanus Procellarum. The plateau is covered with a relatively thick blanket of pyroclastic (fire-fountain) material that most likely emanated from Cobra Head and other smaller vents nearby. The largest and most conspicuous volcanic source crater on the lunar surface. It is believed to be the source for Schröter's Valley. Aristarchus crater

Figure 4: Simplified Geologic Map of the Aristarchus Region

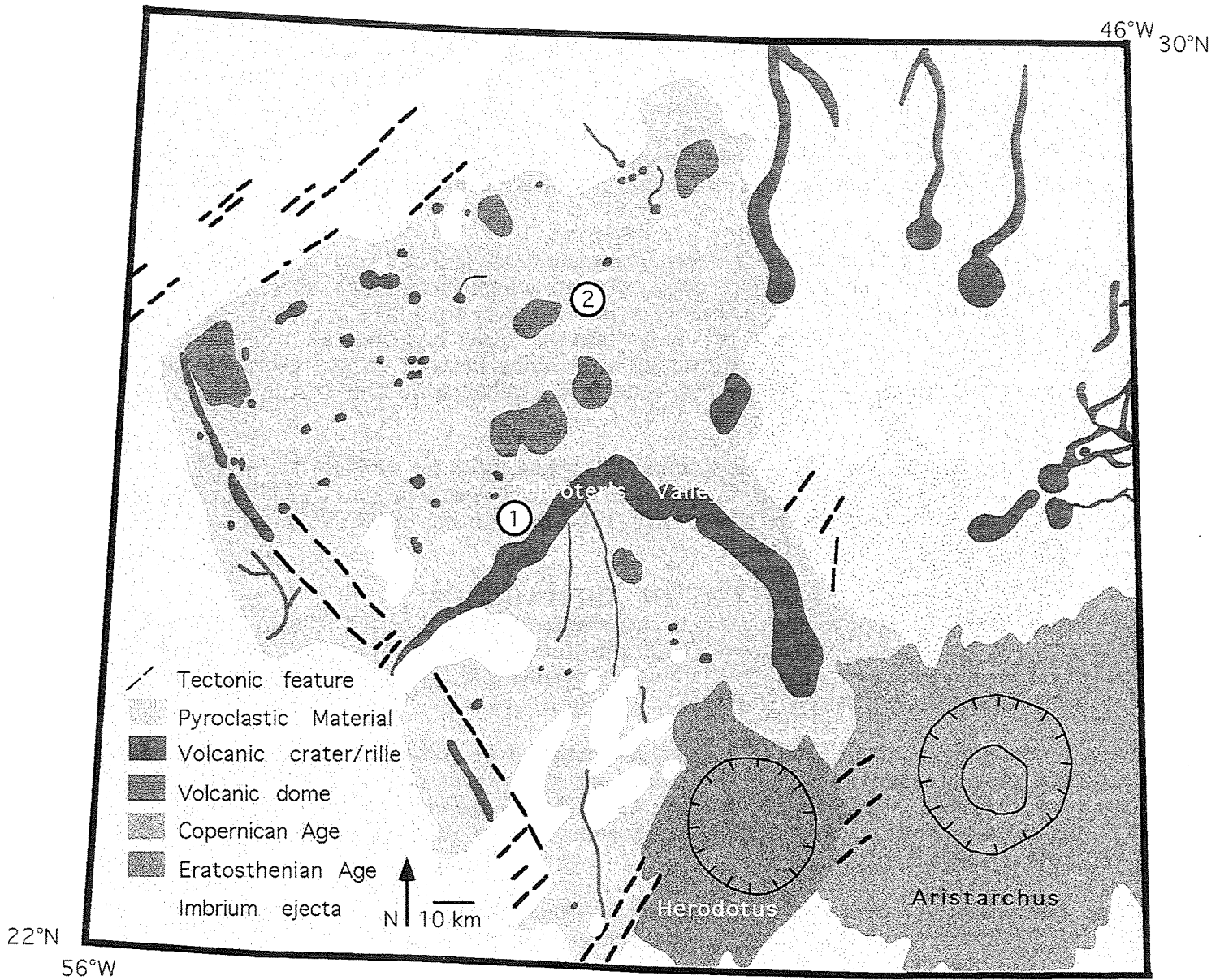


Figure 4: Simplified geologic map of the Aristarchus Plateau region. Note relationship and distribution of volcanic vents, domes and rilles on the plateau.

is a Copernican aged impact crater (40 km diameter) which should expose both Imbrian ejecta and pre-Imbrian material. Herodotus crater is a flooded, Imbrian-aged impact crater (35 km diameter) located just west of Aristarchus. The floor of Oceanus Procellarum is Eratosthenian in age. This mare deposit lies adjacent to the western edge of the Aristarchus plateau. Spectrally, this unit is a very 'blue', low albedo unit in contrast to the bright 'red' spectral nature of the Aristarchus Plateau.

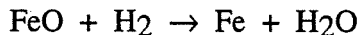
RESOURCE POTENTIAL

These two candidate sites are particularly well suited for in-situ resource generation and utilization based on their spectral signatures and depth of material. In-situ resources are resources existing in the environment, in the atmosphere or at the surface of a planet or satellite. To date, humans venturing into space have relied almost exclusively on equipment and supplies carried from Earth. This strategy is certainly appropriate for operations in Earth orbit, or for stays of a few days on the surface of the Moon. However, the ability to effectively utilize local resources, to "live off the land," will prove vital for long term human habitation of the Moon and planets.

Some resources, *i.e.* solar energy for power and the martian atmosphere for aerobraking, will be exploited by the next generation of robotic spacecraft. Other resources, such as use of the local soil for radiation shielding, will be important to support a long-term human presence. Still others, notably export of helium-3 for fusion reactors on Earth, may only become feasible in the distant future.

Extraction of lunar oxygen for rocket propulsion is a key example of in-situ resource utilization which will directly support a long-term human presence on the Moon. This is because one of the largest elements in any rocket is the oxygen required to burn the fuel. Nearly 90% of the propellant mass of a liquid hydrogen-liquid oxygen rocket is oxygen. Locally-produced oxygen for rocket propulsion promises by far the greatest cost and mass saving of any in-situ lunar resource [46].

Over twenty different processes have been proposed for oxygen production on the Moon [47]. One of the simplest and best-studied of these processes involves the subsolidus reduction of ferrous iron (Fe^{2+}) in lunar minerals and glass using hydrogen gas. This method of oxygen production is a two-step process. Ferrous iron (as FeO) is first reduced to metal, and oxygen is liberated to form water:



The water is then electrolyzed as a second step, with hydrogen recycled to the reactor and oxygen liquefied and stored.

Recent experiments on lunar materials and terrestrial analogs allow an assessment of the various proposed feedstocks for lunar oxygen production. Materials which have been proposed and/or tested include ilmenite, basalt, soil and volcanic glass. As the following discussion illustrates, some reacted better than others.

Ilmenite

Most previous work on lunar resources has focused on ilmenite (FeTiO_3) as the feedstock for oxygen production [48]. Ilmenite occurs in abundances above 25 wt% in some lunar rocks. This mineral is easily reduced, and oxygen yields of 8-10 wt% may be achievable. However, experiments to date have invariably failed to completely segregate ilmenite from other mineral fragments, so that stoichiometric oxygen yield has not been realized.

Lunar oxygen production scenarios which rely exclusively on ilmenite require processing to separate the mineral. This is done to minimize the amount of material that must be heated in order to release oxygen. Processing of soil includes sizing and magnetic separation. Processing of rock requires an initial crushing step. Thus, use of ilmenite alone for lunar oxygen production will involve high energy investments for feedstock preparation.

Basalt

The first experiments to extract oxygen from lunar material utilized high-titanium basalt 70035 [49]. This sample, with an initial iron content of 14.35 wt%, produced from 3.2 to 4.6 wt% oxygen in hydrogen reduction experiments run at temperatures of 900-1050°C.

Soil

Oxygen can be produced from a wide range of unprocessed lunar soils [50,51]. Iron-poor highland soils yield the smallest amounts of oxygen, 1-2 wt%. Mare soils, especially iron-rich samples, produce as much as 3.6 wt% oxygen. The dominant Fe-bearing phases in lunar soil are the minerals ilmenite, olivine, pyroxene and impact glass. Each of these phases is a source of oxygen.

Oxygen yield for lunar soils is strongly correlated with initial iron content [50,51]. Therefore it is possible to assess the potential for oxygen production at any location on the Moon for which the soil's Fe concentration is known. On a global scale, iron abundances in the near surface has been estimated from data returned by spacecraft. Iron was one of several elements measured from orbit during the Apollo 15 and 16 missions, using gamma ray spectrometry [52]. These data cover approximately 20% of the lunar surface, with spatial resolutions of around 100 km.

An improved gamma ray spectrometer is manifested on the Lunar Prospector mission, selected for flight in NASA's Discovery program [53]. This spacecraft, to be placed in a polar orbit, will provide geochemical data for the entire lunar surface. The spectrometer's spatial resolution will again be approximately 100 km.

A technique for iron assessment based on orbital multispectral imaging has recently been developed [54]. This method correlates iron abundance to a parameter derived from reflectance values at 750 and 900 nm. The authors use data from the Clementine spacecraft to map iron abundances across nearly the entire lunar surface. The spatial resolution of the initial study is 35 km. Clementine data, however, can support identification of iron-rich regions as small as a few hundred meters across at any location on the Moon.

Volcanic Glass

The optimum feedstock for production of lunar oxygen and other volatiles may be volcanic glass [26]. At least 25 distinct glass compositions have been identified in the Apollo sample collection [55]. The iron- and titanium-rich species, represented by the isochemical black and orange glasses from the Apollo 17 landing site, have demonstrated the highest oxygen yields of any lunar sample, approaching 4.5 wt% [50,51]. These samples are uniformly fine-grained, offering a feedstock which reacts rapidly and can be used with little or no processing prior to oxygen extraction.

Extensive areas of the lunar surface covered by volcanic glass have been delineated using Earth-based data and Apollo orbital photography [23]. Clementine multispectral imagery has recently been employed to determine the precise extent and estimate the thickness of one widespread deposit, that of the Aristarchus plateau [27].

POTENTIAL LANDING SITE(S)

Two potential landing sites were selected based on analysis of the early Apollo data and the more recent Clementine data. The pyroclastic sites were identified based on their low albedos, dark radar return signatures, and association with what appears to be volcanic vents and in some cases sinuous lava channels. Table 2 summarizes the features present within (1) 10 km radius and (2) 100 km radius of the two potential sites. See Figures 1 and/or 4 for locations.

Table 2: Candidate Landing Sites on Aristarchus Plateau

Site	Features within 10 km radius	Features within 100 km radius
Site 1 25° 25' N 52° 20' W	<p><i>Location/Site Description:</i> North rim of Schröter's Valley</p> <ul style="list-style-type: none"> - low albedo - low radar return <p>Pyroclastic material covers entire area</p> <ul style="list-style-type: none"> - vents present - local area estimate of deposit ~170km² - potential volume ~1700 - 5100 km³ - largest crater ~5 km diameter - access to Schröter's Valley - hummocky area, underlain by Imbrian ejecta <p><i>Characteristic Features Present:</i></p> <ul style="list-style-type: none"> - crater chains present - good view across Schröter's Valley for stratigraphic assessment and view of parasitic rille on floor of Schröter's Valley - very near volcanic dome material 	<p><i>Location/Site Description:</i> Same as for 10 km and,</p> <p><i>Characteristic Features Present:</i> Access to mare material in Oceanus Procellarum</p> <ul style="list-style-type: none"> - hummocky terrain - access to northern domes
Site 2 27° 50' N 51° 20' W	<p><i>Location/Site Description:</i> East of Herodotus X</p> <ul style="list-style-type: none"> - very low albedo - very low radar return - local area estimate of deposit >800km² - potential volume ~4000 - 24000 km³ <p><i>Characteristic Features: Present</i></p> <ul style="list-style-type: none"> - access to Herodotus X - probable pyroclastic source vents - access to small rille for stratigraphic analysis - several crater chains present , mantled with pyroclastic materials - relatively fresh craters with prominent rims (<100 m dia.) 	<p><i>Location/Site Description:</i> Same as for 10 km</p> <p><i>Characteristic Features: Present:</i></p> <ul style="list-style-type: none"> - access to Harbinger Mountains and other structural features to the north - access to probable volcanic vent chain and ridges - access to more rilles for stratigraphic analysis

REFERENCES

- [1] NASA Strategic Plan, 1996
- [2] HEDS Strategic Plan, 1996
- [3] Zisk S.H., C.A. Hodges, H.J. Moore, R.W. Shorthill, T.W. Thompson, E.A. Whitaker, and D.E. Wilhelms, "The Aristarchus-Harbinger Region of the Moon: Surface Geology and History from Recent Remote-Sensing Observations", *The Moon*, 17, p. 59-99, 1977.
- [4] Coombs C.R. and Hawke B.R., "Lunar pyroclastic deposits". GSA Abstracts with Program, p. 237, 1988.
- [5] Hawke B.R., C.R. Coombs, L.R. Gaddis, P.G. Lucey, and P.D. Owensby, "Remote sensing and geologic studies of localized dark mantle deposits on the Moon", *Proc. Lunar Planet. Sci. Conf. 19th*, pp. 255-268, 1989.
- [6] Kulcinski G.L., J.F. Santarius and L.J. Wittenberg. "Presentation at the 1st Lunar Development Symposium, 1986.
- [7] Kulcinski G.L. ed. "Astrofuel for the 21st Century. "College of Engineering, Univ. of Wisconsin, Madison, 20 pp.
- [8] Gibson M.A. and C.W. Knudsen, " Lunar oxygen production from ilmenite", In *Lunar Bases and Space Activities of the 21st Century*, W.W. Mendell, ed., pp. 543-550, 1985.
- [9] Simon M.C., "A parametric analysis of lunar oxygen production", In *Lunar Bases and Space Activities of the 21st Century*, W.W. Mendell, ed., pp. 531-541, 1985.
- [10] Pohn and Wildey, "Color Difference Albedo Map of the Moon", 1970.
- [11] Cavaretta G., R. Funiceileo, H. Giles, G.D. Nichols, A. Taddeucci, J. Zussman, " Geochemistry of green glass spheres from Apollo 15", In *The Apollo 15 Lunar Samples*, Lunar Science Institute, pp. 202-203, 1972.
- [12] Quaide W. , "Provenance of Apennine Front regolith materials (abstract). In *Lunar Science IV*, Lunar and Planetary Institute, pp. 606-607.1973.
- [13] Carr M.H. and C.E. Meyer, "Chemical and petrographic characteristics of the regolith at the Apollo 15 landing site. In *The Apollo 15 Samples*, Lunar Science Institute, pp. 48-50, 1972.
- [14] Hussain L, "The Ar-Ar and cosmic ray exposure ages of Apollo 15 crystalline rocks, breccias and glasses", In *The Apollo 15 Lunar Samples*, Lunar Science Institute, pp. 374-376, 1972.
- [15] Roedder E. and P. Weiblen, "Origin of orange glass spherules in Apollo 17 sample 74220, *EOS Trans. Amer. Geophys. Union*, 54, pp. 612-613, 1973.
- [16] McKay D.S. and G. Heiken, 1973.
- [17] McKay D.S., U.S. Clanton, and G. Ladle, " Scanning electron microscope study of Apollo 15 green glass", *Proc. 4th Lunar Sci. Conf.*, pp. 225-238, 1973.

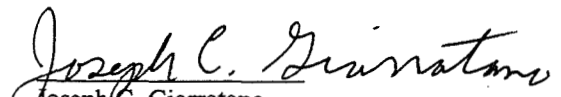
- [18] Huneke J.C., F.A. Podeseck, and G.J. Wasserberg, "An argon bouillabaisse including ages from the Luna 20 site", in Luna Science IV, Lunar Science Institute, pp. 403-405, 1973.
- [19] Carter J.L., E. Padovani, H.C. Taylor, "Morphology and chemistry of particles from Apollo 17 soils 74220, 74241 and 74801", EOS Trans Amer. Geophys. Union, 54, 582-584, 1973.
- [20] Reid A.M., J.L. Warner, W.I. Ridley, R.W. Brown, and G. Moreland, "Apollo 17 orange glass, Apollo 15 green glass and Hawaiian lava fountain glass, EOS Trans. Amer. Geophys. Union, 54, pp. 606-607, 1973.
- [21] Heiken G.H. and D. McKay, Abstracts and Program, Geol. Soc. of America Ann. Meeting, 1974.
- [22] Wilson L. and J. Head, "Ascent and eruption of basaltic volcanism on the Earth and Moon", J. Geophys. Res., 78, 2971-3001, 1981.
- [23] Gaddis L.R., C.R. Pieters, B.R. Hawke, "Remote sensing of lunar pyroclastic mantling deposits", Icarus, 61, 461-489, 1985.
- [24] Coombs C.R., "Explosive Volcanism on the Moon and the Origin of Lunar Sinuous Rilles and their Terrestrial Counterparts", Ph.D. Dissertation, U. Hawaii, 256 p., 1989.
- [25] Hawke B.R., Coombs C.R., Gaddis L.R., Lucey P.D., Owensby P.D., "Remote sensing and geologic studies of localized dark mantle deposits on the Moon." Proc. 19th Lunar and Planetary Sci. Conf., pp. 255-268, 1989.
- [26] Hawke B.R., Coombs C.R. and Clark B.E. "Pyroclastic deposits: An ideal lunar resource", Proc. 20th Lunar and Planetary Sc. Conf., pp. 249-258, 1990.
- [27] McEwen A.S., M.S. Robinson, E.M. Eliason, P.G. Lucey, T.C. Duxbury, P.D. Spudis, "Clementine Observations of the Aristarchus Region of the Moon", Science, v. 266, pp. 1858-1861, 1994.
- [28] Spudis P.D. and P. Davis, Lunar and Planetary Science Conf., 1991.
- [29] Davis P. and P.D. Spudis, "Global petrologic variations on the moon: A ternary-diagram approach, Proc. 17th Lunar Planet. Sci. Conf., in J. Geophys. Res., 92, 1987.
- [30] Hawke B.R., C.R. Coombs, B.A. Campbell, P.G. Lucey, C.A. Peterson, S. Zisk, "Remote Sensing of Regional Pyroclastic Deposits on the North Central Portion of the Lunar Nearside", Proc. 21st Lunar and Planetary Sci., pp. 377-389, 1991.
- [31] Pieters CM, T.B. McCord, S.H. Zisk, and J.B. Adams, "Lunar black spots and the nature of the Apollo 17 area", J. Geophys. Res., 78, pp. 5867-5875, 1973.
- [32] Lucey P.G., B.R. Hawke, C.M. Pieters, J.W. Head, and T.B. McCord, "A compositional study of the Aristarchus region of the Moon using near-infrared reflectance spectroscopy", Proc. 16th Lunar and Planetary Sci. Conf., pp. D344-D354, 1986.
- [33] Zisk S.H., C.A. Hodges, H.J. Moore, R.W. Shorthill, T.W. Thompson, E.A. Whitaker, D.E. Wilhelms, "The Aristarchus-Harbinger region of the Moon: Surface geology and history from recent remote sensing observations", The Moon, 17, pp. 59-99, 1977.

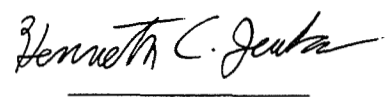
- [34] McCord T.B., R.N. Clark, B.R. Hawke, L.A. McFadden, P.D. Owensby, C. M. Pieters, and J.B. Adams, "Moon: Near-infrared spectral black spots and the nature of the Apollo 17 landing area", *J. Geophys. Res.*, 78, pp. 5867-5875, 1981.
- [35] Davies D.W., T.V. Johnson, and D.L. Matson, "Lunar multispectral mapping at 2.26 microns: First results", *Proc. 10th Lunar and Planetary Science Conf.*, pp. 1819-1828, 1979.
- [36] Johnson T.V., J.A. Mosher, and D.L. Matson, "Lunar spectral units: A northern hemispheric mosaic", *Proc. 8th Lunar and Planet. Sci. Conf.*, pp. 1013-1028, 1977.
- [37] Metzger A.E., J.I. Trombka, R.C. Reedy, J.R. Arnold, "Element concentrations from Lunar Orbital Gamma-Ray Measurements", *Proc. 5th Lunar and Planetary Science Conf. Suppl. 5, Geochim. Cosmochim. Acta 2*, pp. 1067-1078, 1074.
- [38] Adler I, J. Trombka, J. Gerard, P. Lowmann, R. Schmadebeck, A. Blodgett, E. Eller, L. Yin, P. Gorenstein, and Bjorkholm, "Apollo 15 Geochemical X-ray Fluorescence Experiment: Preliminary Report", *Science*, pp. 436-440, 1972.
- [39] Malin M.C., "Lunar red spots: Possible pre-mare Materials", *Earth Planet. Sci. Letters*, 21, pp. 331-341, 1974.
- [40] Thompson T.W., "High resolution lunar radar map at 70-cm wavelength", *Earth Moon Planets*, 37, pp. 59-70, 1987.
- [41] Shorthill R.W. and J.M. Saari, "Non-uniform cooling of the eclipsed moon: A list of thirty prominent anomalies", *Science*, 50, pp. 210-12 1965;
- [42] Shorthill R.W., "The Infrared Moon: A Review", In Lucas, ed., "Thermal Characteristics of the Moon", *Progress in Astronautics and Aeronautics*, 28, 3-49, MIT Press. 1972.
- [43] Shorthill R.W., "Infrared Atlas Charts of the Eclipsed Moon", *The Moon*, 7, 22-45, 1973.
- [44] Moore H.J., "Geologic Map of the Seleucus Quadrangle of the Moon", U.S. Geol. Survey, Geol. Inv. Map I-527, 1967.
- [45] Moore H.J., "Geologic Map of the Aristarchus Quadrangle of the Moon", U.S. Geol. Survey, Geol. Inv. Map I-465, 1965.
- [46] Joosten, B. K., and L. A. Guerra, "Early lunar resource utilization: A key to lunar exploration", *AIAA Space Programs and Technol. Conf. Paper 93-4784*, American Institute of Aeronautics and Astronautics, Washington, D. C., 1993.
- [47] Taylor, L. A., and W. D. Carrier III, "The feasibility of processes for the production of oxygen on the Moon", in *Engineering, Construction and Operations in Space III*, pp. 752-762, American Society of Civil Engineers, New York, 1992.
- [48] Chambers, J. G., L. A. Taylor, A. Patchen, and D. S. McKay, "Quantitative mineralogical characterization of lunar high- Ti mare basalts and soils for oxygen production", *Journal of Geophysical Research*, 100,14,391-14,401, 1995.

- [49] Gibson, M. A., C. W. Knudsen, D. J. Brueneman, C. C. Allen, H. Kanamori, and D. S. McKay, "Reduction of lunar basalt 70035: Oxygen yield and reaction product analysis", *Journal of Geophysical Research*, 99, 10,887-10,897, 1994.
- [50] Allen, C. C., R. V. Morris, and D. S. McKay, "Experimental reduction of lunar mare soil and volcanic glass", *Journal of Geophysical Research*, 99, 23,173 - 23,195, 1994.
- [51] Allen, C. C., R. V. Morris, and D. S. McKay, "Oxygen extraction from lunar soils and pyroclastic glass", submitted to *Journal of Geophysical Research*, 1996.
- [52] Davis, P. A. Jr., "Iron and titanium distribution on the Moon from orbital gamma ray spectrometry with implications for crustal evolutionary models", *Journal of Geophysical Research*, 85, 3209-3224, 1980.
- [53] Feldman, W. C., A. B. Binder, G. S. Hubbard, R. E. Murray Jr., M. C. Miller, and T. H. Prettyman, "The Lunar Prospector gamma-ray spectrometer", *Lunar and Planetary Science XXVII*, 355-356, 1996.
- [54] Lucey, P. G., G. J. Taylor, and E. Malaret, "Abundance and distribution of iron on the Moon", *Science*, 268, 1150-1153, 1995.
- [55] Delano J., "Pristine lunar glasses: Criteria, data and implications", Proc. 16th Lunar Planet. Sci. Conf., Part 2, J. Geophys. Res., 91, D201-213, 1986.

59-80
038290
294267
14P.

INHERIT SPACE
Joseph C. Giarratano, Ph.D.
University of Houston Clear Lake
JSC Mail Code BT2
August 8, 1996
Kenneth C. Jenks
Information Technology Office
Information Systems Division
Business and Information Systems Directorate


Joseph C. Giarratano


Kenneth C. Jenks

INHERIT SPACE

Final Report
NASA/ASEE Summer Faculty Program-1996
Johnson Space Center

Prepared by:	Joseph C. Giarratano, Ph.D.
Academic Rank:	Associate Professor of Computer Science
University and Department:	University of Houston Clear Lake Computer Science Dept. 2700 Bay Area Blvd. Houston, TX 77058
NASA/JSC	
Directorate:	Business and Information Systems
Division:	Information Systems
Branch:	Information Technology
JSC Colleague:	Kenneth C. Jenks
Date Submitted:	August 8, 1996
Contract Number:	NAG 9-867

ABSTRACT

The objective of the proposed research was to begin development of a unique educational tool targeted at educating and inspiring young people 12-16 years old about NASA and the Space Program. Since these young people are the future engineers, scientists and space pioneers, the nurturing of their enthusiasm and interest is of critical importance to the Nation.

This summer the basic infrastructure of the tool was developed in the context of an educational game paradigm. The game paradigm has achieved remarkable success in maintaining the interest of young people in a self-paced, student-directed learning environment. This type of environment encourages student exploration and curiosity which are exactly the traits that future space pioneers need to develop to prepare for the unexpected.

The Inherit Space Educational Tool is an open-ended learning environment consisting of a finite-state machine classic adventure game paradigm. As the young person explores this world, different obstacles must be overcome. Rewards will be offered such as using the Flight Simulator to fly around and explore Titan. This simulator was modeled on conventional Earth flight simulators but has been considerably enhanced to add texture mapping of Titan's atmosphere utilizing the latest information from the NASA Galileo Space Probe. Additional scenery was added to provide color VGA graphics of a futuristic research station on Titan as well as an interesting story to keep the youngster's attention.

This summer the game infrastructure has been developed as well as the Titan Flight Simulator. A number of other enhancements are planned.

INTRODUCTION

Significance of Project

In addition to its primary mission of Space Research, NASA has a number of other goals such as Technology Transfer and educating the public about Space. The education of our Nation's youth is particularly important fewer young people are going into science and engineering, yet these disciplines are the foundations of the Space Program. Besides education, there is a critical need to *inspire* the public about the Space Program to keep the dream alive of expanding beyond the boundaries of Earth.

To carry out this mission of educating and inspiring youth about Space and NASA, the strategy chosen was to develop a game called *Inherit Space* targeted at 12-16 year olds. The game paradigm was selected to make the educational component about living in Space interesting while also being fun to play.

The game design is based on popular adventure games in which the user has a goal and must overcome a number of obstacles. The user must explore new environments and challenges in *Inherit Space*, thus mirroring the challenges faced in Space Exploration. The great advantage of an adventure game is that it allows the user an open-ended exploration of the environment rather than the linear design of a comic book. The disadvantage of an adventure game is that it requires a great deal of programming and creativity on the part of the designers.

Statement of Project

The initial tasks undertaken this summer were to

- Create the infrastructure of a multimedia adventure game involving graphics, video, and sound.
- Implement a basic exploration scenario involving multiple rooms and obstacles
- Implement a flight simulator for Titan, a moon of Saturn.

In order to make it convenient for the target audience of 12-16 year olds to use the game, a graphical user interface (GUI) was designed and implemented to provide seamless transitions between the adventure game and application programs such as the Flight Simulator. The GUI is designed for Windows and Mouse support, and a joystick for operation of the Flight Simulator. Graphic images of the different rooms are shown the user and a musical score is played which changes depending on the room the user is in.

METHODOLOGY

In order to expedite the software development, commercial off the shelf software was used whenever possible (Michael Radke and Chris Lampton, *Build Your Own Flight Sim in C++*). However this was still not trivial as the original flight simulator is 6,000 lines of C++ code which required substantial modification for Titan. In particular the background scenery was modified from the simple blue sky of Earth to provide colors and texture mapping for realistic views of the Titanian atmosphere based on data from the NASA Galileo Space Probe. In addition, the scenery had to be altered to display buildings and other objects of the game plot.

Initially Java was tried as the development language. However since Java does not support video clips which are planned for the game, and is also too slow for real-time response, it was decided to switch to an alternative development tool called Delphi.

IMPLEMENTATION

Finite-State Machine Adventure Game

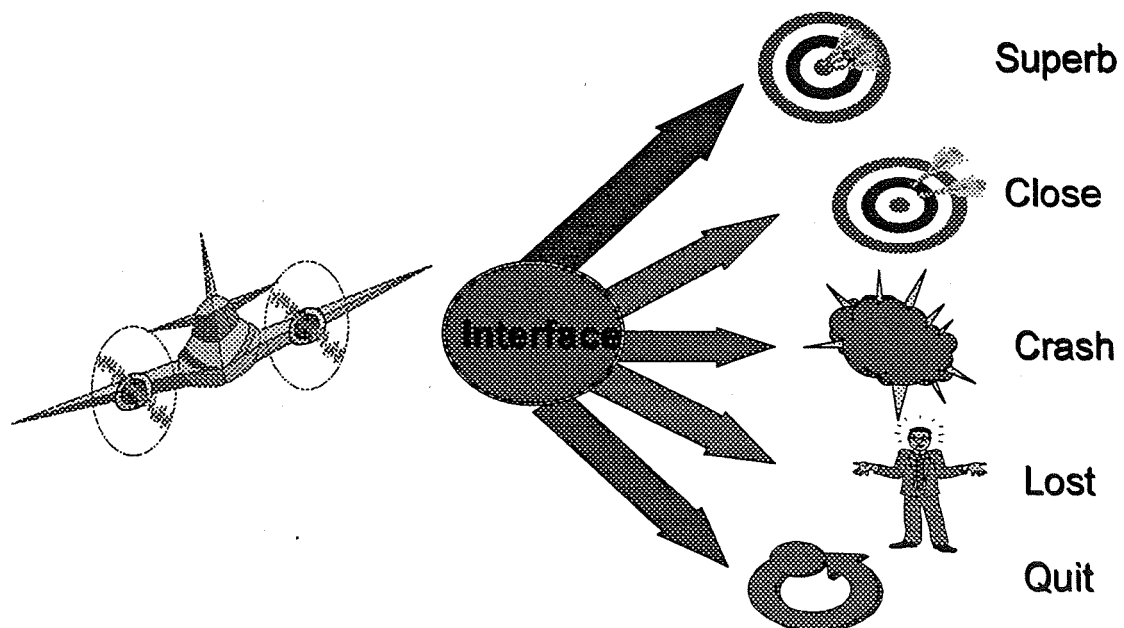
A finite-state machine was implemented using Delphi for the adventure game infrastructure. The finite-state machine is straightforward to implement easily extensible as further rooms are added to the game. It is also very easy to call other code such as the flight simulator depending on the state of the finite-state machine, i.e., what room the user is in.

Graphic images are shown to the user and mouse-sensitive buttons are displayed to allow the user to explore other rooms or take other actions. This feature is particularly convenient for the 12-16 year olds as it minimizes typing of input. It also keeps up the pace of the game rather than slowing down while the user types input.

Flight Simulator

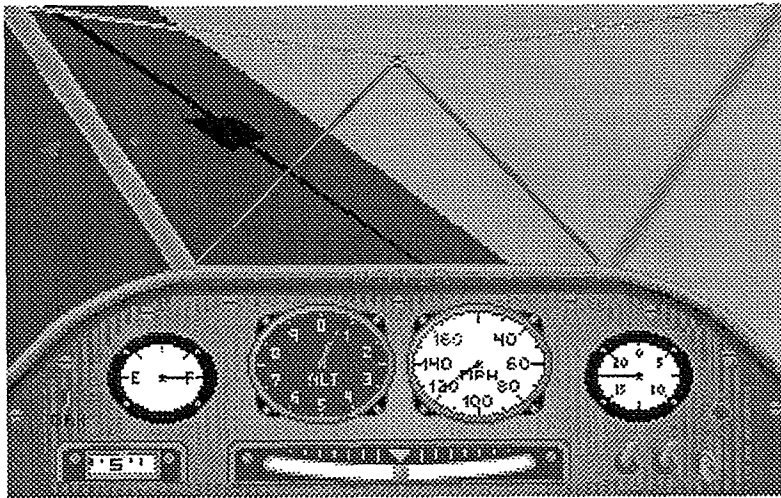
The Flight Simulator is game designed to be called from the main adventure game. This game within a game is called a *gamelet*. The Flight Simulator is designed as a fun educational component. It teaches the user what conditions on Titan are like through flying over the surface and various instrument readouts. There is a good deal of skill required by the user for successful flying. Even if the user has experience with Earth simulators, the Titan Flight Simulator is substantially different and challenging. The following modifications to the original flight simulator were implemented.

- Initialize flight in the air to match the game plot
- Improve flying controls for Titan
- Customize scenery for Titan
- Provide interface with adventure game GUI

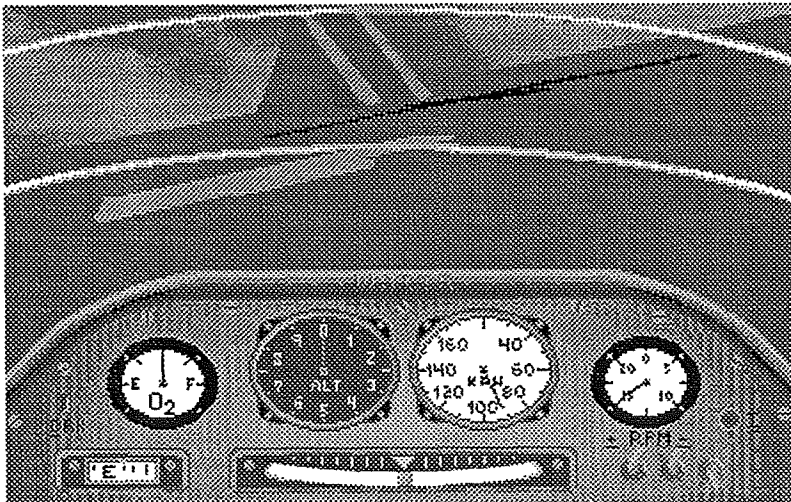


A number of 3-D interactive game programming techniques and algorithms were required to properly implement the Flight Simulator:

- Object representation
- Keyboard, mouse, and joystick input
- Flight modeling
- VGA color system, texture and color mapping
- Viewing transformations
- Integrate with the main program
- Flight Initialization in mid-air required proper initialization of the State Vector
- Improved Flight Controls since the original code provided poor flight control
- Sensitivity Variable to provide the same flying characteristics on different machines
- Real-time Timer



Before Modification



After Modification

3D VIEW PROCESSING

In addition, a considerable amount of effort was needed to provide realistic 3D modeling of the graphics showing Titan that involved view processing. The following factors were affected.

- Multiple coordinate system transformations
- Polygon sorting
- Hidden surface removal
- Polygon clipping
- Pixel color assignment
- VGA Master Palette
- The horizon
- Dynamic sky and ground
- Different approach needed for 3-D texturing of sky and ground
- Texturing not supported by existing object classes and algorithms
- Bitmaps and the master color palette required modification
- Improving the Scenery
- Scenery Objects - World File
- Objects
- Polygons
 - Vertices
 - Color
- Location
- World Coordinates
- Improving the Scenery

PROBLEMS ENCOUNTERED

Some of the major problems encountered were as follows.

- Determining when an EXE was closed and control returned to launcher program
- Launching flight simulator from the Delphi program
- Delphi executables were too large to fit on a diskette
- Distinguish between DLL and EXE programs
- Change music between modules
- Maintain continuity between modules with same music
- Silence was difficult
- Creating obstacles for the user

CONCLUSIONS

The initial version of game was successfully completed this summer. A number of future improvements are planned. For the Flight Simulator the following enhancements will be done.

- Improve texture mapping for sky and ground.
- Add terrain using fractals.
- Modernize cockpit indicators.
- Improve flight model.
- Add collision detection.
- Add auto-pilot and help.

For the adventure game, a number of additional rooms and gamelets need to be added as the adventure continues. Another feature that will be added is a multimedia Timeline that will show NASA history and technology development from the past to the future involving the game. Multimedia video clips and other educational aids will be used to pique user interest and provide a resource for other games.

APPENDIX-FINITE STATE MACHINE SOFTWARE

```

unit Launch;

interface

uses
  SysUtils, WinTypes, WinProcs, Messages, Classes, Graphics,
  Controls,
  Forms, Dialogs, StdCtrls, ExtCtrls, IniFiles, MPlayer;

type
  TLauncherForm = class(TForm)
    Timer1: TTimer;
    MediaPlayer1: TMediaPlayer;
    procedure FormCreate(Sender: TObject);
    procedure FormDestroy(Sender: TObject);
    procedure Timer1Timer(Sender: TObject);
  private
    { Private declarations }
    Other: Word;
    procedure InitEnvParams;
  public
    { Public declarations }
    EnvParams: TStringList;
  end;

var
  LauncherForm: TLauncherForm;

implementation

{$R *.DFM}
procedure TLauncherForm.InitEnvParams;
var
  p: PChar;
  s: string;
begin
  p:=GetDosEnvironment;
  while p^ <> #0 do begin
    s:=StrPas(p);
    EnvParams.Add(s);
    p:=StrEnd(p)+1;
  end;
end;

procedure TLauncherForm.FormCreate(Sender: TObject);
var
  RoomsIni, StatusIni: TIniFile;
  RtnCode: Integer;
  B : Integer;
  NameOfFirstRoom, OldSong : String;
begin
  RoomsIni :=
  TIniFile.Create('d:\delphi\source\launch\rooms.INI');
  NameOfFirstRoom := RoomsIni.ReadString('rooms',
'first','ERROR');
  OldSong := RoomsIni.ReadString('midi',
NameOfFirstRoom,'ERROR');
  RoomsIni.Free;

  StatusIni :=
  TIniFile.Create('d:\delphi\source\launch\status.INI');
  StatusIni.WriteString('location', 'current', NameOfFirstRoom);
  StatusIni.WriteString('location', 'previous',
NameOfFirstRoom);
  StatusIni.WriteString('location', 'oldsong', OldSong);
  StatusIni.WriteBool('items', 'toothpaste', False);
  StatusIni.WriteBool('items', 'food', False);
  StatusIni.Free;

  MediaPlayer1.FileName := OldSong;
  MediaPlayer1.Open;
  MediaPlayer1.Play;

  EnvParams:=TStringList.Create;
  InitEnvParams;
end;

procedure TLauncherForm.FormDestroy(Sender: TObject);
begin
  EnvParams.Free;
end;

procedure LivingroomForm;
  far; external 'DLiving';

procedure KitchenForm;
  far; external 'DKitchen';

procedure TLauncherForm.Timer1Timer(Sender: TObject);
var
  StatusIni, RoomsIni, MusicIni : TIniFile;
  Oldsong, CurrentLocation, CurrentLocationExe, CurrentSong
  : String;
  cmd: array[0..100] of Char;
begin
  if GetModuleUsage(Other) = 0 then begin
    Timer1.Enabled:=False;

    StatusIni :=
    TIniFile.Create('d:\delphi\source\launch\status.INI');
    CurrentLocation := StatusIni.ReadString('location',
'current','ERROR');
    OldSong := StatusIni.ReadString('location',
'oldsong','ERROR');
    StatusIni.Free;

    if CurrentLocation = 'EXIT' then halt;

    MusicIni :=
    TIniFile.Create('d:\delphi\source\launch\rooms.INI');
    CurrentSong := MusicIni.ReadString('midi',
CurrentLocation,'ERROR');
    MusicIni.Free;

    If OldSong <> CurrentSong then
    begin
      MediaPlayer1.Stop;
      MediaPlayer1.Close;
      IF CurrentSong <> 'ERROR' THEN BEGIN
        MediaPlayer1.FileName := CurrentSong;
        MediaPlayer1.Open;
        MediaPlayer1.Play;
      END;
    end;
  end;
end;

```

```

    StatusIni :=
TIniFile.Create('d:\delphi\source\launch\status.INI');
    StatusIni.WriteString('location', 'oldsong', CurrentSong);
    StatusIni.Free;
end;

RoomsIni :=
TIniFile.Create('d:\delphi\source\launch\rooms.INI');
    CurrentLocationExe := RoomsIni.ReadString('rooms',
CurrentLocation, 'ERROR');
    RoomsIni.Free;

    if Copy(CurrentLocationExe, Length(CurrentLocationExe)-
2,3) = 'dll' then begin
    if CurrentLocation = 'living' then
    begin
        LivingroomForm;
    end else if CurrentLocation = 'kitchen' then begin
        KitchenForm;
    end;
    Timer1.Enabled:=True;
end else begin
    StrPCopy(cmd, CurrentLocationExe);

    Other:=WinExec(cmd, SW_SHOW);
    if Other < HINSTANCE_ERROR then begin
    end else begin
        Timer1.Enabled:=True;
    end;
end;
end;
end;
end.

unit Bath1;

interface

uses
    SysUtils, WinTypes, WinProcs, Messages, Classes, Graphics,
Controls,
    Forms, Dialogs, IniFiles, StdCtrls, ExtCtrls;

type
    TForm1 = class(TForm)
        Label1: TLabel;
        Button1: TButton;
        ToothpasteStatus: TLabel;
        Image1: TImage;
        Label2: TLabel;
        Label3: TLabel;
        Button2: TButton;
        procedure Button1Click(Sender: TObject);
        procedure Button2Click(Sender: TObject);
        procedure FormCreate(Sender: TObject);
    private
        { Private declarations }
    public
        { Public declarations }
    end;

var
    Form1: TForm1;

implementation

```

```

{$R *.DFM}

procedure TForm1.Button1Click(Sender: TObject);
var
    GameIni : TIniFile;
begin
    GameIni :=
TIniFile.Create('d:\delphi\source\launch\STATUS.INI');
    GameIni.WriteString('location', 'current', 'bedroom');
    GameIni.Free;
    Halt;
end;

procedure TForm1.Button2Click(Sender: TObject);
var
    GameIni : TIniFile;
begin
    GameIni :=
TIniFile.Create('d:\delphi\source\launch\STATUS.INI');
    GameIni.WriteString('location', 'current', 'toolshed');
    GameIni.Free;
    Halt;
end;

procedure TForm1.FormCreate(Sender: TObject);
var
    StatusIni: TIniFile;
begin
    StatusIni :=
TIniFile.Create('d:\delphi\source\launch\status.INI');
    StatusIni.WriteString('location', 'current', 'EXIT');
    if StatusIni.ReadBool('items', 'toothpaste', False) = True then
    begin
        ToothpasteStatus.Caption := 'There"s toothpaste in the
cabinet.';
    end else begin
        ToothpasteStatus.Caption := 'You need to buy toothpaste.';
    end;
    StatusIni.Free;
end;

end.

unit Bedroom3;

interface

uses
    SysUtils, WinTypes, WinProcs, Messages, Classes, Graphics,
Controls,
    Forms, Dialogs, StdCtrls;

type
    TForm3 = class(TForm)
        Label1: TLabel;
        procedure Label1Click(Sender: TObject);
    private
        { Private declarations }
    public
        { Public declarations }
    end;

var
    Form3: TForm3;

```

```

implementation

{$R *.DFM}

procedure TForm3.Label1Click(Sender: TObject);
begin
  Close;
end;

end.

unit Drug1;

interface

uses
  SysUtils, WinTypes, WinProcs, Messages, Classes, Graphics,
  Controls,
  Forms, Dialogs, IniFiles, StdCtrls;

type
  TForm1 = class(TForm)
    Label1: TLabel;
    Button1: TButton;
    ListBox1: TListBox;
    ListBox2: TListBox;
    ToothpasteStatus: TLabel;
    Button2: TButton;
  procedure Button1Click(Sender: TObject);
  procedure Button2Click(Sender: TObject);
  procedure FormCreate(Sender: TObject);
  private
    { Private declarations }
  public
    { Public declarations }
  end;

var
  Form1: TForm1;

implementation

{$R *.DFM}

procedure TForm1.Button1Click(Sender: TObject);
var
  GameIni: TIniFile;
begin
  GameIni :=
  TIniFile.Create('c:\data\k\oddf\nasagame\titan\launcher\STAT
  US.INI');
  GameIni.WriteString('location', 'current', 'kitchen');
  GameIni.Free;
  Halt;
end;

procedure TForm1.Button2Click(Sender: TObject);
var
  GameIni: TIniFile;
begin
  GameIni :=
  TIniFile.Create('d:\delphi\source\launch\STATUS.INI');
  GameIni.WriteBool('items', 'toothpaste', True);
  GameIni.Free;
  ToothpasteStatus.Caption := 'You now have some
  toothpaste.';

```

```

end;

procedure TForm1.FormCreate(Sender: TObject);
var
  StatusIni: TIniFile;
  B: Integer;
begin
  StatusIni :=
  TIniFile.Create('d:\delphi\source\launch\status.INI');
  StatusIni.WriteString('location', 'current', 'EXIT');
  StatusIni.ReadSection('location', ListBox1.Items);
  for B := 0 to (ListBox1.Items.Count - 1) do
  begin
    ListBox2.Items.Add(StatusIni.ReadString('location',
    ListBox1.Items[B], 'ERROR'));
  end;
  if StatusIni.ReadBool('items', 'toothpaste', False) = True then
  begin
    ToothpasteStatus.Caption := 'You already have some
    toothpaste.';
  end else begin
    ToothpasteStatus.Caption := 'You need to buy toothpaste.';
  end;
  StatusIni.Free;
end;

end.

unit Grocery1;

interface

uses
  SysUtils, WinTypes, WinProcs, Messages, Classes, Graphics,
  Controls,
  Forms, Dialogs, IniFiles, StdCtrls;

type
  TForm1 = class(TForm)
    Label1: TLabel;
    Button1: TButton;
    ListBox1: TListBox;
    ListBox2: TListBox;
    FoodStatus: TLabel;
    Button2: TButton;
  procedure Button1Click(Sender: TObject);
  procedure Button2Click(Sender: TObject);
  procedure FormCreate(Sender: TObject);
  private
    { Private declarations }
  public
    { Public declarations }
  end;

var
  Form1: TForm1;

implementation

{$R *.DFM}

procedure TForm1.Button1Click(Sender: TObject);
var
  GameIni: TIniFile;
begin

```

```

GameIni :=
TIniFile.Create('d:\delphi\source\launch\STATUS.INI');
GameIni.WriteString('location', 'current', 'kitchen');
GameIni.Free;
Halt;
end;

procedure TForm1.Button2Click(Sender: TObject);
var
  GameIni : TIniFile;
begin
  GameIni :=
TIniFile.Create('d:\delphi\source\launch\STATUS.INI');
  GameIni.WriteBool('items', 'food', True);
  GameIni.Free;
  FoodStatus.Caption := 'You now have some food.';
end;

procedure TForm1.FormCreate(Sender: TObject);
var
  StatusIni: TIniFile;
  B : Integer;
begin
  StatusIni :=
TIniFile.Create('d:\delphi\source\launch\status.INI');
  StatusIni.WriteString('location', 'current', 'EXIT');
  StatusIni.ReadSection('location', ListBox1.Items);
  for B := 0 to (ListBox1.Items.Count - 1) do
  begin
    ListBox2.Items.Add(StatusIni.ReadString('location',
ListBox1.Items[B], 'ERROR'));
  end;
  if StatusIni.ReadBool('items', 'food', False) = True then
  begin
    FoodStatus.Caption := 'You already have some food.';
  end else begin
    FoodStatus.Caption := 'You need to buy groceries.';
  end;
  StatusIni.Free;
end;

end.

unit Kitchen2;

interface

uses
  SysUtils, WinTypes, WinProcs, Messages, Classes, Graphics,
  Controls,
  Forms, Dialogs, Inifiles, StdCtrls, ExtCtrls;

type
  TForm1 = class(TForm)
    Label1: TLabel;
    Button1: TButton;
    Button2: TButton;
    Button3: TButton;
    FoodStatus: TLabel;
    ToothpasteStatus: TLabel;
    Button4: TButton;
    Image1: TImage;
    Button5: TButton;
    procedure Button1Click(Sender: TObject);
    procedure Button2Click(Sender: TObject);
    procedure FormCreate(Sender: TObject);

```

```

    procedure Button3Click(Sender: TObject);
    procedure FormDestroy(Sender: TObject);
    procedure Button4Click(Sender: TObject);
  private
    { Private declarations }
  public
    { Public declarations }
  end;

```

```

var
  Form1: TForm1;

procedure KitchenForm; export;

```

implementation

```

{$R *.DFM}
procedure KitchenForm;
begin
  try
    Form1 := TForm1.Create(Application);
    Form1.ShowModal;
  finally
    Form1.Free;
  end;
end;
end;

```

```

procedure TForm1.Button1Click(Sender: TObject);
var
  GameIni : TIniFile;
begin
  GameIni :=
TIniFile.Create('c:\data\k\cddf\nasagame\titan\launcher\STAT
US.INI');
  GameIni.WriteString('location', 'current', 'drug');
  GameIni.Free;
  close;
end;
end;

```

```

procedure TForm1.Button2Click(Sender: TObject);
var
  GameIni : TIniFile;
begin
  GameIni :=
TIniFile.Create('c:\data\k\cddf\nasagame\titan\launcher\STAT
US.INI');
  GameIni.WriteString('location', 'current', 'living');
  GameIni.Free;
  close;
end;
end;

```

```

procedure TForm1.FormCreate(Sender: TObject);
var
  StatusIni: TIniFile;
begin
  StatusIni :=
TIniFile.Create('c:\data\k\cddf\nasagame\titan\launcher\status.I
NI');
  StatusIni.WriteString('location', 'current', 'EXIT');
  if StatusIni.ReadBool('items', 'toothpaste', False) = True then
  begin
    ToothpasteStatus.Caption := 'You have some toothpaste
now.';
  end else begin
    ToothpasteStatus.Caption := 'You need to buy toothpaste.';
  end;
end;
end;

```

```

if StatusIni.ReadBool('items', 'food', False) = True then
begin
  FoodStatus.Caption := 'There"s some yummy food here.';
end else begin
  FoodStatus.Caption := 'The cupboards are bare!';
end;
StatusIni.Free;
end;

procedure TForm1.Button3Click(Sender: TObject);
var
  GameIni : TIniFile;
begin
  GameIni :=
  TIniFile.Create('c:\data\k\cddf\nasagame\titan\launcher\STAT
US.INI');
  GameIni.WriteString('location', 'current', 'airstrip');
  GameIni.Free;
  close;
end;

procedure TForm1.FormDestroy(Sender: TObject);
var
  StatusIni : TIniFile;
begin
  StatusIni :=
  TIniFile.Create('c:\data\k\cddf\nasagame\titan\launcher\status.I
ni');
  StatusIni.WriteString('location','previous','kitchen');
  StatusIni.Free;
end;

procedure TForm1.Button4Click(Sender: TObject);
var
  Statusini : TIniFile;
begin
  StatusIni :=
  TIniFile.Create('c:\data\k\cddf\nasagame\titan\launcher\status.I
ni');
  StatusIni.WriteString('location','current',statusini.readstring('loc
ation','previous','Error'));
  Statusini.Free;
  close;
end;

end.

unit Living1;

interface

uses
  SysUtils, WinTypes, WinProcs, Messages, Classes, Graphics,
  Controls,
  Forms, Dialogs, Inifiles, StdCtrls;

type
  TForm1 = class(TForm)
    Label1: TLabel;
    Button1: TButton;
    Button2: TButton;
    ListBox1: TListBox;
    ListBox2: TListBox;
    procedure Button1Click(Sender: TObject);
    procedure Button2Click(Sender: TObject);

```

```

    procedure FormCreate(Sender: TObject);
    procedure FormDestroy(Sender: TObject);
  private
    { Private declarations }
  public
    { Public declarations }
  end;

var
  Form1: TForm1;
implementation

{$R *.DFM}

procedure TForm1.Button1Click(Sender: TObject);
var
  GameIni : TIniFile;
begin
  GameIni :=
  TIniFile.Create('d:\delphi\source\launch\STATUS.INI');
  GameIni.WriteString('location', 'current', 'bedroom');
  GameIni.Free;
  Halt;
end;

procedure TForm1.Button2Click(Sender: TObject);
var
  GameIni : TIniFile;
begin
  GameIni :=
  TIniFile.Create('d:\delphi\source\launch\STATUS.INI');
  GameIni.WriteString('location', 'current', 'kitchen');
  GameIni.Free;
  Halt;
end;

procedure TForm1.FormCreate(Sender: TObject);
var
  StatusIni: TIniFile;
  B : Integer;
begin
  StatusIni :=
  TIniFile.Create('d:\delphi\source\launch\status.INI');
  StatusIni.WriteString('location','current','EXIT');
  StatusIni.ReadSection('location', ListBox1.Items);
  for B := 0 to (ListBox1.Items.Count - 1) do
  begin
    ListBox2.Items.Add(StatusIni.ReadString('location',
    ListBox1.Items[B],'ERROR'));
  end;
  StatusIni.Free;
end;

procedure TForm1.FormDestroy(Sender: TObject);
var
  StatusIni: TIniFile;
begin
  StatusIni :=
  TIniFile.Create('d:\delphi\source\launch\status.INI');
  StatusIni.WriteString('location', 'previous','living');
  StatusIni.Free;
end;

```

```

end.

unit Tools1;

interface

uses
  SysUtils, WinTypes, WinProcs, Messages, Classes, Graphics,
  Controls,
  Forms, Dialogs, IniFiles, StdCtrls, ExtCtrls;

type
  TForm1 = class(TForm)
    Label1: TLabel;
    Button1: TButton;
    Image1: TImage;
    Image2: TImage;
    procedure Button1Click(Sender: TObject);
    procedure Button2Click(Sender: TObject);
    procedure FormCreate(Sender: TObject);
    procedure Image2Click(Sender: TObject);
  private
    { Private declarations }
  public
    { Public declarations }
  end;

var
  Form1: TForm1;

implementation

{$R *.DFM}

procedure TForm1.Button1Click(Sender: TObject);
var
  GameIni : TIniFile;
begin
  GameIni :=
  TIniFile.Create('d:\delphi\source\launch\STATUS.INI');
  GameIni.WriteString('location', 'current', 'ball');
  GameIni.Free;
  Halt;
end;

procedure TForm1.Button2Click(Sender: TObject);
var
  GameIni : TIniFile;
begin
  GameIni :=
  TIniFile.Create('d:\delphi\source\launch\STATUS.INI');
  GameIni.WriteString('location', 'current', 'toolshed');
  GameIni.Free;
  Halt;
end;

procedure TForm1.FormCreate(Sender: TObject);
var
  StatusIni: TIniFile;
begin
  StatusIni :=
  TIniFile.Create('d:\delphi\source\launch\status.INI');
  StatusIni.WriteString('location','current','EXIT');
  StatusIni.Free;
end;

procedure TForm1.Image2Click(Sender: TObject);
var
  GameIni : TIniFile;
begin
  GameIni :=
  TIniFile.Create('d:\delphi\source\launch\STATUS.INI');
  GameIni.WriteString('location', 'current', 'bath');
  GameIni.Free;
  Halt;
end;

end.

```

ACKNOWLEDGMENTS

I appreciate the tremendous help of my NASA Research Colleague, Kenneth C. Jenks, this summer. I am grateful for his advice in selecting this project and to NASA for the opportunity to work here. I also appreciate the ASEE Summer Faculty Program and its JSC coordinator, Prof. Richard B. Bannerot for all his cheerful enthusiasm, patience and assistance in showing the new faculty around JSC with tours and seminars. I also am pleased to acknowledge the excellent software programming of a number of students: John D. Smith, Donna Panter, Jimmy Elmore, Shruti Bahadur, and Hong Zhang.

COVER PAGE

510-90

038291

141.

294268

Studies of magmatic inclusions in the basaltic martian meteorites
Shergotty, Zagami, EETA 79001 and QUE 94201

Ralph P. Harvey
Case Western Reserve University
JSC Mail code SN4
2 August 1996

Gordon A. McKay
Planetary Science Branch
Earth Science and Solar System Exploration Division
Space and Life Sciences Directorate

(Signature)



Summer Faculty Fellow

(Signature)



NASA Colleague

**STUDIES OF MAGMATIC INCLUSIONS IN THE BASALTIC MARTIAN METEORITES
SHERGOTTY, ZAGAMI, EETA 79001 AND QUE 94201**

Final Report
NASA / ASEE Summer Faculty Fellowship Program- 1996
Johnson Space Center

Prepared by: Ralph P. Harvey
Academic Rank: Senior Research Associate
University & Department: Case Western Reserve University
Department of Geological Sciences
Cleveland, OH 44106-7216

NASA / JSC
Directorate: Space and Life Sciences
Division: Earth Science and Solar System Exploration
Branch: Planetary Science
JSC Colleague: Gordon A. McKay
Date Submitted: 2 August 1996
Contract Number: NGT-44-001-800

ABSTRACT

Currently there are 12 meteorites thought by planetary scientists to be martian samples, delivered to the Earth after violent impacts on that planet's surface. Of these 12 specimens, 4 are basaltic: Shergotty, Zagami, EETA 79001 and QUE 94201. Basalts are particularly important rocks to planetary geologists- they are the most common rocks found on the surfaces of the terrestrial planets, representing volcanic activity of their parent worlds. In addition, because they are generated by partial melting of the mantle and/or lower crust, they can serve as guideposts to the composition and internal processes of a planet. Consequently these four meteorites can serve as "ground-truth" representatives of the predominant volcanic surface rocks of Mars, and offer researchers a glimpse of the magmatic history of that planet.

Unfortunately, unraveling the parentage of a basaltic rock is not always straightforward. While many basalts are simple, unaltered partial melts of the mantle, others have undergone secondary processes which change the original parental chemistry, such as assimilation of other crustal rocks, mixing with other magmas, accumulation, re-equilibration between mineral species after crystallization, loss of late-stage magmatic fluids and alteration by metamorphic or metasomatic processes. Fortunately, magmatic inclusions can trap the evolving magmatic liquid, isolating it from many of these secondary processes and offering a direct look at the magma during different stages of development. These inclusions form when major or minor phases grow skeletally, surrounding small amounts of the parental magma within pockets in the growing crystal. The inclusion as a whole (usually consisting of glass with enclosed crystals) continues to represent the composition of the parental magma at the time the melt pocket closed, even when the rock as a whole evolves under changing conditions. The four basaltic martian meteorites contain several distinct generations of melt inclusions; those found within early-forming pigeonite, intermediate and late-forming Ti,Fe-oxides and sulfides, and intermediate to late-forming phosphates.

In this summer's study we have made a detailed study of all of the various forms of inclusions found within the 4 basaltic martian meteorites listed above. Glasses and minerals within the inclusions were analyzed using the Cameca SX-100 Electron Microprobe in Building 31. The mineralogy and textural context of the inclusions will then be used to explore the crystallization history of these specimens, and to investigate any differences in crystallization history or parental magma compositions between these rocks. In this manner, the magmatic inclusions provide a road map backwards toward the "parental" compositions for the basaltic martian meteorites and provides significant insight into the igneous processes found within the crust of Mars.

INTRODUCTION

The most common type of surficial igneous rock in the solar system is basalt, and consequently an understanding of basalt mineralogy, chemistry and petrogenesis is crucial for understanding planetary processes. In recent years, particular interest has focused on a group of four basaltic lithologies thought to have come from the planet Mars [see ref. 1 and references therein]. These samples, Shergotty, Zagami, EETA 79001 and QUE 94201, known as the basaltic shergottites, share several common features and in general resemble pyroxene-rich terrestrial basalts. One important feature that these rocks share is the presence of magmatic inclusions in several different minerals within the rock. These magmatic inclusions were formed when ambient melt that was trapped within growing crystals, and as a result they represent the composition of the surrounding magma at various stages in the evolution of the parental magmatic liquid. Previous studies have focused on magmatic inclusions in Shergotty and Zagami pyroxenes to investigate parental magma composition and evolution [2,3]. In this study, we extend this work with studies of inclusions in all four basaltic shergottites (including EETA 79001 and QUE 94201), and also include studies of later generations of melt inclusions found in oxide and phosphate phases.

ANALYTICAL TECHNIQUES

Polished thin sections of Shergotty (UNM 409), Zagami (UNM 993 and UH 233), EETA 79001 (TS 69) and QUE 94201 (TS 6, 37, and 38) were initially examined under a polarizing optical microscope. Backscattered images, elemental maps and quantitative analyses were acquired using the Cameca SX-100 electron microprobe in Building 31 at the Johnson Space Center, at an accelerating potential of 15 keV and a beam current of 20 nA. Beam size varied between 1 and 10 microns depending on the volatile loss of various phases analyzed, and well-characterized standards and ZAF procedures were used to correct for matrix effects.

PETROGRAPHY

The rocks as a whole All of the basaltic shergottites have been previously described by a number of authors: representative papers are listed and only a short description will be provided here [4-7]. These rocks are composed predominantly of relatively Fe-rich pyroxene (pigeonite) and anorthitic feldspar (converted to maskelynite by shock), with varying amounts of secondary minerals such as olivine, augite, Ti- and Fe- oxides, phosphates, and sulfides. Although textures vary from sample to sample, in all four specimens pigeonite generally occurs as elongate, strongly zoned euhedral to subhedral grains, with maskelynite occurring predominantly as an interstitial phase. All four specimens exhibit features consistent with long crystallization histories, such as extremely Fe-rich compositions in the mesostasis, though to varying degrees. Shergotty, as the type lithology of the shergottites, shows the most consistent texture from thin-section to thin-section, with relatively little variation in grain size and the modal percentage of pyroxene, maskelynite and mesostasis from section to section. EETA 79001 also shows little variation in modal abundance of pyroxene and maskelynite, but in hand-sample exhibits a lithological contact between a finer grained, more uniform basaltic lithology (lithology B) and a xenocryst-bearing, less uniform basaltic lithology (lithology A). In this study, only lithology B was examined for inclusions. Zagami resembles Shergotty in modal abundances of pyroxene and maskelynite, but exhibits widely varying grain size from thin section to thin section. In addition, some thin sections of Zagami exhibit significant amounts of "dark, mottled lithology", regions of abundant late-stage Fe-rich mesostasis including fayalite-silica intergrowths and large oxide and phosphate crystals. Like Zagami, QUE 94201 exhibits significant differences in pyroxene and maskelynite habit from thin-section to thin-section. Modal abundances of maskelynite can vary from 30 to 55% and pyroxene can occur as small, concentrically zoned euhedral grains, larger, cryptically zoned

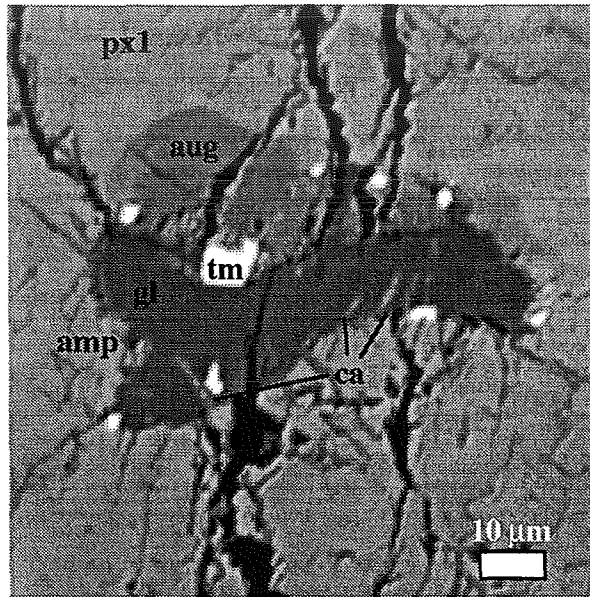


Figure 1. Backscattered electron photomicrograph of typical trapped melt inclusion in Zagami pyroxene (scale bar = 10 μm). The host pyroxene crystal (px1) surrounds several daughter phases including augite (aug), titanomagnetite (tm), chlorapatite needles (ca), and amphibole (amp), as well as glass (gl) representing trapped, uncrystallized magmatic liquid.

Table 1. Representative compositions of host and daughter phases for magmatic inclusions.

<i>Early formed pyroxene host</i>										<i>Early-forming oxide host</i>			
phase	glass	sulfide	whitl.	spinel	augite	pig.	amph.	timag.	ilm.	px-glass	lt glass	dk glass	
SO ₃	0.03	93.51	0.07	0.14			0.10					0.06	
P ₂ O ₅	0.39	0.00	53.44	0.00			0.52					0.00	
SiO ₂	72.09	0.16	1.66	0.12	49.70	49.83	34.46					71.31	
TiO ₂	0.17	0.09	0.00	0.17	0.60	0.40	10.34		51.06			0.42	
Al ₂ O ₃	17.53	0.26	0.39	50.55	1.99	1.21	15.22		2.01			14.65	
Cr ₂ O ₃	0.04	0.07	0.08	0.84	0.29	0.17	4.50		1.72			0.00	
MgO	0.09	0.01	2.71	4.92	13.08	16.48	4.50		0.43			10.87	
CaO	1.66	0.19	44.41	0.12	16.16	5.31	10.45					4.79	
MnO	0.07	0.04	0.11	0.29	0.51	0.75	0.40		0.45			0.88	
FeO	1.14	74.88	2.18	37.63	16.58	24.43	20.94		70.07			32.94	
Na ₂ O	3.79	0.00	2.11	0.05	0.23	0.08	1.58					1.66	
K ₂ O	1.62	0.00	0.07	0.01			0.22					6.98	
total	98.61	170.84	107.22	94.95	99.13	98.66	98.83		96.74			100.08	
<i>Late-forming oxide host</i>													
phase	timag.	ilm.	glass	fayalite	albite	ortho.	augite	whitl.	sulfide	sulfide	px-glass	dk glass	
SO ₃	0.02	0.01	0.01	0.02	0.00	0.01	0.00	0.02	96.21			0.03	
P ₂ O ₅	0.00	0.00	0.05	0.11	0.07	0.04	0.07	9.41	0.00			0.21	
SiO ₂	0.09	0.10	77.81	28.96	66.45	67.84	55.87	34.21	0.01			0.14	
TiO ₂	24.72	51.60	0.58	0.15	0.08	0.10	0.72	4.48	1.11			87.27	
Al ₂ O ₃	2.00	0.01	15.23	0.04	24.53	23.13	7.25	7.93	1.11			0.13	
Cr ₂ O ₃	0.03	0.00	0.01	0.01	0.01	0.00	0.04	0.01	0.00			7.73	
MgO	0.09	0.16	0.01	1.76	0.00	0.00	0.82	0.30	0.00			0.01	
CaO	0.00	0.00	0.46	0.20	1.03	0.50	11.16	15.20	0.00			0.06	
MnO	0.61	0.73	0.01	1.52	0.00	0.00	0.50	0.32	0.01			2.42	
FeO	69.76	46.92	1.22	65.54	0.24	0.30	20.79	20.40	80.86			0.11	
Na ₂ O	0.01	0.00	1.16	0.00	1.97	1.81	0.62	0.87	0.00			2.22	
K ₂ O	0.00	0.00	5.08	0.01	6.53	6.47	1.37	2.79	0.00			0.42	
total	97.32	99.54	101.64	98.34	100.93	100.20	99.24	95.94	178.36			99.94	
<i>Early-forming phosphate host</i>													
phase	glass	sulfide	whitl.	glass	fayalite	glass	whitl.	glass?	augite	timag	px-glass	dk glass	
SO ₃		96.21	0.02	0.01	0.02	0.01	0.02	0.01	0.00	0.38			
P ₂ O ₅		0.00	43.57	0.11	0.03	0.10	0.03	1.04	1.03	0.00			
SiO ₂	90.60	0.01	0.09	73.98	48.01	75.27	48.01	42.30	41.97	1.71			
TiO ₂	0.18	1.11	0.02	0.23	0.93	0.19	0.93	2.82	2.74	25.08			
Al ₂ O ₃	4.63	0.00	0.07	16.50	5.43	16.51	5.43	3.30	3.33	5.58			
Cr ₂ O ₃	0.00	0.00	0.00	0.02	0.00	0.00	0.00	0.01	0.02	0.01			
MgO	0.06	0.00	0.50	0.01	1.03	0.00	1.03	0.89	0.91	0.04			
CaO	1.08	0.00	46.83	1.42	16.78	1.55	16.78	17.36	17.40	0.31			
MnO	0.02	0.01	0.21	0.02	0.58	0.03	0.58	0.72	0.76	0.56			
FeO	0.20	80.86	5.41	0.85	26.49	0.84	26.49	30.79	30.90	64.49			
Na ₂ O	1.12	0.00	1.22	1.32	0.47	0.69	0.47	0.21	0.21	0.08			
K ₂ O	2.92	0.00	0.04	5.12	0.76	4.24	0.76	0.01	0.01	0.14			
Total	100.82	178.36	97.98	99.65	100.55	99.45	99.45	99.48	99.31	98.39			

subhedral grains and elongated, needle-like grains more than 1 cm long. QUE 94201 also exhibits significant amounts of "dark, mottled lithology" similar to those in Zagami. In summary, although the basaltic shergottites share major mineralogical characteristics, they exhibit differences in the modal abundance and habit of major minerals. In addition, they exhibit textural and modal differences from area to area (in QUE, on the scale of thin sections) within each meteorite, with the exception of Shergotty, whose main mass has not been examined in detail.

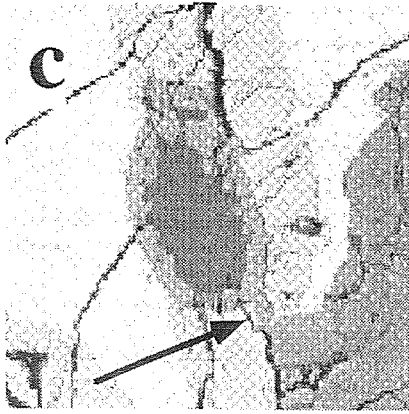
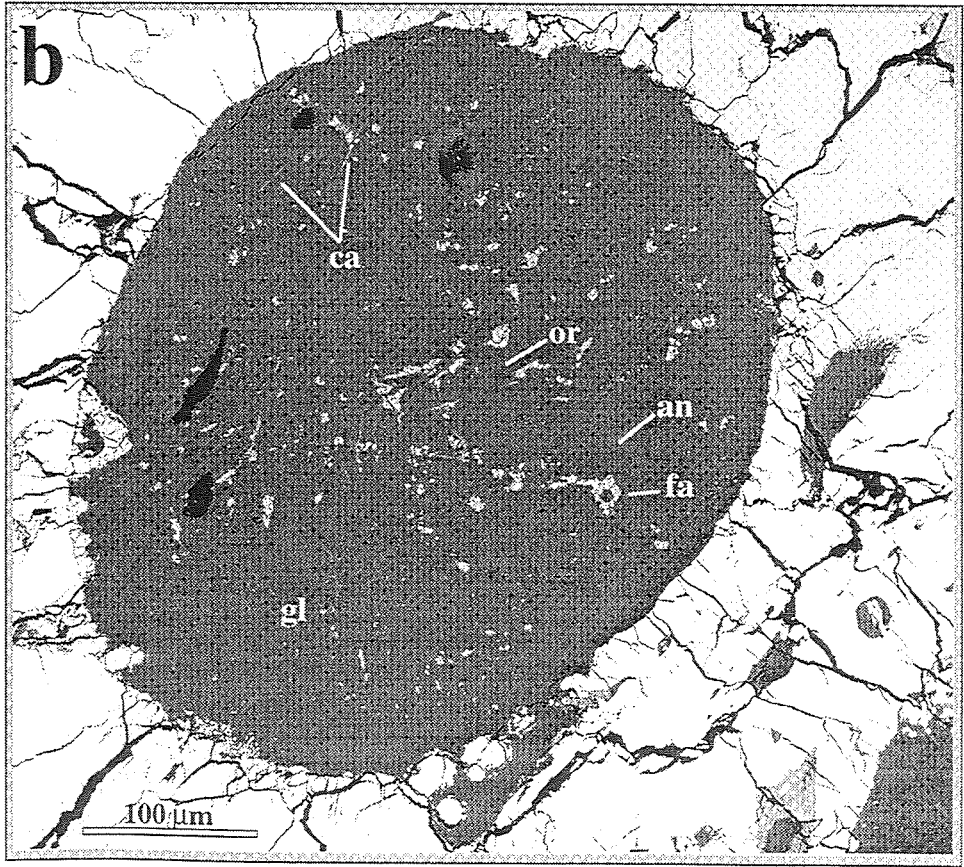
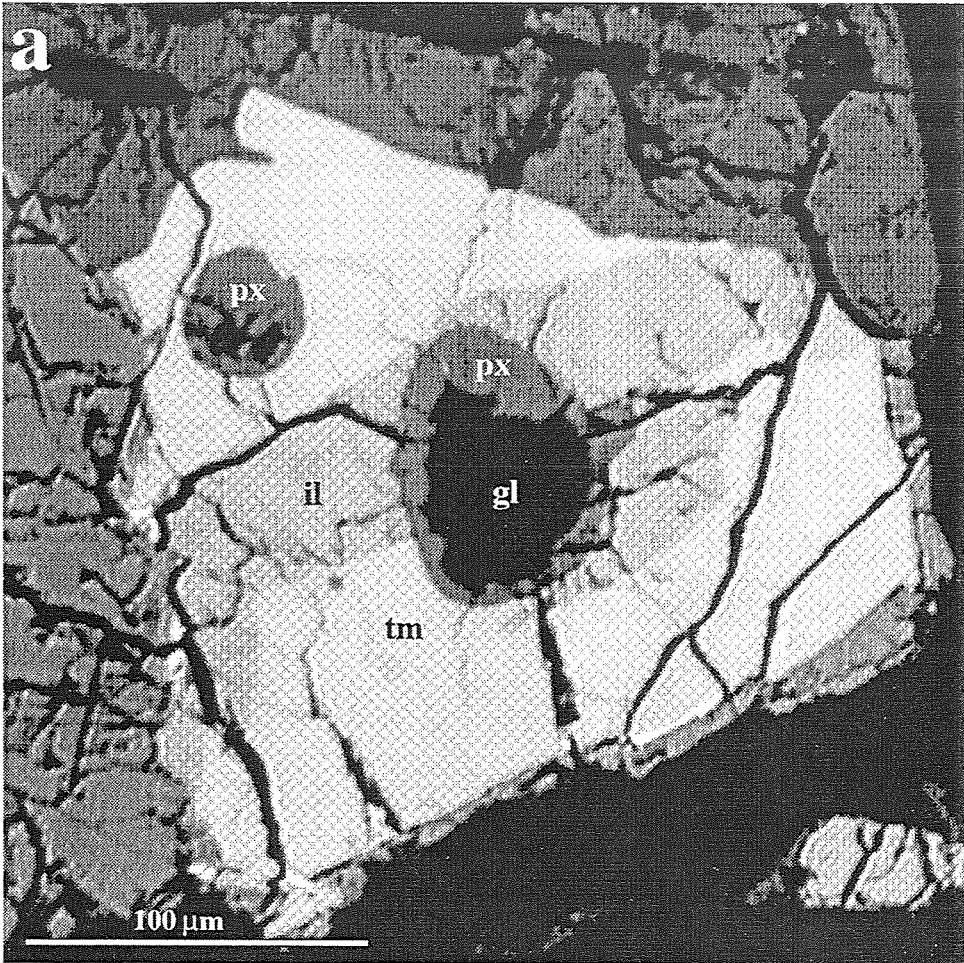
The melt inclusions Melt inclusions can occur in any phase that grows skeletally; in the basaltic shergottites these phases include pyroxene, olivine, oxides and phosphates. Given that these minerals crystallize at different stages in the history of the rock, it is not surprising that each kind of inclusion exhibits distinct mineralogical and textural features. Our observations of these features, including previous studies, are as follows.

-Inclusions in pyroxene Trapped melt inclusions in pyroxenes are the only ones to have been previously studied in detail (and only in Zagami and Shergotty), although inclusions in oxides and phosphates had been noted [2,3,5,8]. Typically these inclusions are quite small (a few tens of microns across), surrounded by a network of radial cracks, and contain both glass and daughter crystals (Fig. 1). Many different daughter phases have been identified during our work and previous studies, including spinel, amphibole, Ti-rich augite, titanomagnetite, ilmenite, pyrrhotite, chlorapatite, and whitlockite [2,3]. As might be expected during pyroxene crystallization, the first phase to crystallize from the trapped melt inclusion is additional host pyroxene, resulting in the observed radial fractures as shrinkage occurs. A second pyroxene is common in the inclusions, usually lining part or all of the inclusion wall. This second pyroxene, often a Ti-rich augite, is quite distinct from the enclosing pigeonite in composition but difficult to distinguish optically. Amphibole, when present, also commonly occurs as a wall-lining. Phosphates, spinels, oxides and sulfides usually occur as small needles or equant euhedral crystals, nucleating off the inclusion walls and usually partially embedded in the surrounding pyroxene. Not all inclusions show all the phases seen, most likely because the random cut of thin sections through the rock does not always show all the phases present. Table 1 shows representative mineral compositions for pyroxene melt inclusion phases.

-Inclusions in oxides Trapped melt inclusions in oxides in Zagami and Shergotty have been noted by several authors, but have not been previously studied [2,5,8]. All of the basaltic shergottites contain abundant late Fe-Ti oxides, usually euhedral grains of titanomagnetite containing significant areas of exsolved ilmenite. Textural and fractional crystallization studies of these oxides indicate that they began forming sometime not long after the onset of pyroxene crystallization and increased in abundance throughout the remaining crystallization history of the rock, as the content of Fe and Ti increased in the parental magma. Inclusions in oxides are large by comparison to those found in pyroxene, centrally located within the host grain, and can be in contact with either Fe,Ti-oxide phase, indicating that they were trapped early in the growth of the host crystal. In general, the inclusions are largest and most numerous in basaltic shergottite lithologies with the most evolved composition and coarsest overall grain size- the largest oxide-hosted inclusions are found in Zagami's dark mottled lithology, while the smallest are found in Shergotty and EETA 79001. Again, this probably reflects the increased Ti-Fe content of the magma and may also indicate slow cooling rates at the terminus of crystallization.

Inclusions in oxides are relatively simple by comparison to those found in pyroxene hosts. Their general form is quite rounded, and often a host crystal will contain several inclusions with identical mineralogies. Ti-Fe oxide-hosted inclusions take two general forms. Inclusions trapped in early formed oxides exhibit an exterior mantle of pyroxene surrounding interior glass, indicating that the liquid they trapped was still crystallizing abundant pyroxene (Fig. 2a). This type of inclusion predominates in Shergotty, EETA 79001, and fine-grained lithologies in Zagami. Inclusions trapped in later-formed oxides are predominantly glassy and contain a smaller amount of mafic silicates- they rarely show much pyroxene content, and can contain crystallites of fayalite similar to those found in the mesostasis of Zagami's dark mottled lithology (Fig. 2b). The glass in later-formed inclusions contains many of the same phases seen in pyroxene inclusions, such as needles of chlorapatite, and very small oxide and sulfide grains. In addition, the glass often

Figure 2. Backscattered electron photomicrographs of representative Ti, Fe-oxide grains bearing magmatic inclusions. **a.** shows two typical inclusions within a single early-formed exsolved oxide grain (consisting of titanomagnetite (tm) and ilmenite (il), exhibiting a pyroxene mantle (px) surrounding interior glass (gl). **b.** shows a large inclusion in a late-formed Ti, Fe-oxide grain, containing wall-nucleated and suspended grains of fayalite (fa), chlorapatite (ca) and surrounded by a glass rich in anorthite (an) and orthoclase (or) crystallites (visible as subtle light and dark patches in the grey background). **c.** Oxide-hosted inclusion showing "channel" linking interior inclusion to external mesostasis.



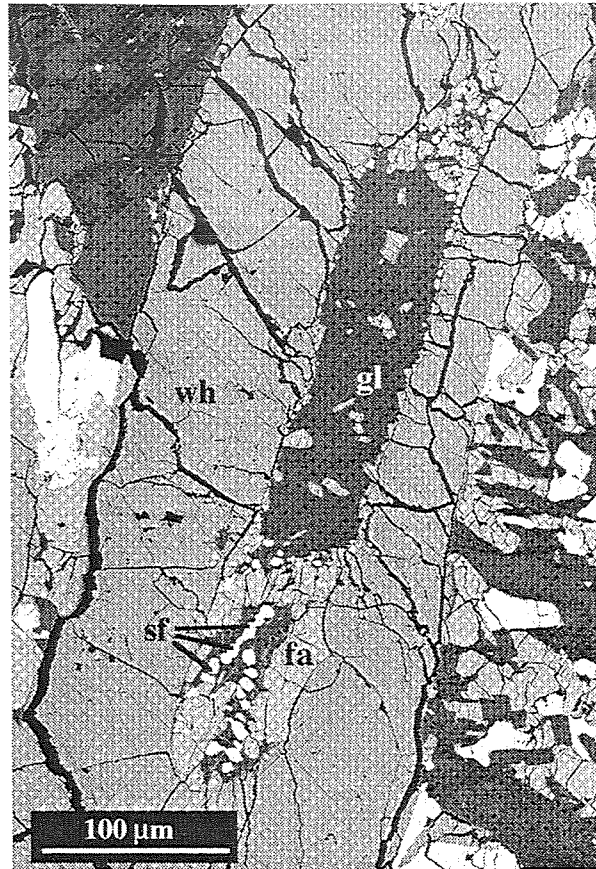


Figure 3. Backscattered electron photomicrograph of representative inclusion in phosphate. The host crystal is composed of whitlockite (wh), and the inclusion consists of fayalite (fa) and sulfide (sf) daughter crystals nucleating off the walls and ends of the inclusion within the interior glass (gl).

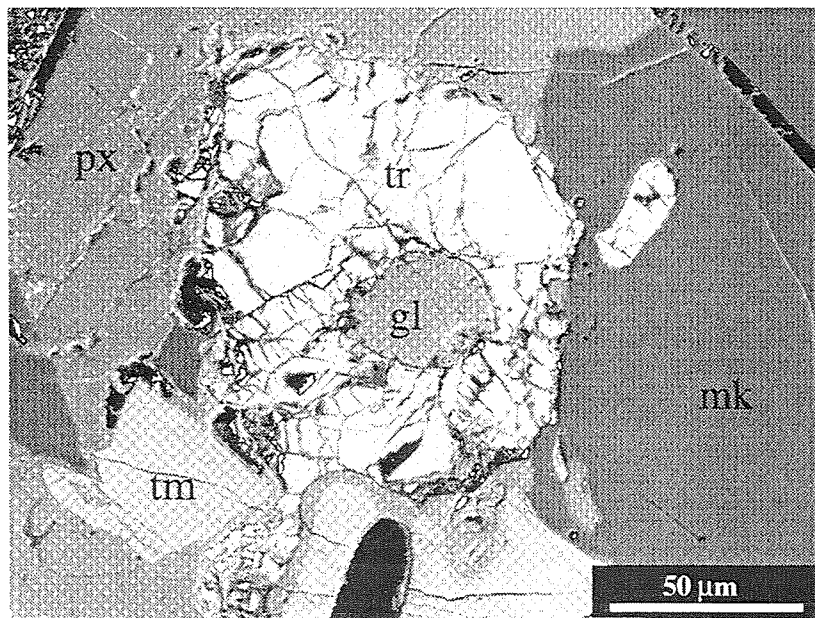


Figure 4. Backscattered electron photomicrograph of representative inclusion in sulfide. The host crystal is composed of troilite (tr), and the inclusion consists of a pyroxene-normative glass (gl). Surrounding phases consist of pyroxene (px), titanomagnetite (tm), and maskelynite (mk).

contains abundant feldspar crystallites, both anorthite and orthoclase compositions. These later-formed inclusions are commonly found in oxides within coarser basaltic shergottite lithologies such as that shown in QUE, and the dark mottled lithology of Zagami. Some inclusions of both types exhibit "channels" that extend from the interior inclusion through the host crystal to the surrounding mesostasis (Fig. 2c). Representative compositions of phases from inclusions within oxides can be found in Table 1.

-Inclusions in phosphates Trapped melt inclusions in phosphates have been noted previously but, as with the Ti,Fe oxides, not actively studied [2,8]. The basaltic shergottites contain two distinct phosphate phases; whitlockite (in early papers misidentified as merrillite) is the most abundant phase, and minor chlorapatite can be found in highly evolved mesostasis areas and within magmatic inclusions. Both phases are predominantly euhedral, forming elongated lathes or needles, and are found as interstitial or mesostasis components indicating they form very late in the crystallization history of the rock. All of the inclusions studied here were in host crystals of whitlockite.

As is the case with oxide-hosted inclusions, phosphate-hosted inclusions are usually central to the parent crystal and tend to follow its original crystallographic structure, taking the form of an elongated, round-ended tube. As is the case for oxide-hosted inclusions, there are some distinctions between inclusions found in less evolved lithologies and those found in more evolved lithologies. Phosphates from Shergotty and fine-grained Zagami lithologies often contain multiple inclusions and are usually nearly pure glass with few daughter crystals. This glass is a uniform, silica-rich composition distinct from the feldspar-normative glass found in pyroxene and oxide inclusions, suggesting that phosphate crystallized after feldspar crystallization had ceased. Phosphates in more evolved lithologies such as QUE 94201 and the dark mottled lithology of Zagami are more likely to contain a single large inclusions than multiple smaller ones, and these larger inclusions often contain abundant daughter crystals of sulfides, fayalite, and Fe-rich pyroxene nucleating off of the walls of the inclusion, in addition to the interior glass.

Representative compositions of phases from inclusions within phosphates can be found in Table 1.

-Inclusions in sulfides Trapped melt inclusions in sulfide have not been identified previously in the basaltic shergottites. Of the four specimens studied here, only EETA 79001 contains this type of inclusion, which is relatively simple in form. The significance of the absence of sulfide inclusions in the other basaltic shergottites is not known. Typically, inclusions in sulfide are of oval shape and occupy the center of the host grain (Fig 4). EETA 79001 has experienced heavy shock and in most cases the sulfide exhibits significant fracturing. Two different inclusion compositions have been noted; a two-phase glass exhibiting possible immiscibility textures, and a single-phase pyroxene normative glass. Representative compositions of phases from inclusions within sulfides can be found in Table 1.

DISCUSSION / DIRECTIONS FOR FUTURE WORK

The basaltic shergottites are all very similar in terms of the minerals present, and like most basalts probably originated as partial melts of more primitive mantle material. However, the four specimens examined in this study show enough variation to make it certain they have experienced, at a minimum, distinct crystallization histories. Because magmatic inclusions have trapped a small portion of the ambient magmatic fluid, and then allowed it to develop as a "captive" small closed system, they serve as excellent tracers of the evolution of a lithology. The glass found within magmatic inclusions is essentially the ambient liquid remaining after the rock has cooled below solidus temperatures. The composition of this glass reflects the parental magma from which the rock formed as well as the host and daughter minerals which crystallized from it. Consequently, careful study of the compositions of the glasses and minerals associated with the inclusions can provide insight into martian magmatic evolution in the following ways.

-Modal mineralogy The type specimen of the basaltic shergottites, Shergotty, is very even in grain size and consistent in terms of abundance of pyroxene, maskelynite, and oxides. EETA 79001, QUE 94201 and Zagami all contain lithologies very similar to Shergotty in these regards, but also contain other distinct lithologies that set them apart. Both EETA 79001 and Zagami show

planar lithological contacts with coarser-grained, more incompatible-rich units, and QUE 94201 shows a wide range of modal abundances and grain sizes over short distances within the small (13g) specimen. Some correlation is seen between the abundance and texture of inclusions and the types of lithologies present in the host specimen. Pyroxene-hosted inclusions are relatively common on Shergotty and fined-grained Zagami, occurring in perhaps one grain in ten, with many grains hosting several inclusions. However, this type of inclusion is rare in the coarse-grained lithology of Zagami, found only in a few, fine-grained regions of QUE, and very rare in EETA 79001. Differences in the growth rate of pyroxene in the various basaltic shergottites is probably the controlling factor, since skeletal growth of the enclosing host phase is required for trapping, and rapid cooling promotes skeletal growth. Given that basaltic shergottite pyroxenes are also strongly zoned, it may prove possible. These variations suggest that it may be possible to correlate zoning profiles of pyroxene with the presence of magmatic inclusions, and establish the relative cooling rates of the various specimens.

-Melt inclusion mineralogy The early inclusions (those in pyroxene and early formed phosphates and oxides) are different from the later inclusions, as is to be expected; between the times that these various inclusions were enclosed, the ambient magmatic fluid was changing composition as it evolved. Examples of these differences include: the presence of Ti-rich augite, spinels, and amphiboles in pyroxene inclusions, when these phases are not seen in the mesostasis; abundant daughter minerals and K feldspars in oxide inclusions in the dark mottled lithology of Zagami, but none in the early inclusions; only Si-normative glass in early phosphate inclusions, while later inclusions contain abundant daughter phases. The evolution of this magmatic fluid in a closed system is due to the crystallization of various primary mineral species, which result in a fluid enriched in elements not used to make minerals, and depleted in elements that are used to form minerals. In addition, the composition of the ambient liquid may change due to open-system behavior; addition of new magmatic fluids, assimilation of local country rock into the magma chamber, or removal of melt or crystals due to eruption or accumulation on the magma chamber floor. Other observations suggest significant open-system behavior of mobile elements relatively early in the crystallization history- the mineralogy observed in pyroxene-hosted inclusions is significantly different than that seen in the rock as a whole, containing spinels, amphiboles, and augites not seen as mesostasis components. In fact, there appears to be a strong correlation between how early an inclusion formed and how distinct it's mineralogy is from that of the rock as a whole, with pyroxene-hosted inclusions being most unlike mesostasis, and late oxide and phosphate inclusions essentially containing an assemblage of minerals identical to mesostasis. Careful study of these changes may help identify the stage in the crystallization history of the rock when the system essentially "closed".

-Parental magmas Determining the composition of the magma that the basaltic shergottites crystallized from is an important goal, because it will allow study of the broader scale geochemistry of the martian crust and mantle. Unfortunately, although the magmatic inclusion represents a trapped parental melt, the subsequent crystallization of host and daughter phases makes it unrepresentative as found in the rock today. However, some careful "reconstruction", adding back together the daughter and host minerals, can allow an estimate of the parent magma's composition to be calculated. Only the earliest trapped inclusions are useful in this regard; the distinctions noted between the crystallization products found in early magmatic inclusions and the mesostasis of these rocks suggest that the magma may have changed significantly before later inclusions were trapped. Using the composition of various inclusion phases as shown in Table 1, initial estimates of the volume of these phases, and some constraints based on known geochemical properties of magma-mineral interactions, linear regression techniques allow a "best-fit" possible parent composition to be produced [9]. At this time calculations have been performed only on magmatic inclusions in Zagami pyroxenes and oxides, as shown in Table 2. So far these calculations have not produced any surprises, generating compositions that are similar to those produced during previous work (Fig. 5). However, continued work should produce compositions for the other specimens, and provide insight into their possible petrogenetic connections. Reconstruction of later-trapped inclusions, although not representing truly parental compositions, will offer

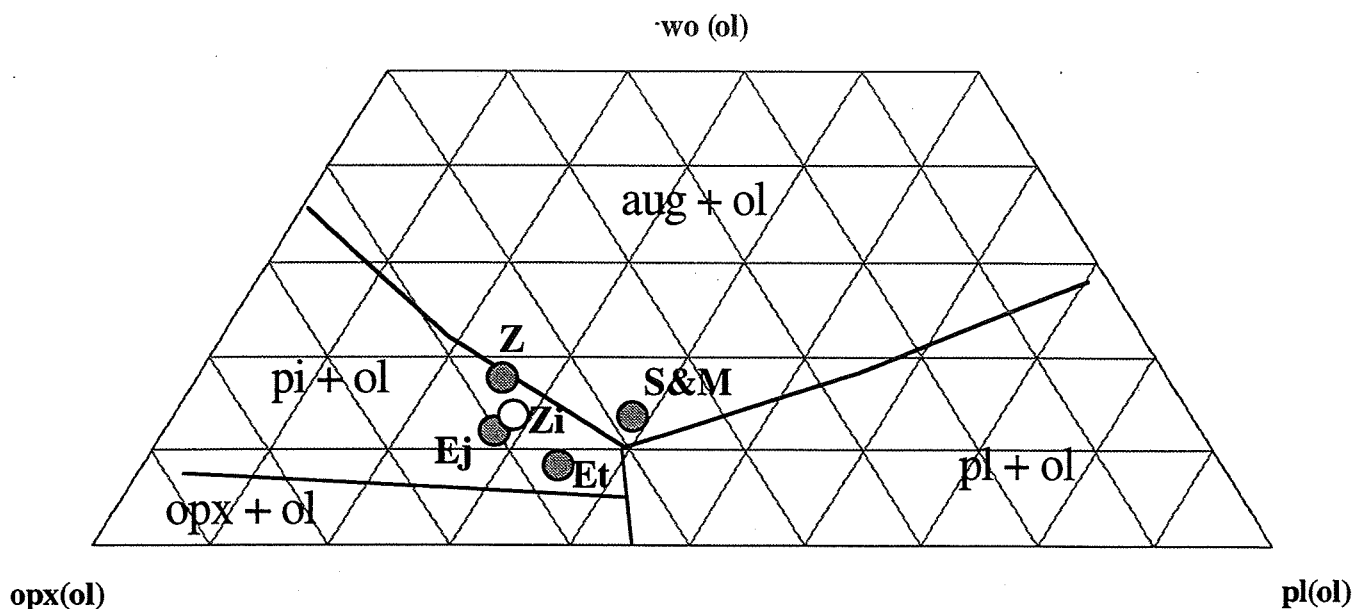


Figure 5. Phase diagram showing the relationship of various proposed parent melts for basaltic shergottites. Dark circles represent proposed parental melt compositions, as projected from olivine in the basalt tetrahedron, are shown as follows. **Z** is the Zagami parent melt from [4], **E** is the EETA79001 parent melt from [6,10], **Et** is EETA79001 from [11], **S** is the Shergotty parent melt from [5]. The white circle labelled **Zi** is the proposed parental melt calculated in this work, based on magmatic inclusions in primary pigeonite in Zagami.

Table 2. Major element composition of possible parent magmas of the basaltic shergottite meteorites. Labels (**Ej**, **EI**, **Zi**, etc.) are as shown in Fig. 5.

	Ej (EETA79001) from [6]	EI (EETA79001) from [10]	S (Shergotty) from [5]	Et (EETA79001) from [11]	Z (Zagami) from [4]	Zi (Zagami) This work
SiO₂	49.20	50.67	50.10	56.50	51.20	49.27
TiO₂	0.78	0.86	1.08	0.69	0.81	2.52
Al₂O₃	6.44	7.10	9.45	12.00	6.19	6.84
MgO	14.40	12.22	5.11	8.40	10.40	9.75
CaO	7.96	8.74	10.00	10.40	10.70	8.10
FeO	18.49	18.67	19.70	7.70	18.20	21.36
Na₂O	0.97	1.07	1.84	1.90	1.29	1.16
K₂O	0.06	0.07	0.24	0.13	0.13	0.82

significant insight into differences in the geochemical evolution of these specimens as well as the evolution of martian basaltic liquids on the whole.

CONCLUSIONS

This work represents the first comprehensive look at magmatic inclusions in all four of the known basaltic shergottites. Inclusions were identified within four different phases; pyroxenes, oxides, phosphates, and sulfides. The textural context of each of these kinds of inclusions was carefully studied, and the abundance and composition of the various host and daughter phases they contain was analyzed. As has been seen during previous, more limited studies, these inclusions are very useful tracers of the history of these rocks. They provide significant insight into the composition of the parental magmas from which the basaltic shergottites formed, as equivalent small samples of the original magmatic liquid they crystallized from. In addition, they offer useful insight into each of the basaltic shergottite's crystallization history. Systematic differences between the siting and composition of the inclusions in the four specimens have been noted, suggesting that each lithology experienced a distinct crystallization history which included open-system behavior to varying degrees. Within individual specimens, detailed comparisons between early- and late-forming inclusions and the mesostasis should allow us to trace the extent of this open-system behavior, and determine to what extent various igneous processes could account for it, such as volatile loss, magma mixing, assimilation, melting, or accumulation. Understanding the number of sources needed to generate the basaltic shergottites, the geological history and setting of the various samples, and what petrogenetic links these meteorites share will help planetary scientists comprehend the nature of volcanic activity on Mars.

REFERENCES

1. McSween H.Y. Jr. (1994) What we have learned about Mars from SNC meteorites. *Meteoritics* **29**, 755-779.
2. Treiman A. H. (1985) Amphibole and hercynite spinel in Shergotty and Zagami: Magmatic water, depth of crystallization, and metasomatism. *Meteoritics* **20**, 229-243.
3. McSween H.Y. Jr. and Harvey R.P. (1993) Outgassed water on Mars: Constraints from melt inclusions in SNC meteorites. *Science* **259**, 1890-1892.
4. McCoy T.J., Taylor G.J. and Keil K. (1992) Zagami: Product of a two-stage magmatic history. *Geochim Cosmochim Acta* **56**, 3571-3582.
5. Stolper E.M. and McSween H.Y. Jr. (1979) Petrology and origin of the shergottite meteorites. *Geochim Cosmochim Acta* **43**, 1475-1498.
6. McSween H.Y. Jr. and Jarosewich E. (1983) Petrogenesis of the Elephant Moraine A79001 meteorite: multiple magma pulses on the shergottite parent body. *Geochim Cosmochim Acta* **47**, 1501-1513.
7. Harvey R.P., McCoy T.J. and Leshin L.A. (1996) Shergottite QUE 94201: texture, mineral compositions and comparison with other basaltic shergottites (abstract). *Abstracts Lunar and Planetary Science Conference* **27**, 497-498.
8. Smith J.V. and Hervig R.L. (1979) Shergotty meteorite: Mineralogy, petrology, and minor elements. *Meteoritics* **14**, 121-142.
9. Harvey R.P. and McSween H.Y. Jr. (1992) Parent magma of the nakhlite meteorites: Clues from melt inclusions. *Earth Planet. Sci. Lett.* **111**, 467-482.
10. Longhi J. and Pan V. (1989) The parent magmas of the SNC meteorites. *Proc. Lunar Planet. Sci. Conf.* **19th**, 451-464.
11. Trieman A. and Sutton S.R. (1992) Petrogenesis of the Zagami meteorite: Inferences from synchrotron X-ray (SXRF) microprobe and electron microprobe analyses of pyroxenes. *Geochim. Cosmochim. Acta* **56**, 4059-4074.

511-32
038292
10P.
294072

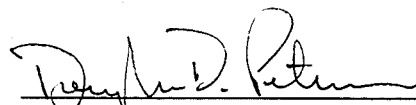
**DEVELOPING TOOLS AND TECHNIQUES
TO INCREASE COMMUNICATION EFFECTIVENESS**

Linda A. Hayes
University of Houston
AP4
August 9, 1996

Doug Peterson
Assistant to the Director
Public Affairs Office



Linda A. Hayes

 8/9/96

Doug Peterson

**DEVELOPING TOOLS AND TECHNIQUES
TO INCREASE COMMUNICATION EFFECTIVENESS**

Prepared by:	Linda A. Hayes, Ph.D.
Academic Rank:	Assistant Professor
University & Department:	University of Houston College of Business Houston, Texas 77204
NASA/JSC Directorate:	Public Affairs Office
JSC Colleague:	Doug Peterson
Date Submitted:	August 9, 1996
Contract Number:	NGT 9 - 867

ABSTRACT

The Public Affairs Office (PAO) of the Johnson Space Center (JSC) is responsible for communicating current JSC Space Program activities as well as goals and objectives to the American Public. As part of the 1996 Strategic Communications Plan, a review of PAO's current communication procedures was conducted. The 1996 Summer Faculty Fellow performed research activities to support this effort by reviewing current research concerning NASA/JSC's customers' perceptions and interests, developing communications tools which enable PAO to more effectively inform JSC customers about the Space Program, and proposing a process for developing and using consistent messages throughout PAO. Note that this research does not attempt to change or influence customer perceptions or interests but, instead, incorporates current customer interests into PAO's communication process.

INTRODUCTION

The Public Affairs Office (PAO) of the Johnson Space Center (JSC) is responsible for communicating current goals and objectives plus all JSC activities to its many customers including the American Public, educators, the media and so on. In addition, by recent executive order, all agencies in the government are to become more customer-focused. These far-reaching responsibilities led to PAO's development of the 1996 JSC Strategic Communications Plan in order to ensure that the American public understands the Space Program's human space flight activities and related research.

As part of the 1996 Strategic Communications Plan, a review of current PAO communication procedures was conducted. The 1996 Summer Faculty Fellow in PAO performed research activities to support PAO's efforts in this area as follows: 1) review current research concerning NASA/JSC's customers' perceptions; 2) develop communication tools which enable PAO to more effectively inform JSC customers about the Space Program; and 3) propose a process for developing and using consistent messages throughout PAO. Each of these activities is discussed below.

CUSTOMER PERCEPTIONS

A recent poll (Ladwig and Miller 1995; Miller 1994) found that only nine per cent of the U.S. public surveyed felt that they were well informed about space exploration. Several factors contribute to this low number. First, Americans face many demands on their time including family, work, leisure, and so on. Time allocated to understanding the Space Program depends on how it ranks with the other priorities of Americans.

Second, people are typically cognitive misers, preferring those items easier to understand. The Space Program is a long-term, complex program which is very scientific in nature. Because of its complexity, people are likely to spend more time to obtain the same level of understanding of Space Program activities than they would other topics, such as sports. Research, such as Miller 1994, found that scientific literacy in the U.S. is quite low. For example, only 72% answered correctly (in a multiple choice questionnaire format) that it takes one year for the Earth to rotate around the Sun.

And, third, people tend to allocate time to those items of interest to them. Again, Miller 1994 shows that Americans are more interested in issues such as the environment, economic conditions and local schools than space exploration.

Yet, national legislation has assigned NASA the task of informing the American public about the Space Program. One of the major functions of NASA outlined in The National Aeronautics and Space Act of 1958 is to "provide for the widest practicable and appropriate dissemination of information concerning its activities and results." In addition, a 1993 Executive Order directed all government agencies to be customer-driven, putting the customer first while providing the customer with the highest quality service. Thus, this research project focused on aiding PAO in developing appropriate tools and methods to effectively accomplish the goals of these directives. For example, see NASA's Customer Service Status Report to the President, March 8, 1994.

COMMUNICATION PROCESS

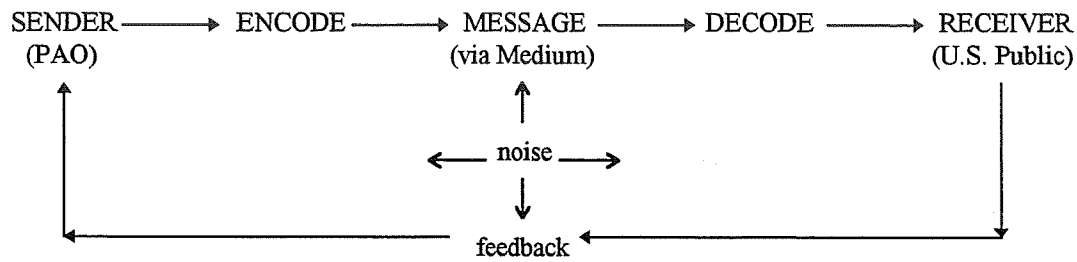
Most proposed communication models are similar to the one shown in Figure 1. In order for the receiver (customer) to obtain the intended message, all of the steps in the model need to take place. The sender (PAO) needs to encode the message in an appropriate manner that the receiver can understand. This encoding may not be easy, especially when the reported activities are highly technical in nature. The sender must transmit the message through a medium that the receiver uses. This not only means TV, for example, but one of the specific TV channels that the receiver watches.

Next, the receiver needs to decode the message. Decoding includes information processing of the message similar to the model in Figure 2. The receiver must first pay attention to the message. If the receiver is not paying attention, the message is lost. As previously discussed, the Public has many other priorities and their attentiveness to Space Program messages may be quite low.

Once attentive, the receiver needs to put the message into language he or she understands for comprehension. This may be an arduous task for Americans low in scientific literacy. Further, research has shown that exposure to the message multiple times is often needed for adequate comprehension and retention of the correct message meaning. That is, the message needs to be sent multiple times and the receiver needs to take in the message multiple times for adequate comprehension and retention to take place.

COMMUNICATION TOOL DEVELOPMENT

The first major objective of this research was to develop tools that would enable PAO to better inform its customers about the Space Program. Data from Ladwig and Miller 1995 suggest a high correlation ($r = .79$) between an individual's interests and his or her perceptions of being well informed. No data was found to determine the temporal positioning (cause and effect) of these two variables. It is quite easy to envision



Communication - the passing of information or ideas between the sender and receiver to inform, remind and increase awareness

Encode - putting the message into understandable form for the receiver

Medium - the way message moves from the sender to receiver - TV, radio, newspaper, etc.

Decode - receiver translates message into understandable form to the receiver

Feedback - sender monitors how message is being received by measuring receiver responses

Noise - factors that can distort or interfere with the message being sent

Figure 1. - Communication Process Model

MESSAGE → ATTENTION → COMPREHENSION → RETENTION

Attention - awareness, notice, concentration of the mind on something

Comprehension - Understand the meaning

Retention - remember, keep in mind

Figure 2. - Receiver Decoding Message - Information Processing Model

situations which illustrate either or both. This research is concerned with how customers become better informed and, therefore, attempts to capture that portion of the relationship where being interested influences being informed. Attention is a major step in processing message information as shown in Figure 2. Typically, an individual will pay more attention to a message concerning a topic he or she is interested than a message concerning a topic he or she is not interested. Attentiveness to a message increases comprehension and retention of the message which, ultimately, increases how well informed the individual is.

Thus, a basic assumption of this research is that a customer's interest or lack of interest in a topic will influence how informed the customer will be. Note, there was no attempt in this research to change or influence customer interests; instead, the proposed communication tools incorporated current customer interests.

From past research (JSC Open House Survey 1995; Ladwig and Miller 1995; Miller 1994; Yankelovich 1996), several thematic areas were identified as being of current interest to NASA/JSC customers. From this data, it appears that customers are more interested in certain aspects of the Space Program than others. The fundamental concept of this research was to develop messages that inform customers about the Space Program but in a manner more in line with customers' current interests.

To accomplish this, a matrix was developed which incorporated customers' current thematic interest areas obtained from research described above and the JSC activities portion of the Space Program. Each JSC activity was related to a thematic area of interest to the customer. The JSC list of activities was developed using the 1996 NASA Vision and Mission and NASA Strategic Plan, the 1996 PAO goals and objectives, JSC's areas of excellence, schedule of current and future JSC Program events and related activities, and so on. Thus, the Themes and Messages Matrix includes themes from customers' current interest areas and messages from JSC activities.

It is envisioned that PAO use the Themes and Messages Matrix to aid in developing messages for JSC customers. When developing messages about JSC activities, PAO incorporates into the message a key thematic area of interest to the customer. Key thematic interest areas are incorporated into JSC messages for three major reasons. First, messages that include a customer's interests will more readily get the customer's attention. If the customer is attending to the message, he or she will listen more closely or read more carefully and, hopefully, retain more. Second, the message is expressed in terms the customer understands since the thematic areas were developed from customer perceptions and feedback. Customer comprehension and retention will increase when the message is structured in a way tailored to the customer. And, third, though the JSC activities reported may vary considerably, the thematic interest areas vary less. This allows for repetition of the thematic interest areas even though the JSC activities may change. Repetition of a thematic area will aid in retention of the JSC activity. Ultimately, as the customer retains more information about JSC activities, he or she will become better informed about the Space Program.

Since Space Program goals and customer interests may vary from time to time, the Themes and Messages Matrix can be revised periodically to reflect this new information.

THEMES AND MESSAGES MANAGEMENT

The second objective of this research was to develop a process where "Themes and Messages" (T&M's) are updated on a timely bases, used consistently throughout PAO, and incorporated into appropriate PAO products. Figure 3 shows the proposed process. The main drivers of messages from PAO to JSC customers are the program and center events and activities (e.g. Shuttle missions, Space Station milestones, special JSC projects, etc.). The earlier customer thematic interest areas are associated with upcoming JSC events and activities, the more effectively PAO teams can integrate T&M's into their products. Thus, PAO personnel who are in the best position to know of upcoming events and activities were identified. These key personnel will come to the weekly PAO Staff Meeting with suggestions for T&M's for the next reporting period. PAO Management approve a set of T&M's and inform the team leads, whose teams integrate the T&M's into their products.

CONCLUSION

Communication is more effective when an organization considers customer perceptions and knowledge. It was proposed that including current interests of customers into PAO messages will aid communication by enhancing customer understanding and knowledge of the Space Program. To accomplish this, a matrix was developed which related JSC activities to current thematic interest areas of the NASA/JSC customers. In addition, a process was developed to aid in identifying messages and using these messages consistently throughout PAO.

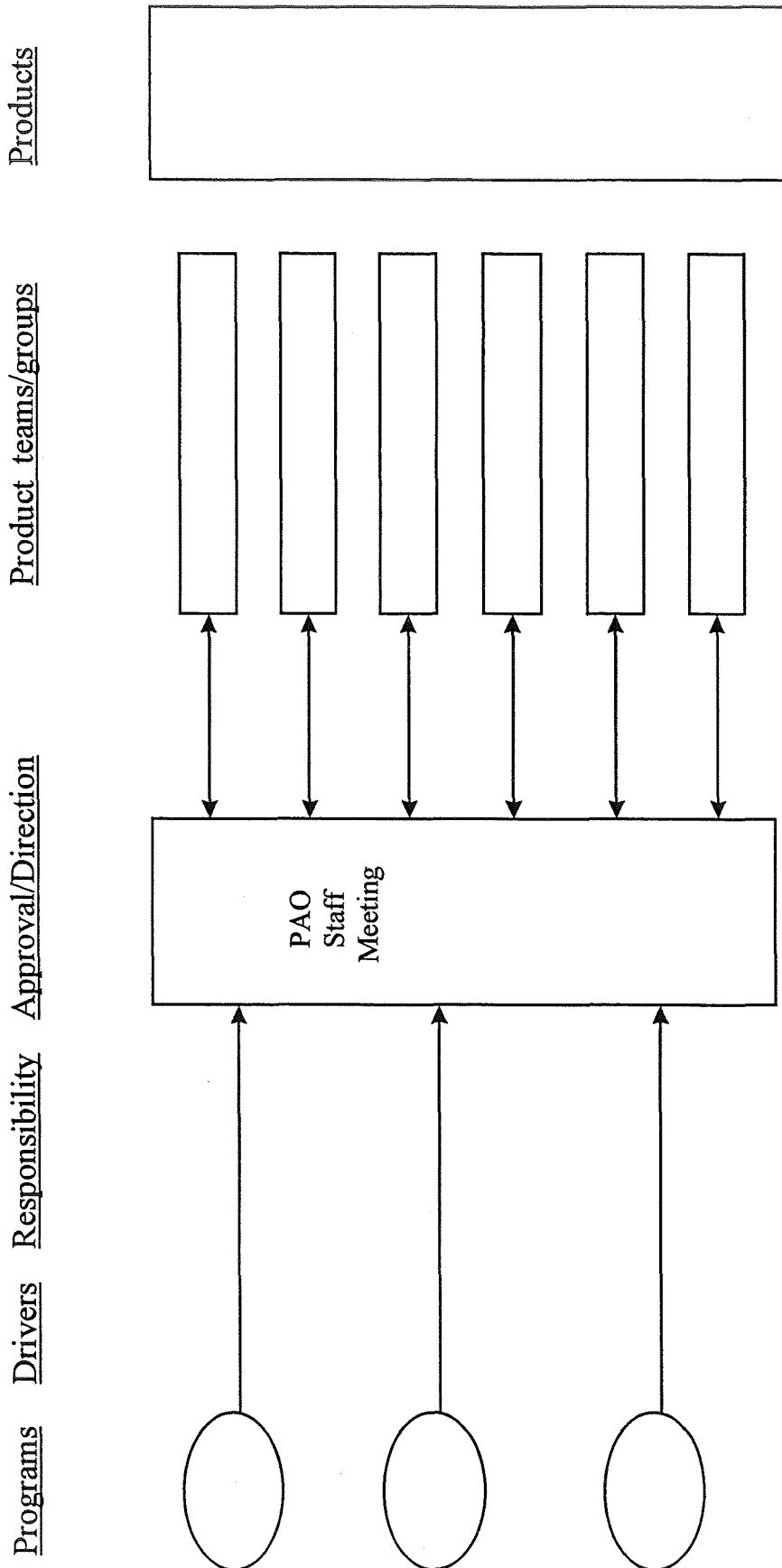


Figure 3. - Process for Developing and Using Messages

REFERENCES

Ladwig, Alan and Jon D. Miller, "Public Attitudes Toward Spending For Space Exploration," paper for Conference of American Association for Advancement of Science, Atlanta, Georgia, 1995.

Miller, Jon, D. "The Information Needs of the Public Concerning Space Exploration," Special NASA Report, 1994.

Yankelovich Partners, Inc., presentation of survey results to Rockwell International, 1996.

312-52
038293

Close

ESTIMATING TRABECULAR BONE MECHANICAL PROPERTIES FROM
NON-INVASIVE IMAGING

294274

141.

Final Report
NASA/ASEE Summer Faculty Fellowship Program--1996
Johnson Space Center

Prepared By: Harry A. Hogan, Ph.D.
Academic Rank: Associate Professor
University & Department: Texas A&M University
Department of Mechanical Engineering
College Station, Texas 77843-3123

NASA/JSC
Directorate: Space and Life Sciences
Division: Medical Sciences
Branch: Life Sciences Research Laboratories
JSC Colleague: Laurie Webster, Ph.D.
Date Submitted: August 2, 1996
Contract Number: NAG 9-867

Approved By: 
Date Approved: 8/2/96

ESTIMATING TRABECULAR BONE MECHANICAL PROPERTIES FROM
NON-INVASIVE IMAGING

Final Report
NASA/ASEE Summer Faculty Fellowship Program--1996
Johnson Space Center

Prepared By: Harry A. Hogan, Ph.D.
Academic Rank: Associate Professor
University & Department: Texas A&M University
Department of Mechanical Engineering
College Station, Texas 77843-3123
NASA/JSC
Directorate: Space and Life Sciences
Division: Medical Sciences
Branch: Life Sciences Research Laboratories
JSC Colleague: Laurie Webster, Ph.D.
Date Submitted: August 2, 1996
Contract Number: NAG 9-867

ABSTRACT

An important component in developing countermeasures for maintaining musculoskeletal integrity during long-term space flight is an effective and meaningful method of monitoring skeletal condition. Magnetic resonance imaging (MRI) is an attractive non-invasive approach because it avoids the exposure to radiation associated with X-ray based imaging and also provides measures related to bone microstructure rather than just density. The purpose of the research for the 1996 Summer Faculty Fellowship period was to extend the usefulness of the MRI data to estimate the mechanical properties of trabecular bone. The main mechanical properties of interest are the elastic modulus and ultimate strength. Correlations are being investigated between these and fractal analysis parameters, MRI relaxation times, apparent densities, and bone mineral densities.

Bone specimens from both human and equine donors have been studied initially to ensure high-quality MR images. Specimens were prepared and scanned from human proximal tibia bones as well as the equine distal radius. The quality of the images from the human bone appeared compromised due to freezing artifact, so only equine bone was included in subsequent procedures since these specimens could be acquired and imaged fresh before being frozen. MRI scans were made spanning a 3.6 cm length on each of 5 equine distal radius specimens. The images were then sent to Dr. Raj Acharya of the State University of New York at Buffalo for fractal analysis. Each piece was cut into 3 slabs approximately 1.2 cm thick and high-resolution contact radiographs were made to provide images for comparing fractal analysis with MR images. Dual energy X-ray absorptiometry (DEXA) scans were also made of each slab for subsequent bone mineral density determination. Slabs were cut into cubes for mechanical using a slow-speed diamond blade wafering saw (Buehler Isomet). The dimensions and wet weights of each cube specimen were measured and recorded. Wet weights were also recorded. Each specimen was labeled and marked to denote anatomic orientations, i.e. superior/inferior (S/I), medial/lateral (M/L), and anterior/posterior (A/P). The actual locations of each cube cut were documented and images distributed to define ROI locations for other analyses (to Raj Acharya for fractal analysis, to Jon Richardson at Baylor College of Medicine for DEXA, and to Chen Lin at Baylor College of Medicine for T2* MRI analysis). Quasi-static mechanical testing consisted of compressive loading in all three mutually perpendicular anatomic directions. Cyclic loading was applied for 10 cycles to pre-condition the specimen and results calculated for the eleventh. For one of three directions tested on each specimen, the 10 cycles were followed with loading to failure. Testing is currently proceeding and once completed the results will be correlated with data from the other analyses. One of the main points of interest is the relationship between fractal dimension and mechanical properties. Throughout preparation and testing all specimens were maintained hydrated with physiological saline and stored frozen when not being used.

INTRODUCTION

An important component in developing countermeasures for maintaining musculoskeletal integrity during long-term space flight is an effective and meaningful method of monitoring skeletal condition. Magnetic resonance imaging (MRI) is an attractive non-invasive approach because it avoids the exposure to radiation associated with X-ray based imaging and also provides measures related to bone microstructure rather than just density. Much of the initial work in this area deals primarily with the lower limb because of its prominence in overall skeletal function. Recent Summer Faculty Fellowship participants have devised methods for non-invasively determining the size and shape of the main load-bearing bones, such as the femur & tibia (Todd, 1994), and also estimating muscle forces and joint kinematics during exercise (Figueroa, 1995). The bone dimensions and geometry are derived from magnetic resonance images (MRI) since this avoids exposure to ionizing radiation as is customary with X-ray and similar methods. Finite element models of the femur can be constructed from the geometry data and the applied loads derived from physiological muscle force data. The goal is to use such models to predict the stresses and strains within the bone, and from them identify and assess regions of weakness and potential fracture risk. This detailed and quantitative insight will allow individualized evaluation of skeletal condition (pre-, post-, and in-flight) and prescription of exercise protocols for in-flight counter-measures as well as post-flight rehabilitation.

The next major step in developing this capability is to determine the material properties of the bone tissue within the bones. With methods available to generate the geometry and loads, a complete and more accurate model also requires information on the material properties of the bone or bones of interest. A major challenge at this point is to devise a way to estimate these properties from MRI data, which is a process essentially unexplored to date. Another recent Summer Faculty Fellowship participant has been studying methods for calculating fractal parameters from high-resolution MRI data in order to characterize the microarchitecture of trabecular bone tissue (Acharya *et al.*, 1995). The purpose of the research for the 1996 Summer Faculty Fellowship period has been to examine the potential usefulness of the MRI data to estimate the mechanical properties of trabecular bone. More specifically, correlations are being studied between the fractal parameters and elastic modulus, ultimate strength, apparent density, and bone mineral density. Considerable attention is being given to developing the detailed protocols and procedures needed and conducting preliminary tests to establish parameters and identify potential limitations

EXPERIMENTAL PROCEDURES

Overview

Much of the time and effort during the summer research period has been spent establishing and improving the detailed protocols and procedures required to execute and coordinate the research plan. The research involves collaboration between several different laboratories and personnel so extensive and effective coordination is essential. The main steps in the overall process can be summarized as follows:

1. Acquire whole bone specimens, cut to size, and embed for whole bone" MRI scanning.
(at University of Texas Medical School, Orthopaedic Biomechanics Laboratory)
2. MRI scan region 3-4 cm long using "high-resolution" coil.
(at Baylor College of Medicine/Methodist Hospital, Medical Physics)
3. Cut piece into slabs approximately 1.2 cm thick.
(at University of Texas Medical School, Orthopaedic Biomechanics Laboratory)
4. Scan slabs for bone mineral density using dual energy X-ray absorptiometry (DEXA).
(at Baylor College of Medicine /Methodist Hospital, Medical Physics)
5. Make high-detail contact X-rays to provide alternate images of trabecular architecture.
(at Texas A&M University, Veterinary Radiology)
6. Cut slabs into cubes for mechanical testing and define regions of interest (ROI).
(at University of Texas Medical School, Orthopaedic Biomechanics Laboratory)
7. Conduct mechanical tests and calculate mechanical properties of interest.
(at University of Texas Medical School, Orthopaedic Biomechanics Laboratory)
8. Determine wet and dry densities and ash weights.
(at University of Texas Medical School, Orthopaedic Biomechanics Laboratory)
9. Calculate fractal dimensions from MRI and X-ray images.
(at State University of New York at Buffalo, Biomedical Imaging Group)
10. Determine bone mineral densities and T2* effective relaxation times from DEXA and MRI data, respectively, for each ROI corresponding to test specimens.
(at Baylor College of Medicine /Methodist Hospital, Medical Physics)

Once the experimental tests are completed and the data analyzed, correlations will be examined between mechanical properties and other parameters. The mechanical properties of interest are the elastic moduli (in all 3 orthogonal directions) and the ultimate strength. The main microstructural parameter is the fractal dimension of the trabecular architecture. The fractal dimension is a novel quantity not commonly used for such purposes but recent studies have shown it to be a unique measure in distinguishing between normal and osteoporotic bone (Ruttimann *et al.*, 1992; Majumdar *et al.*, 1993; Weinstein and Majumdar, 1994). This suggests that the fractal dimension may likewise be a promising parameter for predicting mechanical properties. Addressing this question is therefore a major goal of the current research. For completeness and reference with other studies, additional microstructural measures to be included in correlation studies are the wet and dry densities and the ash weights.

Specimen Preparation and Imaging

Whole bones were acquired either through the University of Texas Medical School (human tibia) or the Texas A&M University College of Veterinary Medicine (equine radius). The bones were cut down to roughly one-third of the total length to isolate the metaphaseal regions containing significant trabecular bone. These pieces (proximal tibia for human bone and distal radius for equine bone) were then embedded using bone cement to mount them to plexiglass base plates. An embedded specimen is shown schematically in Figure 1.

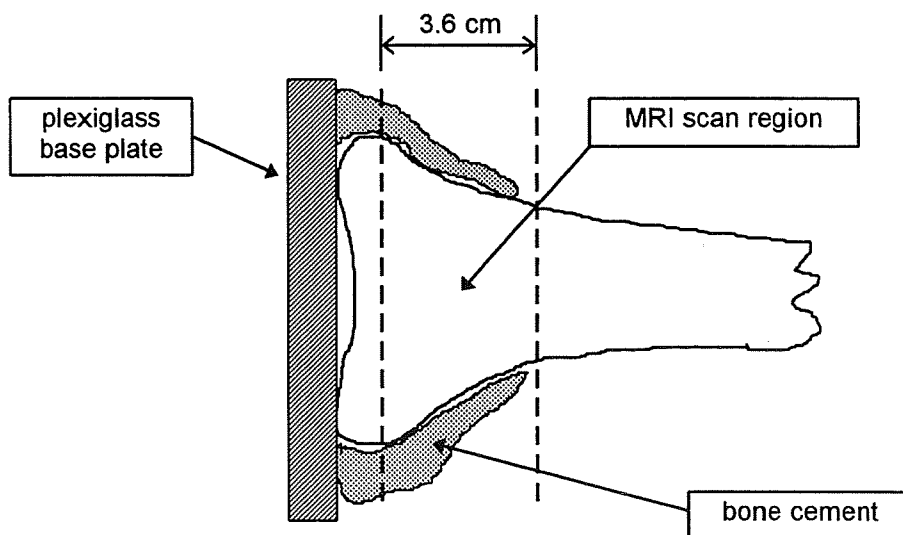


Figure 1. Embedded specimen for MRI scanning.

Each mounted specimen was transferred to the Baylor College of Medicine for MRI scanning by Dr. Chen Lin. In order to obtain images with high enough resolution to depict the microstructural architecture within trabecular bone tissue an orbit coil was used. The in-plane resolution of the orbit coil is 0.125 microns. Nine axial scans were made spanning a 3.6 cm long region on each specimen. Each scan was 2 mm thick with a 2 mm space between scans. Each 3.6 cm section was cut into 3 slabs approximately 1.2 cm thick on a band saw with custom fixtures for maintaining parallel, even cuts. The slabs and MRI scans are depicted in Figure 2. A coronal scan was also made for documenting the location of the axial scans. In order to maintain maximal clinical relevance, human proximal tibia bones were studied first. Upon reviewing the images from these bones, however, artifacts due to air pockets were observed, particularly in the central portions of the pieces where the porosity is high. Thus, an attempt was made to fully hydrate the specimens by storing in water overnight under a vacuum. The images from the re-hydrated specimens were still not as clear as *in vivo* or fresh bone, so further study was restricted to equine bone since these could be acquired fresh without being frozen before scanning. A total of 5 equine radius bones were prepared and scanned. The images were then sent to Dr. Raj Acharya for eventual fractal analysis.

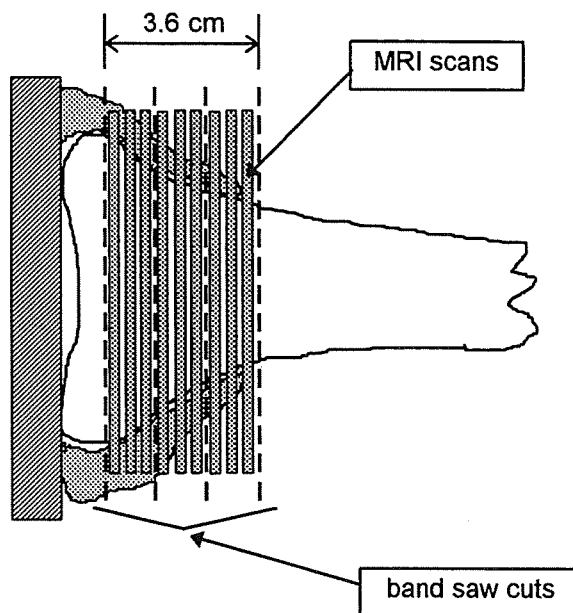


Figure 2. MRI scan and slab cutting details.

14-6

High-resolution contact radiographs were made of each slab to provide images for comparing fractal analysis with MR images. The X-ray images were also used to plan cutting cube specimens for mechanical testing. X-rays were made at 3 mA and 28 kV for two exposure times (45s and 60s) on a beryllium window GE model 2001437 unit in the Large Animal Radiology Lab of the College of Veterinary Medicine at Texas A&M University. In addition, each slab was radiographed in two orientations, with the superior surface "down" touching the film packet and with the inferior surface "down". The developed films were scanned into a PC to create TIF files (600dpi). A sample is shown in Figure 3. These images were also sent to Dr. Acharya for fractal analysis. Each of the slabs was also scanned by Mr. Jon Richardson of Baylor College of Medicine on a DEXA (dual energy X-ray absorptiometry) scanner for subsequent bone mineral density determination.

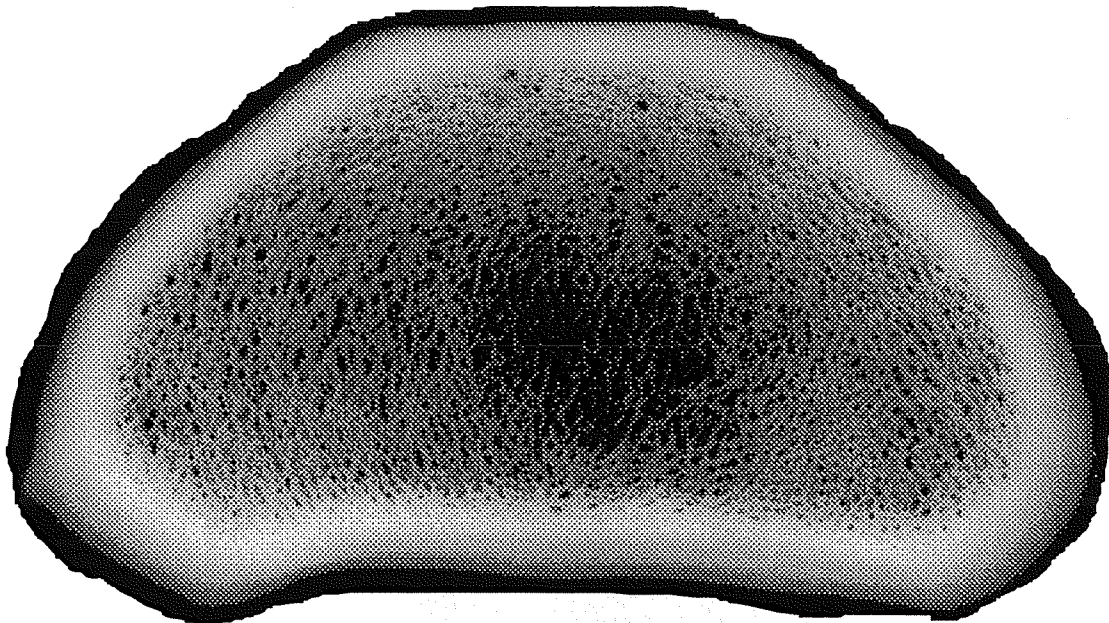


Figure 3. Sample X-ray image (scanned at 600dpi).

Mechanical Testing

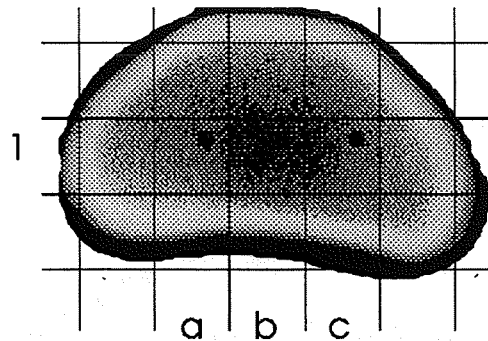
Before actually cutting the cube specimens, the number and location was planned graphically. A lower resolution (300dpi) scan was made of the X-ray encompassing all 3 slabs cut from each of the 5 bones. The TIF file was imported into CorelDraw and a 12 x 12 mm grid overlaid and positioned so as to maximize the number of cubes and allow adequate gripping in the saw. A sample image is shown in Figure 4 for bone "E3". Each of the bones was labeled E1 through E5, and the slabs from each were labeled A, B, and C from smallest to largest (i.e. superior to inferior, or proximal to distal), respectively.

E3

(cubes with 'dots' were cut)

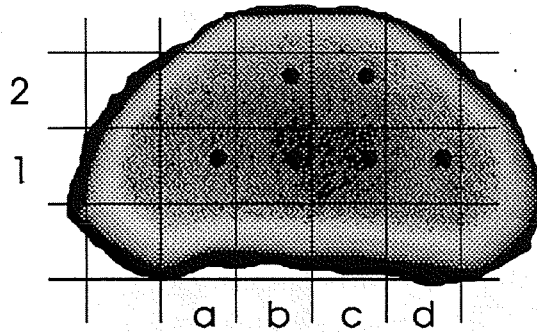
cube designations

Slab A



1a, 1b, 1c

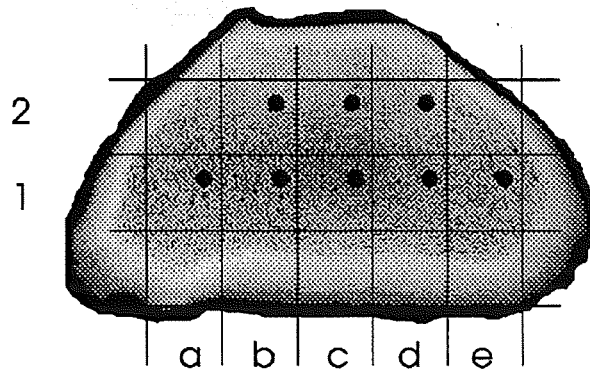
Slab B



2b, 2c

1a, 1b, 1c, 1d

Slab C



2b, 2c, 2d

1a, 1b, 1c, 1d, 1e

Figure 4. X-ray image with grids overlaid for planning cube specimen cuts.

The grid was transferred to each slab by making transparencies of the images, trimming around the edge of the bone, and then using this template to mark line positions. The lines were drawn with a fine point permanent marker pen. Cubes were cut in a slow-speed diamond blade wafering saw (Buehler Isomet) under continuous irrigation with distilled water. A dual blade tandem arrangement was employed to allow pairs of parallel cuts. Once the cubes were cut the confirmed positions were distributed as regions of interest (ROI) to the other investigators for fractal analysis (Raj Acharya), DEXA analysis (Jon Richardson), and MRI relaxation time determinations (Chen Lin). The ROI information included in Figure 4 is annotated to include a numbering system devised to uniquely identify each cube in the study. For example, the cube on the lower left of slab B shown would be designated E3B1a, where the first two digits identify the "parent" bone (E3), the next digit the slab (B), and the next two digits the "row/column" position within the slab (row 1, column a). After each cube was cut, the wet weight was measured on a microbalance and the dimensions determined using a digital caliper. The length for each of the 3 orthogonal anatomic directions was measured in six locations and averaged to give dimensions in the superior/inferior (S/I), anterior/posterior (A/P), and medial/lateral (M/L) directions. The cubes were wrapped in saline-soaked gauze in individually sealed plastic bags and stored frozen.

Mechanical testing was conducted in the Orthopaedic Biomechanics Laboratory at the University of Texas Medical School in Houston in collaboration with Drs. Timothy Harrigan and Catherine Ambrose. Procedures were developed similar to those of Goulet et al. (1994), Keller (1994), and Linde et al. (1992). A servo-hydraulic MTS 810 load frame was used to apply quasi-static compressive loading in each of the three anatomic directions. Polished aluminum platen fixtures were fabricated with the lower one articulated for self-aligning. The platens were lightly lubricated with glycerol just before mounting the specimens in place. Cyclic loading was applied at a rate of 1%/s to a level of 1% strain for 15 cycles. Force and displacement output were digitized at 50Hz and stored to disk. Data from the loading portion of the eleventh cycle was used for estimating the elastic modulus from the best-fit linear region. The first 10 cycles are for pre-conditioning the specimen to stabilize the response to consistent behavior. For the last of the three directions tested on each specimen, the 10 cycles were followed with loading to failure. A sample output plot for this case is shown in Figure 5. The ultimate strength is then calculated from the maximum load achieved. The direction for failure loading was randomized between S/I, M/L, and A/P. Thus, the mechanical testing of each specimen gives the elastic modulus in all three directions and the ultimate strength in one direction.

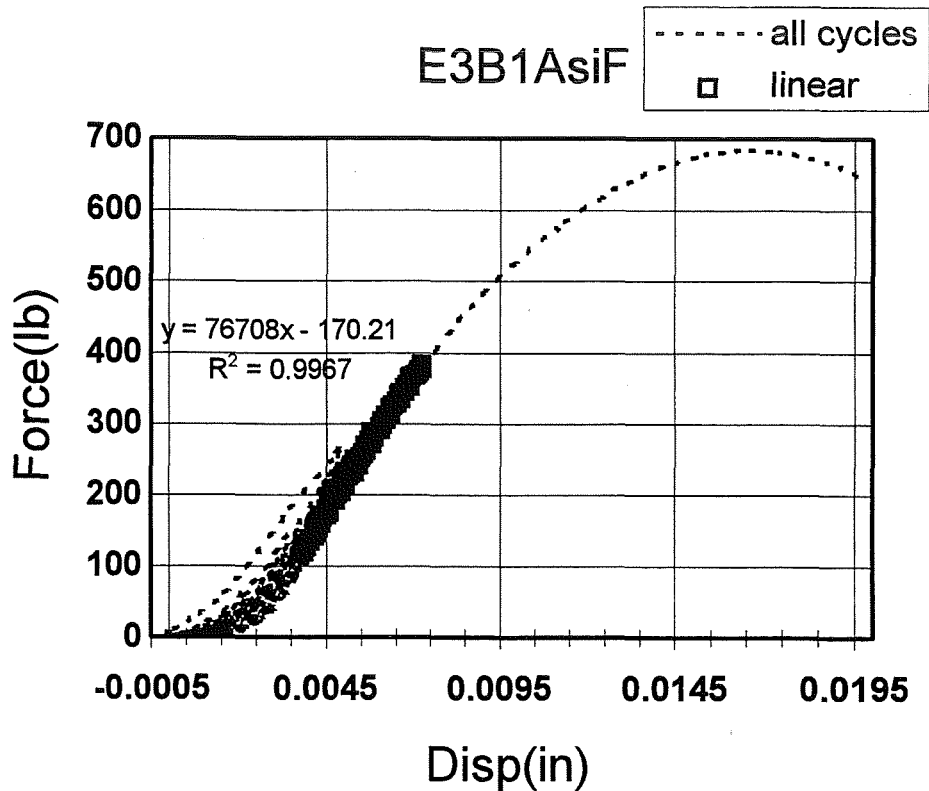


Figure 5. Force-displacement results for cyclic loading and failure overload.

Testing is currently proceeding and once completed each specimen will be defatted and dried in an oven at 100°C for 24 hours. The dry weight will be measured (in g) and dry density calculated by dividing by the volume (in cm³). The specimens will then be ashed in an oven at 500°C for 48 hours and weighed. The ratio of ash weight (in g) to dry weight (in g) is commonly expressed as a percentage and termed the "ash weight percent", or sometimes even just "ash weight". An ash density will also be calculated by dividing the ash weight (in g) by the volume (in cm³). The wet density will likewise be estimated by dividing the wet weight (in g) by the volume (in cm³). Once all testing and analysis is completed the following quantities will be determined directly from each cube specimen:

- wet density, fat-free dry density, and ash density
- ash weight percent
- elastic modulus in S/I, M/L, A/P directions
- ultimate strength in one direction

With proper identification of all ROI information between the various investigators, the following quantities will be calculated for the same specific tissue regions from which the cube specimens for mechanical testing were cut:

- fractal dimension
- MRI relaxation times (such as T2*)
- bone mineral density (BMD) and bone mineral content (BMC) from DEXA

Results will then be analyzed statistically to identify correlations between mechanical properties and fractal dimensions, T2*, BMD/BMC, and densities. The predictive ability of fractal dimension is of particular interest since this quantity reflects trabecular bone architecture and can be acquired non-invasively with X-ray exposure.

REFERENCES

- Acharya, R. S., LeBlanc, A., Shackelford, L. C., Swarnarkar, V., Krishnamurthy, R., Hausman, E., and Lin, C. (1995) Fractal analysis of bone structure with applications to osteoporosis and microgravity effects. (manuscript submitted).
- Ciarelli, M. J., Goldstein, S. A., Kuhn, J. L., Cody, D. D., and Brown, M. B. (1991) Evaluation of orthogonal mechanical properties and density of human trabecular bone from the major metaphyseal regions with materials testing and computed tomography. *J. Orthop. Res.* **9**, 674-682.
- Figuroa, F. (1995) Methodologies to determine forces on bones and muscles of body segments during exercise, employing compact sensors suitable for use in crowded space vehicles. *Final Report NASA/ASEE Summer Faculty Fellowship Program.*
- Goulet, R. W., Goldstein, S. A., Ciarelli, M. J., Kuhn, J. L., Brown, M. B., and Feldkamp, L. A. (1994) The relationship between the structural and orthogonal compressive properties of trabecular bone. *J. Biomechanics* **27**, 375-389.
- Keller, T. S. (1994) Predicting the compressive mechanical behavior of bone. *J. Biomechanics* **27**, 1159-1168.
- Linde, F., Hvid, I., and Madsen, F. (1992) The effect of specimen geometry on the mechanical behaviour of trabecular bone specimens. *J. Biomechanics* **25**, 359-368.
- Majumdar, S., Weinstein, R. S., and Prasad, R. R. (1993) Application of fractal geometry techniques to the study of trabecular bone. *Med. Phys.* **20**, 1611-1619.
- Ruttiman, U. E., Webber, R. L., and Hazelrig, J. B. (1992) Fractal dimension from radiographs of peridental alveolar bone. *Oral Surg.Oral Med.Oral Pathol.* **74**, 98-110.
- Todd, B. A. (1994) Finite element modeling of the lower extremities. *Final Report NASA/ASEE Summer Faculty Fellowship Program.*
- Weinstein, R. S. and Majumdar, S. (1994) Fractal geometry and vertebral compression fractures. *J. Bone Min. Res.* **9**, 1797-1802.

REPORT DOCUMENTATION PAGE

Form Approved
OMB No. 0704-0188

Public reporting burden for this collection of information is estimated to average 1 hour per response, including the time for reviewing instructions, searching existing data sources, gathering and maintaining the data needed, and completing and reviewing the collection of information. Send comments regarding this burden estimate or any other aspect of this collection of information, including suggestions for reducing this burden, to Washington Headquarters Services, Directorate for Information Operations and Reports, 1215 Jefferson Davis Highway, Suite 1204, Arlington, VA 22202-4302, and to the Office of Management and Budget, Paperwork Reduction Project (0704-0188), Washington, DC 20503.

1. AGENCY USE ONLY (Leave Blank)	2. REPORT DATE June 1997	3. REPORT TYPE AND DATES COVERED Contractor Report
----------------------------------	-----------------------------	---

4. TITLE AND SUBTITLE National Aeronautics and Space Administration (NASA)/American Society for Engineering Education (ASEE) Summer Faculty Program - 1996 Volume I	5. FUNDING NUMBERS
---	--------------------

6. AUTHOR(S) Richard B. Bannerot* and Donn G. Sickorez, Editors	
--	--

7. PERFORMING ORGANIZATION NAME(S) AND ADDRESS(ES) Lyndon B. Johnson Space Center Houston, Texas 77058	8. PERFORMING ORGANIZATION REPORT NUMBERS
--	---

9. SPONSORING/MONITORING AGENCY NAME(S) AND ADDRESS(ES) National Aeronautics and Space Administration Washington, D.C. 20546-0001	10. SPONSORING/MONITORING AGENCY REPORT NUMBER CR-202008
---	---

11. SUPPLEMENTARY NOTES * University of Houston; Houston, Texas
--

12a. DISTRIBUTION/AVAILABILITY STATEMENT Unclassified/Unlimited Available from the NASA Center for AeroSpace Information (CASI) 800 Elkridge Landing Road Linthicum Heights, MD 21090-2934 (301) 621-0390 Subject Category: 99	12b. DISTRIBUTION CODE
--	------------------------

13. ABSTRACT (Maximum 200 words) The 1996 JSC NASA/ASEE Summer Faculty Fellowship Program was conducted by the University of Houston and JSC. The objectives of the program, which began nationally in 1964 and at JSC in 1965 are to (1) further the professional knowledge of qualified engineering and science faculty members, (2) stimulate an exchange of ideas between participants and NASA, (3) enrich and refresh the research and teaching activities of participants' institutions, and (4) contribute to the research objectives of the NASA centers. Each faculty fellow spent at least 10 weeks at JSC engaged in a research project in collaboration with a NASA JSC colleague. This document is a compilation of the final reports on the research projects completed by the faculty fellows during the summer of 1996.

14. SUBJECT TERMS information transfer, research, research projects, urban research, engineering, science, universities, university program	15. NUMBER OF PAGES 167	16. PRICE CODE
--	----------------------------	----------------

17. SECURITY CLASSIFICATION OF REPORT Unclassified	18. SECURITY CLASSIFICATION OF THIS PAGE Unclassified	19. SECURITY CLASSIFICATION OF ABSTRACT Unclassified	20. LIMITATION OF ABSTRACT Unlimited
---	--	---	---